20 Years Annual Report

AG MAGNETISMUS

Annual Report 2016
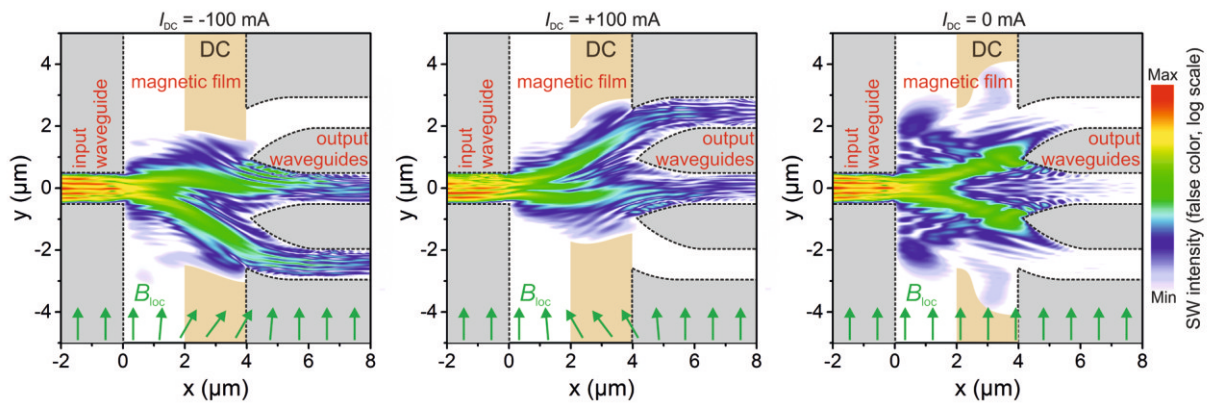

AG MAGNETISMUS
TU KAISERSLAUTERN

OPTIMAS

TECHNISCHE UNIVERSITÄT
KAISERSLAUTERN

Cover page: Shown is the micromagnetic simulation of a switchable spin wave (SW) signal splitter based on SW caustics. The SW caustics are created by opening the 1D input waveguide into the 2D magnetic film. Its curvilinear propagation arises due to the inhomogeneous magnetization of the film. For more details see Section 4.11. a) and b) Channeling of SW energy into different output waveguides depending on the direction of the applied DC-current. c) Suppression of the output signal, if no DC-current is applied.

Annual Report 2016

AG MAGNETISMUS
TU KAISERSLAUTERN
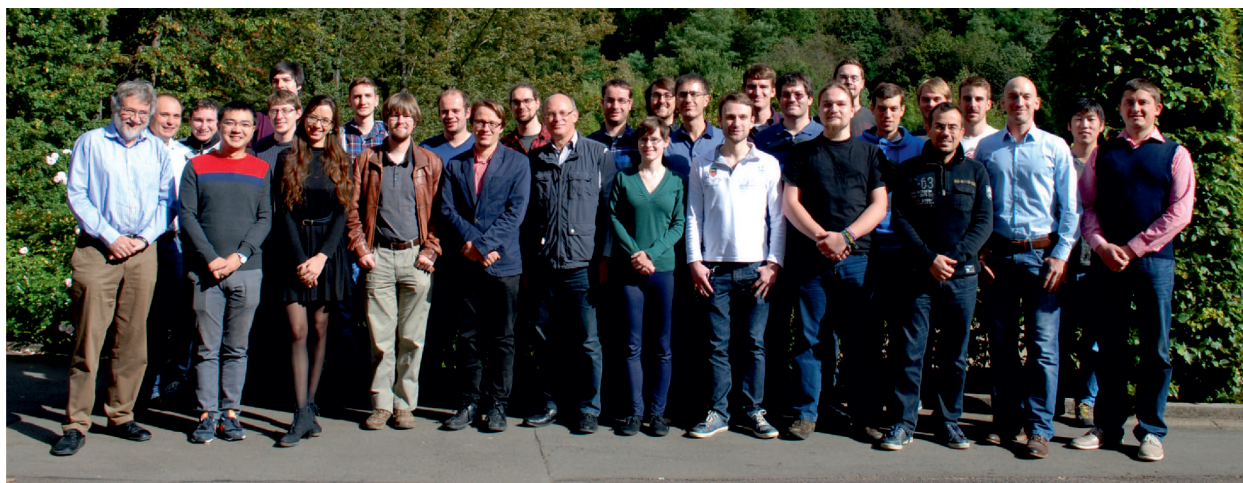
Address: Prof. Dr. Burkard Hillebrands
                Fachbereich Physik
                Landesforschungszentrum OPTIMAS
                Technische Universität Kaiserslautern
                Erwin-Schrödinger-Straße 56
                67663 Kaiserslautern, Germany
                Tel.: +49-(0)631-205-4228
                Fax.: +49-(0)631-205-4095

Postal address: Postfach 3049
                67653 Kaiserslautern, Germany

Internet: http://www.physik.uni-kl.de/hillebrands/
E-Mail: hilleb@physik.uni-kl.de

This Annual Report can be downloaded from:

http://www.physik.uni-kl.de/hillebrands/publications/annual-reports/

Our Group

From left to right:

Prof. Dr. Burkard Hillebrands, Dr. Andrii Chumak, Viktor Lauer, Qi Wang,
Pascal Frey, Björn Heinz, Laura Mihalceanu, Martin Kewenig, Dmytro Bozhko,
Michael Schneider, Dr. Philipp Pirro, Matthias Schweizer, Dr. Alexander Serga,
Thomas Langner, Ellen Wiedemann, Alexander Kreil, Dr. Andrés Conca Parra,
Steffen Steinert, Moritz Geilen, Sascha Keller, Hauke Georg Schäfer, Timo Noack,
Tobias Fischer, Jochen Greser, Thomas Meyer, Frank Heussner,
Jun. Prof. Dr. Evangelos Papaioannou, Kenji Fukuda (Guest),
Dr. Vitaliy Vasyuchka

(The picture was taken at our group retreat in Annweiler in October 2016.)

Not on the picture: Philipp Jaeger, Sibylle Müller, Dr. Isabel Sattler,
Halyna Musiienko-Shmarova, Dieter Weller This report contains unpublished results and
should
not be quoted without permission from the authors.

Contents

Chapter 1: Preface

Dear Colleagues and Friends,

we are happy to present our Annual Report 2016. This year, we celebrate an anniversary - this is the 20th edition of our Annual Report. If you are interested in our earlier Reports, they can be found on our home page. This Report is now covering the period November 2015 to October 2016.

Along this year we enjoyed several events important to us:

• Start of new Transregional Collaborative Research Center TR173 *Spin + X: Spin in its collective environment*: In January we had the official starting date. The initiative comprises 18 scientific projects distributed between researchers in Kaiserslautern and at the Johannes Gutenberg University in Mainz, plus a young researcher college. My group is engaged in three projects.

• Innovation Award Rhineland-Palatinate: In January we received the *Innovationspreis des Landes Rheinland-Pfalz* in the category "cooperation" jointly with the company Sensitec GmbH and the Johannes Gutenberg University Mainz for *Magnetoresistive Sensors for the Internet of Things and for Industry 4.0*.

• Funding from the European Research Council: In June Andrii Chumak started his ERC Starting Grant *Nanoscale magnonic circuits for novel computing systems* (*MagnonCircuits*). I received an ERC Advanced Grant on *Supercurrents of Magnon Condensates for Advanced Magnonics* (*SuperMagnonics*). Work started in October. To provide the needed measurement capacities two new Brillouin light scattering labs are currently installed. Both projects enable us to push forward fundamental and applied research in the field of magnonics and magnon spintronics, in particular by testing new ideas and concepts.

• IFW Dresden: I accepted an offer for the position of the Scientific Director and Board of the Leibniz Institute for Solid State and Materials Research in Dresden (IFW). I now share my time between Kaiserslautern and Dresden. Our research work in Kaiserslautern continues full steam. However, my teaching load and my involvement in committee work are reduced.

• Conferences and workshops: In January Andrii Chumak, jointly with our former group member Helmut Schultheiss (now at Helmholtz-Zentrum Dresden-Rossendorf), organized a Wilhelm and Else Heraeus-Seminar at the Physikzentrum Bad Honnef on Magnonics - *Spin waves connecting charges, spins and photons*. In June, in Kaiserslautern we organized the 3rd Workshop of the Core-to-Core Project Tohoku-York-Kaiserslautern *New concepts for future spintronic devices*. About 80 attendees mostly from Japan, the United Kingdom and Germany attended the event for three days. Apart from the excellent science the excursion with an original steam engine train into the valley of Elmstein including a wine tasting was a particular highlight.

New research highlights are:

• Magnon condensates and supercurrents: We have demonstrated for the first time the existence of a supercurrent at room temperature. Our system is a Bose-Einstein magnon condensate acting as a macroscopic quantum state carrying a magnonic supercurrent. We also investigated by experiment and accompanying theory a novel condensation phenomenon mediated by magneto-elastic interaction in a parametrically driven magnon gas - a spontaneous accumulation of hybrid
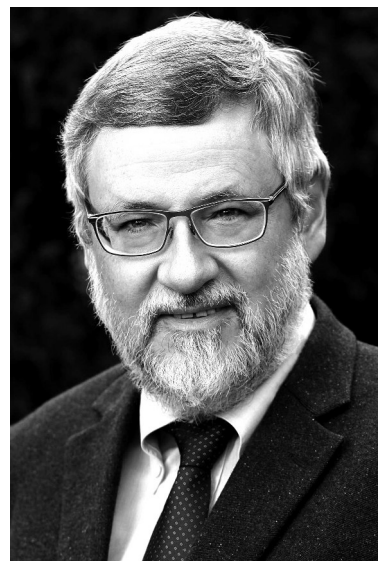
magneto-elastic bosons at the intersection of the lowest magnon mode and a transversal acoustic wave. We show that the population of these quasiparticles is determined by a bottleneck effect in the magnon transfer from high to low energy states through the magnon-phonon hybridization region.

• Auto-oscillations and spin Seebeck effect: We have studied the temporal evolution of the spin Hall effect - spin transfer torque (SHE-STT) driven auto-oscillations in a YIG/Pt microdisc using Brillouin light scattering (BLS) measurements. Furthermore, by time-resolved BLS we observed magnetization auto-oscillations in nanostructured YIG/Pt waveguides driven by the spin Seebeck effect due to a thermal gradient at the YIG/Pt interface. We also demonstrated the frequency dependence of the spin Seebeck effect in YIG/Pt bilayers. Moreover, we found that the characteristic response time is scaling approximately with the inverse thickness of the magnetic films.

• Magnon computing: We have experimentally realized a macroscopic spin-wave majority gate. And, using micromagnetic simulations, we have studied a nano-scaled spin-wave directional coupler in the form of two dipolar-coupled spin-wave waveguides separated by a gap. We also simulated a nano-scale reconfigurable magnonic crystal realized by using voltage-controlled perpendicular magnetic anisotropy in ferromagnetic-dielectric hetero-structures.

• Magneto-plasmonics: We achieved progress in understanding the behavior of magneto-plasmonic structures. By combining near and far-field measurements we were able to introduce the concept of a magneto-plasmonic meta-material.

Again, there have been several changes in our group. Britta Leven has left us for taking a position in our Department of Physics, now responsible for the student lab classes. We thank her for all her contributions, in particular to our applied research. Philipp Pirro returned to us after concluding a post-doc with Stéphane Mangin at the Institut Jean Lamour, Université de Lorraine, Nancy, France. He continues to act as a linking person for collaborations bringing together the material science competences of the Nancy group with our competences in magnon physics. Andrii Chumak received his habilitation on *Magnonic Crystals* and now has the status of Privatdozent. Donata Passarello finished her Ph.D. thesis in the framework of a collaboration with the IBM Almaden Research Center San José, U.S.A. in the group of Stuart Parkin. After completing his diploma thesis in our group, Timo Noack joined us as a new Ph.D. student. We also welcome Qi Wang, Pascal Frey and Halyna Musiienko-Shmarova as new Ph.D. students in our group, and Michael Schneider, Martin Kewenig, Moritz Geilen, Björn Heinz, Jochen Greser, Alexander Kreil and Ellen Wiedemann as new Diploma students.

Thomas Brächer was awarded the "Preis der Alumni-Vereinigung Physik" of the University of Kaiserslautern. He currently is a postdoc at SPINTEC, Grenoble.

Our work would not have been possible without valuable collaborations with people all over the world. They are too many to list them here all. In particular we would like to thank, in alphabetical order, Christoph Adelmann, Johan Åkerman, Yasuo Ando, Antonio Azevedo, Christian Back, Matthieu Bailleul, Gerrit Bauer, Arne Brataas, Yury Bunkov, Giovanni Carlotti, Florin Ciubotaru, Frederick Casper, Sergej Demokritov, Thibaut Devolder, Bernard Dieny, Marco Doms, Rembert Duine, Carsten Dubs, Ursula Ebels, Hajo Elmers, Jürgen Fassbender, Gerhard Fecher, Claudia Felser, Albert Fert, Mark Freeman, Sebastian Goennenwein, John Gregg, Hubert Grimm, Rudolf Gross, Dirk Grundler, Gianluca Gubbiotti, Konstantin Gusliyenko, Jaroslav Hamrle, Uwe Hartmann, Thomas Hauet, Michel Hehn, Jos Heremans, Atsufumi Hirohata, Axel Hoffmann, Hans Hübel, Gerhard Jakob, Xiaofeng Jin, Martin Jourdan, Gleb Kakazei, Boris Kalinikos, Alexy Karenowska, Sang-Koog Kim, Akihiro Kirihara, Olivier Klein, Mathias Kläui, Yuri Kobljanskyj, Peter Kopietz, Mikhail Kostylev, Volodymyr Kruglyak, Takahide Kubota, Ronald Lehn-

AG MAGNETISMUS
TU KAISERSLAUTERN

It is my special pleasure to greet all former group members. May this report help to stay in touch. If you are interested in our work I would be happy to hear from you.

With all my best wishes for Christmas, and a Happy New Year,

Kaiserslautern, November 2016

Vorwort

Liebe Kolleginnen und Kollegen, Freundinnen und Freunde unserer Arbeitsgruppe,

ich freue mich sehr, Ihnen wieder unseren Jahresbericht präsentieren zu dürfen. Diesmal feiern wir ein Jubiläum - dies ist die zwanzigste Auflage unseres Jahresberichts. Er deckt den Zeitraum von November 2015 bis Oktober 2016 ab.

Während dieses Jahres fanden viele für uns wichtige Ereignisse statt:

• Beginn des neuen Sonderforschungsbereichs/Transregio TR173 *Spin + X: Spin in its collective environment*: Im Januar war der offizielle Beginn. Die Zusammenarbeit umfasst 18 wissenschaftliche Projekte zwischen Wissenschaftlern in Kaiserslautern und an der Johannes Gutenberg-Universität in Mainz sowie eines Colleges für junge Wissenschaftler. Unsere Gruppe ist hierbei an drei Projekten beteiligt.

• Innovationspreis Rheinland-Pfalz: Im Januar erhielten wir den *Innovationspreis des Landes Rheinland-Pfalz* in der Kategorie "Kooperation" gemeinsam mit der Firma Sensitec GmbH und der Johannes Gutenberg-Universität Mainz für *Magnetoresistive Sensors for the Internet of Things and for Industry 4.0*.

• Finanzierung durch den Europäischen Forschungsrat: Im Juni begann Andrii Chumak seinen ERC Starting Grant zum Thema *Nanoscale magnonic circuits for novel computing systems (Magnon-Circuits)*. Ich erhielt einen ERC Advanced Grant für *Supercurrents of Magnon Condensates for Advanced Magnonics (SuperMagnonics)*. Die Arbeit diesbezüglich begann im Oktober. Um die nötigen Kapazitäten für die erforderten Messungen bereitzustellen, werden zwei neue Brillouin-Lichtstreu-Labore in Betrieb genommen. Beide Projekte ermöglichen uns, die Grundlagen- sowie die anwendungsorientierte Forschung im Bereich der Magnonik und Magnon-Spintronik voranzutreiben, insbesondere im Hinblick auf das Austesten neuer Ideen und Konzepte.

• IFW Dresden: Ich akzeptierte ein Angebot für die Stelle des wissenschaftlichen Direktors und Vorstands am Leibniz-Institut für Festkörperphysik und Materialwissenschaften (IFW) in Dresden. Nun teile ich meine Zeit auf zwischen Kaiserslautern und Dresden. Unsere Forschung in Kaiserslautern wird jedoch mit voller Kraft fortgesetzt. Jedoch wird meine Beteiligung an der Lehre und an Gremienarbeit reduziert.

• Konferenzen und Workshops: Im Januar organisierte Andrii Chumak gemeinsam mit unserem ehemaligen Gruppenmitglied Helmut Schultheiss (nun beschäftigt am Helmholtz-Zentrum in Dresden-Rossendorf) ein Wilhelm- und Else-Heraeus-Seminar am Physikzentrum Bad Honnef zum Thema *Magnonics - Spin waves connecting charges, spins and photons*. Im Juni organisierten wir in Kaiserslautern den dritten Workshop des Core-to-Core-Projektes Tohoku-York-Kaiserslautern mit dem Thema *New concepts for future spintronic devices*. Ungefähr 80 Teilnehmer, größtenteils aus Japan, Großbritannien und Deutschland, nahmen an der dreitägigen Veranstaltung teil. Abgesehen vom exzellenten wissenschaftlichen Austausch war auch die Exkursion mit einer originalen Dampfeisenbahn nach Elmstein mit einer anschließenden Weinprobe ein besonderes Highlight.

Unsere diesjährigen Forschungs-Highlights waren:

• Magnonenkondensate und -Supraströme: Wir konnten zum ersten Mal die Existenz eines Supra-

stroms bei Raumtemperatur nachweisen. Unser System ist ein Bose-Einstein-Magnonenkondensat, welches einen makroskopischer Quantenzustand darstellt und einen magnonischen Suprastrom trägt. Zusätzlich untersuchten wir durch Experimente und entsprechende Theorie ein neues Kondensationsphänomen vermittelt durch magnetoelastische Wechselwirkung in einem parametrisch angeregten Magnonengas - eine spontane Ansammlung hybridisierter magnetoelastischer Bosonen am Schnittpunkt der tiefsten Magnon-Mode mit einer transversalen Schallwelle. Wir konnten zeigen, dass die Besetzung dieser Quasiteilchen durch einen Engpass im Magnonentransfer von hohen hin zu niedrigen Energiezuständen, verursacht durch die Magnon-Phonon-Hybridisierung, bestimmt wird.

• Auto-Oszillationen und der Spin-Seebeck-Effekt: Wir untersuchten die zeitliche Entwicklung der durch Spin-Hall-Effekt - Spin-Transfer-Torque (SHE-STT) angeregten Auto-Oszillationen in einer YIG/Pt-Mikroscheibe mittels Brillouin-Lichtstreu- (BLS) Messungen. Wir beobachteten zudem in zeitaufgelösten BLS-Messungen Auto-Oszillationen der Magnetisierung von nanostrukturierten YIG/Pt-Wellenleitern, welche durch den Spin-Seebeck-Effekt bei einem Temperaturgradienten an der YIG/Pt-Oberfläche ausgelöst wurden. Ferner konnten wir die Frequenzabhängigkeit des Spin-Seebeck-Effekts in YIG/Pt-Doppellagen nachweisen. Wir fanden heraus, dass die charakteristische Reaktionszeit ungefähr mit der inversen Schichtdicke des magnetischen Films skaliert.

• Magnonen-Computing: Wir haben ein makroskopisches Spinwellen-Majoritätsgatter experimentell realisiert. Außerdem untersuchten wir mittels mikromagnetischer Simulationen einen räumlichen Spinwellen-Koppler auf der Nanometerskala, bestehend aus zwei dipolar gekoppelten Wellenleitern, welche durch eine Lücke getrennt sind. Zudem simulierten wir einen rekonfigurierbaren magnonischen Nanokristall durch spannungskontrollierte senkrechte magnetische Anisotropie in ferromagnetisch-dielektrischen Heterostrukturen.

• Magnetoplasmonik: Wir erreichten einen Fortschritt im Verständnis des Verhaltens magnetoplasmonischer Strukturen. Durch Kombination von Nahfeld- und Fernfeldmethoden war es uns möglich, das Konzept eines magneto-plasmonischen Metamaterials zu präsentieren.

Wieder einmal gab es einige Veränderungen in unserer Arbeitsgruppe. Britta Leven verließ uns für eine Anstellung im hiesigen Fachbereich für Physik, in der sie nun für die studentischen Laborpraktika verantwortlich ist. Wir möchten ihr an dieser Stelle für ihre vielen Beiträge danken, insbesondere bezüglich unserer angewandten Forschung. Philipp Pirro kehrte zu uns nach seinem Postdoc bei Stéphane Mangin am Institut Jean Lamour, Universität Lorraine in Nancy, Frankreich zurück. Er agiert auch weiterhin als eine Verbindungsperson für Zusammenarbeiten zwischen den materialwissenschaftlichen Kompetenzen der Gruppe aus Nancy und unseren Kompetenzen in Magnonenphysik. Andrii Chumak erhielt seine Habilitation zum Thema "Magnonic Crystals" und hält nun den Status eines Privatdozenten inne. Donata Passarello beendete ihre Doktorarbeit im Rahmen einer Kollaboration mit dem IBM Almaden Forschungszentrum in San José, USA, in der Gruppe von Stuart Parkin. Nach Fertigstellung seiner Diplomarbeit in unserer Gruppe begann Timo Noack bei uns eine Doktorarbeit. Wir begrüßen ebenfalls Qi Wang, Pascal Frey und Halyna Musiienko-Shmarova als neue Doktoranden sowie Michael Schneider, Martin Kewenig, Moritz Geilen, Björn Heinz, Jochen Greser, Alexander Kreil und Ellen Wiedemann als neue Diplomanden.

Thomas Brächer erhielt den Preis der Alumni-Vereinigung Physik der Universität Kaiserslautern. Er ist derzeit als Postdoc bei SPINTEC in Grenoble angestellt.

Unsere Arbeit wäre nicht ohne wertvolle Kooperationen mit Partnern aus der ganzen Welt möglich gewesen. Es sind zu viele um sie alle an dieser Stelle aufzulisten. Insbesondere möchten wir, in alphabetischer Reihenfolge, danken: Christoph Adelmann, Johan Åkerman, Yasuo Ando, Antonio

Azevedo, Christian Back, Matthieu Bailleul, Gerrit Bauer, Arne Brataas, Yury Bunkov, Giovanni Carlotti, Florin Ciubotaru, Frederick Casper, Sergej Demokritov, Thibaut Devolder, Bernard Dieny, Marco Doms, Rembert Duine, Carsten Dubs, Ursula Ebels, Hajo Elmers, Jürgen Fassbender, Gerhard Fecher, Claudia Felser, Albert Fert, Mark Freeman, Sebastian Goennenwein, John Gregg, Hubert Grimm, Rudolf Gross, Dirk Grundler, Gianluca Gubbiotti, Konstantin Gusliyenko, Jaroslav Hamrle, Uwe Hartmann, Thomas Hauet, Michel Hehn, Jos Heremans, Atsufumi Hirohata, Axel Hoffmann, Hans Hübel, Gerhard Jakob, Xiaofeng Jin, Martin Jourdan, Gleb Kakazei, Boris Kalinikos, Alexy Karenowska, Sang-Koog Kim, Akihiro Kirihara, Olivier Klein, Mathias Kläui, Yuri Kobljanskyj, Peter Kopietz, Mikhail Kostylev, Volodymyr Kruglyak, Takahide Kubota, Ronald Lehndorff, Joseph Losby, Jörg Lösch, Victor L'Vov, Sadamichi Maekawa, Stéphane Mangin, Gennadiy Melkov, Claudia and Tim Mewes, Shuichi Murakami, Hiroshi Naganuma, Sergei Nikitov, Jean-Pierre Nozières, Kevin O'Grady, Hideo Ohno, Tereo Ono, Mikihiko Oogane, Yoshichika Otani, Stuart Parkin, Johannes Paul, Anna Pomyalov, Günter Reiss, Sergio Rezende, Caroline Ross, Eiji Saitoh, John R. Sandercock, Rudi Schäfer, Gerd Schönhense, Helmut Schultheiss, Koji Sekiguchi, Jairo Sinova, Andrei Slavin, Rolf Slatter, Bob Stamps, Yoshishige Suzuki, Igor Syvorotka, Koki Takanashi, Vasyl Tiberkevich, Simon Trudel, Yaroslav Tserkovnyak, Kenichi Uchida, Alexey Ustinov, Bart van Wees, Martin Weides und Mingzhong Wu.

Es ist mir eine besondere Freude, hiermit auch allen ehemaligen Gruppenmitgliedern einen Gruß zu senden. Möge dieser Bericht uns helfen, im Kontakt zu bleiben. Wenn Sie an unserer Arbeit interessiert sind, würde ich mich freuen, von Ihnen zu hören.

Mit den besten Wünschen für ein frohes Weihnachtsfest und ein gutes Neues Jahr,

Kaiserslautern, im November 2016

Ihr Burkard Hillebrands

AG MAGNETISMUS
TU KAISERSLAUTERN

Chapter 2: Personnel

2.1   Members of the group

Group leader:

Prof. Dr. Burkard Hillebrands

Senior scientists:

Dr. habil. Andrii Chumak	
Dr. Andrés Conca Parra	
Dr. Britta Leven, Akad. Oberrätin	until 03/16
Jun. Prof. Dr. Evangelos Papaioannou	
Dr. Philipp Pirro	since 01/16
Dr. habil. Alexander Serga	
Dr. Vitaliy Vasyuchka	

Postdocs and long-term guest scientists:

Dr. Peter Clausen	until 06/16

Ph.D. students:

M.Sc.	Dmytro Bozhko	
Dipl.-Phys.	Tobias Fischer	
Dipl.-Phys.	Pascal Frey	since 07/16
Dipl.-Phys.	Frank Heussner	
Dipl.-Phys.	Sascha Keller	
Dipl.-Phys.	Thomas Langner	
Dipl.-Phys.	Viktor Lauer	
Dipl.-Phys.	Thomas Meyer	
Dipl.-Phys.	Timo Noack	since 09/16
Dipl.-Phys.	Laura Mihalceanu	since 12/15
M.Sc.	Halyna Musiienko-Shmarova	since 08/16
M.Sc.	Donata Passarello (IBM Research lab)	until 12/16
M.Sc.	Qi Wang	since 02/16

Diploma Students:

Moritz Geilen	since 12/15
Jochen Greser	since 02/16
Björn Heinz	since 11/15
Martin Kewenig	since 11/15
Alexander Kreil	since 06/16
Timo Noack	until 05/16

Michael Schneider	since 11/15
Ellen Wiedemann	since 10/16

Student Assistants:

Moritz Geilen	until 11/15
Björn Heinz	until 10/15
Philipp Jaeger	
Martin Kewenig	until 10/15
Dipl.-Phys. Laura Mihalceanu	until 11/15
Dipl.-Phys. Timo Noack	05/16 - 08/16
Hauke Georg Schäfer	
Michael Schneider	until 10/15
Matthias Schweizer	
Steffen Steinert	since 01/16

Engineers and Technicians

Dipl.-Ing. (FH) Dieter Weller

Administration:

Sibylle Müller
Dr. Isabel Sattler

AG MAGNETISMUS
TU KAISERSLAUTERN

2.2   Visiting scientists, postdoctoral fellows and exchange students

(sorted by date of first arrival in our group)

Prof. Dr. Victor S. L'vov, Weizmann Institute of Science, Rehovot   08.11. - 22.11.2015
Israel

During his visit we have established a strong scientific cooperation between our groups and initiated joint work on theoretical studies of the distribution of the magnon gas both in real and phase spaces and on investigations of phase induced magnon transport in thermal gradients, i.e. magnetic supercurrents.

Assoc. Prof. G. Vourlias, D. Karfaridis, Physics Department,   12.01. - 16.01.2015
Aristotle University of Thessaloniki, Thessaloniki
Greece

the visit took place in the framework of the DAAD exchange program Germany-Greece. During this visit the exchange of structural and magnetic measurements of magnetic multilayers was discussed.

Dr. Antonio Garcia-Martin, IMM-Instituto de Microelectronica de   21.01. - 22.01.2016
Madrid, Madrid
Spain

He gave an invited talk in the Optimas seminar with the title: "Resonant magnetoplasmonic structures: fundamentals and applications". During his visit intensive discussions took place with our group as well as with the group of Prof. M. Aeschlimann in relation to our SFB-TRR 173 SPIN+X-B07 project.

Dr. Christoph Adelmann, IMEC, Leuven   04.02. - 05.02.2016
Belgium

He is a principal investigator addressing thin films for BEOL & spintronics in IMEC. His primary interest is in the development of novel computing systems as an alternative to CMOS. Magnonics is of special interest in this view. During his visit we discussed the progress within our joint investigations towards spin-wave logic devices and magneto-acoustic cells required for the combination of these devices with CMOS technology.

Dr. Andrey Drozdovskiy, Saint Petersburg Electrotechnical   08.02. - 06.03.2016
University, Saint Petersburg
    Russia

    He is a member of the group of Prof. Boris Kalinikos with whom
    we collaborate in the frame of the German-Russian DFG project
    "Nonlinear spin wave dynamics in thin magnetic films and struc-
    tures". During his stay Andrey experimentally studied the prop-
    agation of coherent spin waves in ferromagnetic-ferrorelectric bi-
    layered structures based on YIG single-crystal films.

Prof. Dr. Yury M. Bunkov, Institut Neel, CNRS, Grenoble   04.04. - 07.04.2016
    France

    He visited our group in order to discuss our last findings in the field
    of Bose-Einstein magnon condensates and supercurrents. Yury pre-
    sented an invited talk "The spin superfluidity and magnon BEC",
    where he reviewed the field of magnon condensates in super-
    fluid ^{3}He and in the antiferromagnets with Suhl-Nakamura inter-
    action ($MnCO_3$, $CsMnF_3$, $RbMnF_3$).

Dongwook Go, Theoretical Nanoscale Transport Lab,   11.04. - 12.04.2016
Pohang University of Science and Technology, Pohang
    South Korea

    During a guest stay at the Forschungszentrum Jülich in the group
    of Stefan Blügel, Dongwook Go, a PhD student of the Theoretical
    Nanoscale Transport Lab of the Pohang University of Science and
    Technology (POSTECH) of the Republic of Korea visited our labs.
    During his stay he gave a talk on "Physics of Orbitronics: Orbital
    Rashba and orbital Hall effects".

Prof. Andrei Slavin, Oakland University, Rochester, Michigan   04.05. - 20.05.2016
    USA

    He visited our group as a Visiting MAINZ Professor in order to
    jointly work on parametric and kinetic instabilities of a parametri-
    cally driven dense magnon gas and on temporal dynamics of Bose-
    Einstein magnon and magnon-phonon condensates. In frame of our
    special group seminar Andrei gave two talks with titles "Mecha-
    nism of spin current transfer through antiferromagnetic dielectrics"
    and "Reconfigurable magnetic metamaterials for microwave signal
    processing".

Dr. Xavi Marti, Czech Academy of Sciences, Prague   02.06. - 03.06.2016
    Czech Repulic

    Dr. Xavi Marti visited our group to present his examples and vi-
    sions concerning the transfer of innovation from the field of spin-
    tronics into applications. In the framework of the laser and quan-
    tum optics seminar, he gave a talk entitled "Spintronics from nano
    to geo: antiferromagnetic memories, parkings and volcanoes".

Prof. Dr. Victor S. L'vov, Weizmann Institute of Science, Rehovot   25.07. - 21.08.2016
    Israel

    During his second visit Viktor was focused on the development of
    a theory of bottleneck accumulation of hybridized magneto-elastic
    bosons in parametrically pumped YIG films. As well, he consulted
    us concerning the theoretical studies of temporal properties of the
    magnon mediated longitudinal spin Seebeck effect in YIG-Pt struc-
    tures.

Dr. Anna Pomyalov, Weizmann Institute of Science, Rehovot   25.07. - 21.08.2016
    Israel

    She participated in the development of a theory of bottleneck accu-
    mulation of hybridized magneto-elastic bosons and performed the
    related numerical calculations. At our special group seminar she
    presented results of her numerical studies of vortex creation and
    development in the superfluid counterflow in a channel.

Prof. Andrei Slavin, Oakland University, Rochester, Michigan   25.07. - 09.08.2016
    USA

    During his second visit Andrei focused on the theoretical studies
    of thermal magnon-phonon dipolar-exchange spectra measured in
    arbitrarily magnetized YIG films by our new wavevector-resolved
    BLS setup.

Tomosato Hioki, Institute for Materials Research, Tohoku University,   15.08. - 23.09.2016
Sendai
    Japan

    He is a graduate student from the group of Prof. E. Saitoh at
    the Tohoku University in Sendai with whom we have a long and
    productive cooperation. During his stay, Hioki performed BLS
    wavevector-resolved measurements of the lutetium bismuth iron
    garnet ($(Lu,Bi)_3(Fe,Ga)_5O_{12}$) and iron borate ($FeBO_3$) samples
    which complement the results obtained in Sendai.

Prof. Dr. Yury M. Bunkov, Institut Neel, CNRS, Grenoble   17.08. - 31.08.2016
France

He has visited us a second time during the year in order to deeply discuss the physics of magnon supercurrents in ferrite films of yttrium-iron-garnet (YIG) and to plan joint experimental studies of Bose-Einstein condensation of magnons in arbitrary magnetized YIG films. Yury gave an invited talk in the OPTIMAS seminar with the title: "Cosmology in superfluid 3He", where he showed many analogies between the superfluid ^{3}He and the Universe, which can be understood as quantum superfluid liquids with complex broken symmetries and with a number of excitations, particles and defects.

Dr. Max Lein, Dr. Koji Sato, Advanced Institute of Materials Research,   17.08. - 18.08.2016
Tohoku University, Sendai
Japan

They are theoretical physicists who discussed in Kaiserslautern together with Kei Yamamoto from the University of Mainz the possibility to use magnons as a model systems for topological bosons and topology induced properties of classical wave systems.

Dr. Kei Yamamoto, Institut für Physik, Universität Mainz, Mainz   17.08. - 18.08.2016
Germany

Kei Yamamoto is a theoretical physicists who discussed in Kaiserslautern together with Max Lein and Koji Sato from the Tohoku University in Sendai the possibility to use magnons as a model systems for topological bosons and topology induced properties of classical wave systems.

Monika Mycroft, Oxford University, Oxford   29.08. - 05.10.2016
United Kingdom

She has visited our group in the framework of our collaboration with the group of Prof. John Gregg on studies of spin dynamics in magnetic bilayers.

Kenji Fukuda, Tohoku University, Sendai   14.09. - 26.10.2016
Japan

He visited our group in the context of the Core-to-Core collaboration. During his stay, he presented his work on the fabrication and characterization of ferrimagnetic Mn-based Heusler epitaxial thin films and performed BLS measurements to further investigate the properties of these films.

*AG MAGNETISMUS
TU KAISERSLAUTERN*

Dr. Florin Ciubotaru, IMEC, Leuven   21.09. - 30.09.2016
   Belgium

   Focusing on the realization of spin-wave logic elements, Florin visited our group to perform BLS measurements in order to investigate the properties of confined spin-wave modes in scaled sub-micron CoFeB waveguides.

Assoc. Prof. Georgios Vourlias and group members, Physics   09.10. - 21.10.2016
Department, Aristotle University of Thessaloniki, Thessaloniki
   Greece

   He and Dimitris Karfaridis, Kostantinos Symeonidis, Nikolaos Pliatsikas, Dimitris Chaliambalias and Evangelia Tarani visited our group in the framework of the DAAD exchange program Germany-Greece. Kostantinos presented his data on magnetometry for the magnetic bilayers as well as for magnetic nanoparticles. Dimitris Karfaridis together with Nikolaos presented in the group their results on x-rays diffraction, transmission electron microscopy and x-rays photoelectron spectroscopy on Fe/MgO/Pt trilayers. Dimitris Chaliambalias together with Evangelia discussed their structural data with respect to our magnetic measurements.

2.3   Guest seminars

Victor S. L'vov
16.11.2015

Weizmann Institute of Science, Rehovot, Israel
Freak Waves in the Ocean
Group seminar

Tilmann Beck
14.12.2015

Technische Universität Kaiserslautern, Kaiserslautern, Germany
Fatigue of metals under cyclic loading and its identification by innovative measurement methods
Group seminar

Antonio Garcia-Martin
21.01.2016

IMM-Instituto de Microelectronica de Madrid, Madrid, Spain
Resonant magnetoplasmonic structures:fundamentals and applications
OPTIMAS Laser- and quantum-optics seminar

Dominik Marcó
26.01.2016

Department of Magnetic Microstructures, IFW Dresden, Dresden, Germany
Strayfield-induced Faraday contributions in wide-field Kerr microscopy and -magnetometry
Special group seminar

Christoph Adelmann
04.02.2016

IMEC, Leuven, Belgium
Computing with spin waves
OPTIMAS Laser- and quantum-optics seminar

Manisha Kumari
10.02.2016

Indian Institute of Technology, Delhi, India
Spin pumping in NiFe/Ta sputtered bilayers
Special group seminar

Andrey Drozdovskii
15.02.2016

Saint Petersburg Electrotechnical University, Saint Petersburg, Russia
Spin waves in ferromagnetic-ferrorelectric structures based on YIG single-crystal films.
Special group seminar

Yury M. Bunkov
05.04.2016

Institut Néel, CNRS, Grenoble, France
The spin superfluidity and magnon BEC
Special group seminar

Dongwook Go
11.04.2016

Theoretical Nanoscale Transport Lab, Pohang University of Science and Technology, Pohang, South Korea
Physics of orbitronics: orbital Rashba and orbital Hall effects
Special group seminar

AG MAGNETISMUS
TU KAISERSLAUTERN

Olena Gomonai
18.04.2016	Johannes Gutenberg Universität Mainz, Germany
Spintronics with antiferromagnets: what's new compared to ferromagnets
Group seminar
Andrei Slavin
12.05.2016	Oakland University, Rochester, Michigan, USA
Mechanism of spin current transfer through antiferromagnetic dielectrics
Special group seminar
Andrei Slavin
17.05.2016	Oakland University, Rochester, Michigan, USA
Reconfigurable magnetic metamaterials for microwave signal processing
Special group seminar
Xavi Marti
03.06.2016	Czech Academy of Sciences, Prague, Czech Republic
From nano to geo: Spin-orbit coupling applied to antiferromagnetic memories, cars and volcanoes
OPTIMAS Laser- and quantum-optics seminar
Olivier Rousseau
18.07.2016	Université Paris 13 Nord, Villetaneuse, France
Spin-wave interferometer for magnon logic
Group seminar
Anna Pomyalov
18.08.2016	Weizmann Institute of Science, Rehovot, Israel
Spatiotemporal development of mesoscopic quantum vortex tangles in counterflowing ^4He
Special group seminar
Richard Schlitz
29.08.2016	Walther-Meißner-Institut, München, Germany
Spin Transport Experiments in Hybrid Nanostructures
Special group seminar
Yury M. Bunkov
30.08.2016	Institut Néel, CNRS, Grenoble, France
Superfluid ^3He and Cosmology
Special OPTIMAS seminar
Tomosato Hioki
19.09.2016	Institute for Materials Research, Tohoku University, Sendai, Japan
Time-resolved spin Seebeck effect in high magnetic fields
Special group seminar
Monika Mycroft
26.09.2016	Oxford University, Oxford, United Kingdom
Model of metallic bi-layer spin battery
Special group seminar
Teruo Ono
26.09.2016	Institute for Chemical Research, Kyoto University, Japan
Spin dynamics in inhomogeneously magnetized systems
IEEE Magnetics Society distinguished Lecture, Special OPTIMAS seminar

2.4 Visits of group members at other laboratories

Sascha Keller	Group of Assoc. Prof. Georgios Vourlias, Aristotle University, Thessaloniki, Greece 09.12.2015 - 16.12.2015 Host: Assoc. Prof. Georgios Vourlias
Laura Mihalceanu	Group of Assoc. Prof. Georgios Vourlias, Aristotle University, Thessaloniki, Greece 09.12.2015 - 12.12.2015 Host: Assoc. Prof. Georgios Vourlias
Matthias Schweizer	Group of Assoc. Prof. Georgios Vourlias, Aristotle University, Thessaloniki, Greece 10.12.2015 - 16.12.2015 Host: Assoc. Prof. Georgios Vourlias
Tobias Fischer	Group of Prof. Yasuo Ando, Tohoku University, Sendai, Japan 04.04.2016 - 30.05.2016 Host: Prof. Yasuo Ando and Mikihiko Oogane
Evangelos Papaioannou	Group of Assoc. Prof. Georgios Vourlias, Aristotle University, Thessaloniki, Greece 04.04.2016 - 07.04.2016 Host: Assoc. Prof. Georgios Vourlias
Evangelos Papaioannou	Group of Prof. Björgiv Hjörvarsson, Uppsala University, Uppsala, Sweden 27.05.2016 - 30.05.2016 Host: Prof. Björgiv Hjörvarsson
Timo Noack	Center for Materials for Information Technology (MINT), Alabama, USA 01.06.2016 - 29.07.2016 Host: Prof. Dr. Takao Suzuki
Dmytro Bozhko	Group of Prof. G.A. Melkov, Faculty of Radiophysics, Electronics and computer systems, National Taras Shevchenko University of Kyiv, Kyiv, Ukraine 17.08.2016 - 31.08.2016 Host: Prof. G.A. Melkov

AG MAGNETISMUS
TU KAISERSLAUTERN

2.5   Group member photo gallery

Dmytro Bozhko
Ph.D. student

Dr. Andrii Chumak
Senior scientist

Dr. Peter Clausen
Postdoc

Dr. Andrés Conca Parra
Senior scientist

Tobias Fischer
Ph.D. student

Pascal Frey
Ph.D. student

Moritz Geilen
Diploma student

Jochen Greser
Diploma student

Björn Heinz
Student assistant

Frank Heussner
Ph.D. student
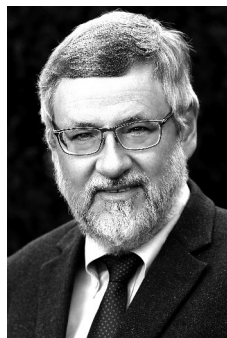
Prof. Dr. Burkard Hillebrands
Group leader

Philipp Jaeger
Student assistant

Sascha Keller
Ph.D. student

Martin Kewenig
Diploma student

Alexander Kreil
Diploma student

Thomas Langner
Ph.D. student

Viktor Lauer
Ph.D. student

Dr. Britta Leven
Senior scientist
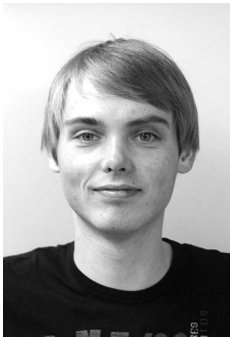
Thomas Meyer
Ph.D. student

Laura Mihalceanu
Ph.D. student

Halyna Musiienko-Shmarova
Ph.D. student

Sibylle Müller
Secretary

Timo Noack
Ph.D. student

JProf. Dr. Evangelos Papaioannou
Senior scientist

AG MAGNETISMUS
TU KAISERSLAUTERN

Donata Passarello
Ph.D. student

Dr. Philipp Pirro
Postdoc

Dr. Isabel Sattler
Administration

Hauke Georg Schäfer
Student assistant

Michael Schneider
Diploma student

Matthias Schweizer
Student assistant

Qi Wang
Ph.D. student

Dieter Weller
Mechanical engineer

Dr. Alexander Serga
Senior scientist

Steffen Steinert
Student assistant

Dr. Vitaliy Vasyuchka
Senior scientist

Chapter 3: Methods

3.1   Brillouin light scattering spectroscopy (BLS)

Brillouin light scattering spectroscopy (BLS) is the primary key technique in our laboratory to investigate the dynamic properties of magnetic materials and devices. It is based on the interaction of photons with the fundamental excitations of a solid such as magnons, the quanta of magnetic excitations. The interaction can be understood as an inelastic scattering process of the incident photons with magnons, taking into account energy and momentum conservation as indicated in Fig. 1. This technique is sensitive for incoherent, thermal magnons as well as for externally excited, coherent excitations.
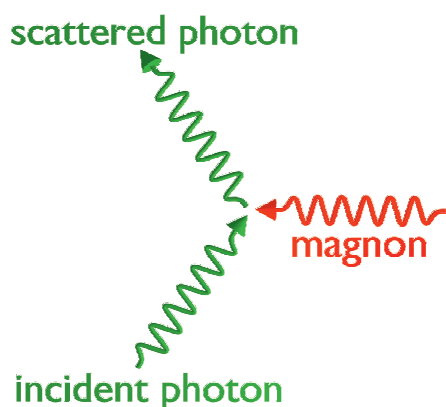
Fig. 1: Scheme of inelastic scattering of an incident photon by a magnon. Here, the annihilation process where the frequency of the scattered photon is increased by the frequency of the annihilated magnon is shown.

The detection of the inelastically scattered photons, i.e. the separation from the elastically scattered photons and the determination of the transferred energy, requires an interferometric technique with extremely high contrast and sensitivity. In our laboratory we implemented the (3+3) Tandem-Fabry-Pérot-Interferometer, designed by John R. Sandercock and schematically shown in Fig. 2. It consists of two Fabry-Pérot interferometers (FPI), each one passed three times by the inelasti-
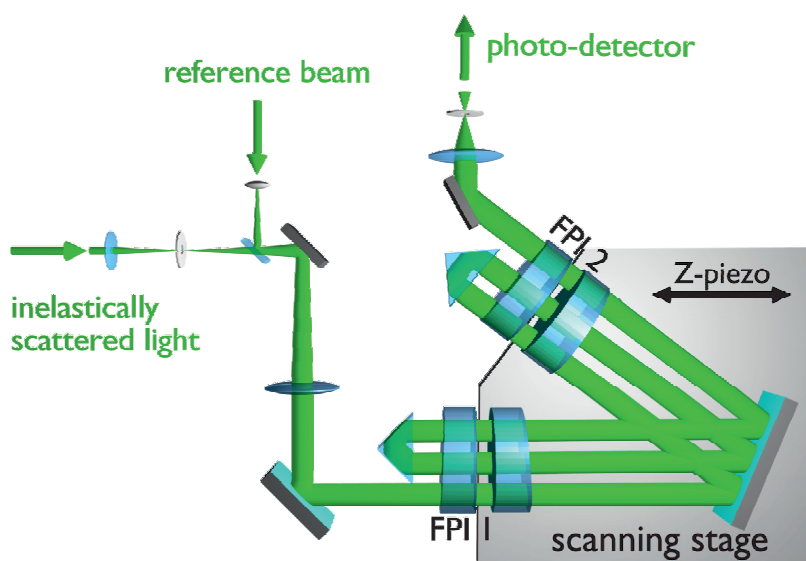
Fig. 2: Scheme of a (3+3) tandem Fabry-Pérot interferometer, designed and build by John R. Sandercock (JRS Scientific Instruments, Mettmenstetten, Switzerland)
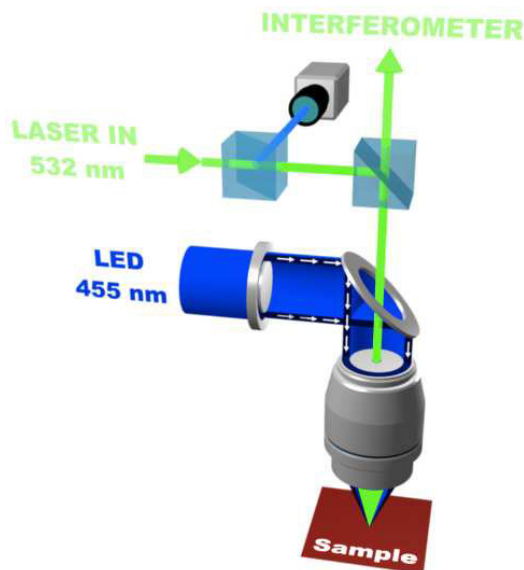
Fig. 3: Schematic setup of a BLS-microscope. The laser light is focused on the sample using a high resolution objective which is also collecting the scattered photons. The LED light is used to monitor the position of the laser focus on the sample by a CCD camera and to apply active position control to the sample stage.

cally scattered light. This approach results in a contrast better than 10^{10} for the separation of the elastically and inelastically scattered photons in a frequency range from 500 MHz up to 1 THz.

In the last decade we made significant progress in the improvement of BLS spectroscopy. The spatial resolution was pushed to the fundamental limit of classical optics by constructing a BLS microscope (Fig. 3) with sophisticated active stabilization methods. In this way, spin-wave transport phenomena can be investigated in micro-structures including time- and phase resolved measurements. However, in the BLS microscope, the wave vector resolution is lost since the angle of light incidence is not well defined anymore. Thus, wave vector resolved measurements like the direct determination of the dispersion relation are conducted with conventional BLS which has a typical spatial resolution of about 50 μm.

In a further development during the past two years, our BLS equipment has been upgraded towards the investigation of new material systems. Integrating a blue laser with a wavelength of 491 nm into one of our micro-focus BLS setups opened up an access to the dynamics of thin YIG films (with thicknesses of 100 nm and below) by largely increasing the sensitivity since the effective scattering cross section is much higher at this wavelength.

A further advancement regarding our standard BLS techniques is the pulsed probe laser beam technique allowing for the detection of various evolution processes such as, e.g., the temperature evolution inside a sample. The special feature of this technique is that the focused laser beam combines the role of the magnon probe with the role of a local sample heater. The heating time is adjusted using amplitude modulation of the probing laser beam by an acousto-optic modulator (AOM). The scheme of the corresponding experimental setup, which consists of a YIG film sample, a microwave circuit, and a BLS laser system, is shown in Fig. 4.

The following list gives an overview of the different BLS setups available in our group. In addition to the optical elements, all setups are equipped with various microwave components to excite and amplify spin waves.

BLS1: High-field electromagnet (1.2 T), conventional BLS spectroscopy (spacial resolution 50 μm, wave-vector resolution $\delta k \approx 0.2\,\text{rad}/\mu\text{m}$ with maximal wave vector $k_{\max} \approx 23\,\text{rad}/\mu\text{m}$). Time- and phase resolution.
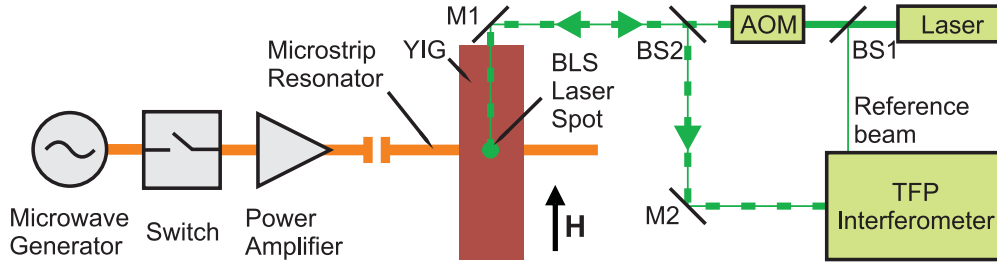
Fig. 4: Schematic illustration of the BLS setup with pulsed probe laser beam technique. On the left hand side, the microwave circuit consisting of a microwave source, switch and amplifier is shown. This circuit drives a microstrip resonator, which is placed below a YIG film. The green dot illustrates the focus position of the BLS laser. On the right hand side, the BLS laser beam path is indicated. The light of the laser is split by a beam splitter (BS1). The sample beam is sent to an acousto-optic modulator and the reference beam to the interferometer. The modulated sample beam is guided through the second beam splitter (BS2) and the mirror (M1) to the YIG film where it scatters. The scattered light is reflected again at M1 and deflect by BS2 to the Tandem Fabry-Pérot interferometer.

BLS2: BLS spectroscopy with microscope (250 nm spatial resolution, $k_{max} \approx 17$ rad/µm) and positioning stage. Option for time- and phase resolution.

BLS3: High-field electromagnet (1.2 T) and conventional BLS spectroscopy (wave-vector resolution $\delta k \approx 0.2$ rad/µm with maximal wave vector $k_{max} \approx 23$ rad/µm). Microscope stage with 250 nm spatial resolution ($k_{max} \approx 17$ rad/µm) and electromagnet (0.1 T) for in-plane fields. Option for time- and phase resolution as well as for an out-of-plane electromagnet.

BLS4: Electromagnet (0.1 T), BLS spectroscopy with microscope (250 nm spatial resolution) with green ($\lambda = 532$ nm) and blue laser ($\lambda = 491$ nm). Option for time and phase resolution.

3.2   Microwave techniques

Brillouin light scattering (BLS) spectroscopy, as described in the previous section, is a powerful tool for the detection of spin waves and measurement of their characteristics. Nevertheless, it does not allow for spin-wave excitation. Thus, in many of our experiments BLS spectroscopy is combined with microwave techniques which ensure high-efficient generation of spin waves in magnetic structures. Spin waves are emitted by nano- and micro-sized microstrip antennas placed on the surfaces of magnetic thin films and is driven by a microwave signal in the GHz frequency range [1, 2]. Microwave sources in our laboratories generate signals of up to 70 GHz providing access to spin-waves in a very wide range of frequencies and wavenumbers. Furthermore, large powers (up to 200 W) provided by microwave amplifiers allow for the study of strongly nonlinear spin-wave dynamics as well as for quantum effects in parametrically-driven magnon gases. The microwave technique allows for the excitation of both, continuous spin waves as well as short spin-wave packets. Among other advantages, the pulsed technique enables the realization of time resolved (resolution down to 250 ps) BLS spectroscopy [3] shown in Fig. 1. The continuous microwave excitation, by-turn, allows realization of phase-resolved BLS spectroscopy [4, 5].

Besides the excitation of spin waves, the microwave technique is intensively used for high-sensitive (10^{-13} W) detection. Using the same antennas the magnetization precession is converted into microwave currents. These currents are amplified by low-noise amplifiers and analyzed using
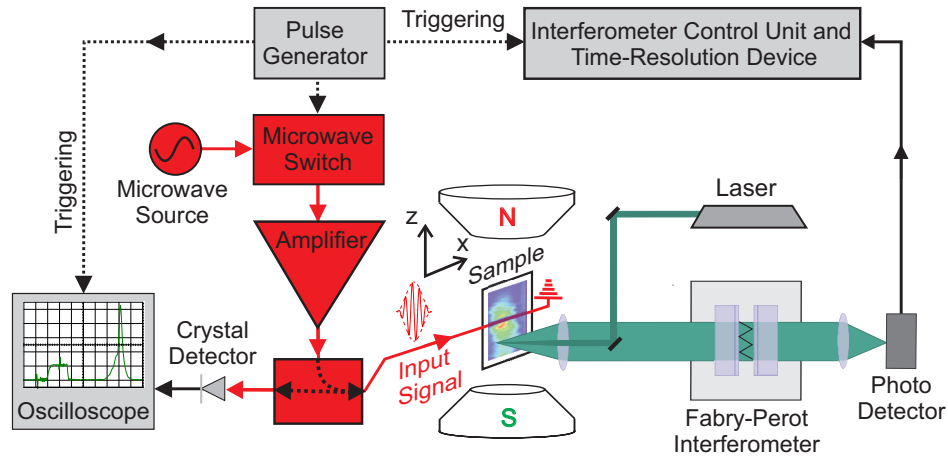
Fig. 1: Scheme of the microwave-assisted time- and space-resolved BLS setup

wide-band oscilloscopes, vector network analyzers or a spectrum analyzer. A vector network analyzer is also used for the ferromagnetic resonance (FMR) measurements allowing determination of such characteristics of the magnetic thin films as magnetization saturation, exchange constant, and damping.

We gain from the modern microwave setup for broadband microwave analysis installed in our lab. This setup, schematically shown in Fig. 2, consists of the following complementary devices: vector network analyzer, spectrum analyzer, microwave signal generator, two high-power microwave amplifiers, and a magnet. It has a wide frequency bandwidth of up to 70 GHz which allows for the microwave excitation of spin waves with wavelengths down to 30 nm. This helps us to perform measurements in the frame of modern nanometer-scale magnonics. The broadband microwave analysis can be conducted in both the CW and pulsed regime. The possibility to switch between CW and time-resolved measurements of the vector network analyzer gives us a unique opportunity to separate spin-wave signals from much larger electromagnetic leakages.
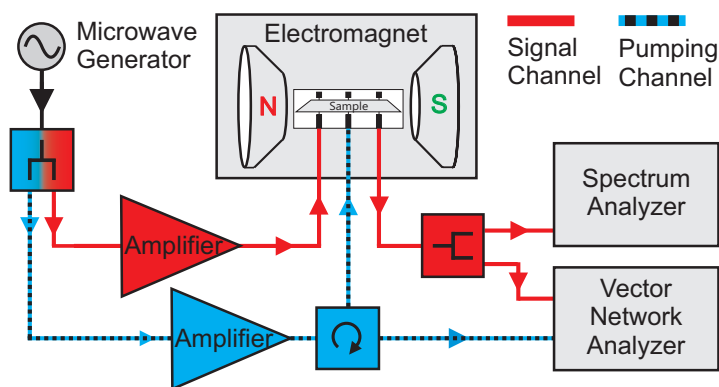
Fig. 2: Diagram of the experimental setup for microwave analysis with a wide frequency bandwidth up to 70 GHz

Our microwave techniques have been recently amended by detection of spin waves and spin currents using the inverse spin Hall effect. During the last year a new microwave spin pumping setup has been installed in our lab. It allows us to detect spin current-induced electric signals in a ferromagnet|normal-metal bilayers as dependence of the direction of the in-plane magnetic field.

AG MAGNET|SMUS
TU KA|SERSLAUTERN

References

[1] A.V. Chumak, V.I. Vasyuchka, A.A. Serga, B. Hillebrands, *Magnon spintronics*, Nat. Phys. **11**, 453 (2015).

[2] A.A. Serga, A.V. Chumak, B. Hillebrands, *YIG magnonics*, J. Phys. D **43**, 264002 (2010).

[3] O. Büttner, M. Bauer, S.O. Demokritov, B. Hillebrands, Yu.S. Kivshar, V. Grimalsky, Yu. Rapoport, A.N. Slavin, *Linear and nonlinear diffraction of dipolar spin waves in yttrium iron garnet films observed by space- and time-resolved Brillouin light scattering*, Phys. Rev. B **61**, 11576 (2000).

[4] A.A. Serga, T. Schneider, B. Hillebrands, S.O. Demokritov, M.P. Kostylev, *Phase-sensitive Brillouin light scattering spectroscopy from spin-wave packets*, Appl. Phys. Lett. **89**, 063506 (2006).

[5] K. Vogt, H. Schultheiss, S.J. Hermsdoerfer, P. Pirro, A.A. Serga, B. Hillebrands, *All-optical detection of phase fronts of propagating spin waves in a $Ni_{81}Fe_{19}$ microstripe*, Appl. Phys. Lett. **95**, 182508 (2009).

3.3   Magneto-optic Kerr effect magnetometry and microscopy (MOKE)

The magneto-optical Kerr effect (MOKE) is a well established technique to study magnetization properties. The effect is based on the fact, that the plane of polarization of light is rotated when the light is reflected from a magnetic material [1]. The physical origin of MOKE is the magnetic circular dichroism effect: exchange and spin-orbit coupling in a magnetic material lead to different absorption spectra for left- and right-circularly polarized light. Measuring the change of the polarization of the reflected beam (often referred to as Kerr angle Θ_{Kerr}) provides access to the magnetization state of the sample.
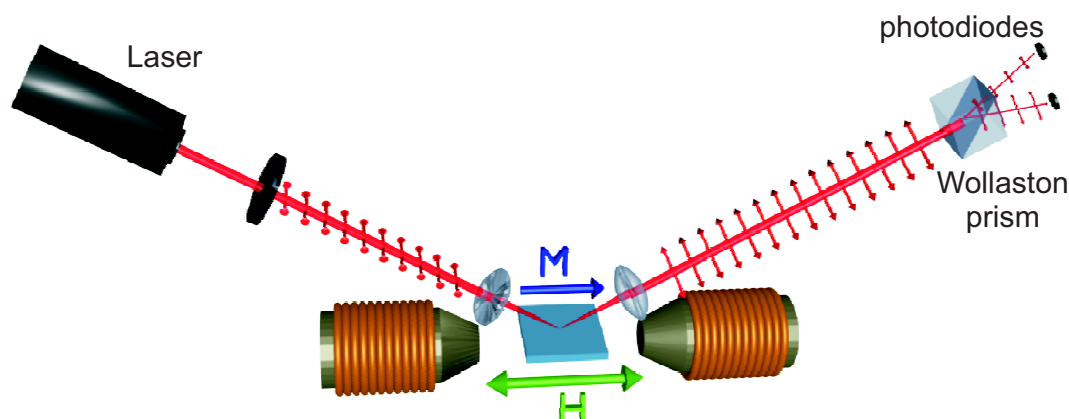
Fig. 1: Schematic setup of a longitudinal Kerr magnetometer.

With MOKE it is possible to study quasi-static magnetization reversal properties and magnetic anisotropies. When using a pulsed laser system it is also possible to study the time dependence of the magnetization under the influence of, e.g., a pulsed magnetic field or a microwave field. Since it is an optical technique it is non invasive, and the spatial resolution is only limited by the optical resolution. Thus, we are able to study the static and dynamic properties of magnetic thin films and magnetic structures with lateral dimension down to $1\,\mu$m.

Our group uses four different MOKE setups, all of them using the same principle. The light of a laser source is s-polarized through a thin-film polarizer. The beam is focused onto the sample. The polarization of the reflected light is analyzed by a detector unit that was developed and is built in our laboratory. A Wollaston prism divides the beam into two orthogonally polarized beams, which are monitored by a pair of photodiodes. The detector works as an opto-electrical bridge circuit to increase the signal-to-noise ratio. The obtained normalized differential signal $(I_1 - I_2)/(I_1 + I_2)$ is directly proportional to the Kerr angle Θ_{Kerr}.

Four experimental setups are available to investigate different scientific aspects:

Longitudinal Kerr magnetometer: Longitudinal MOKE geometry to probe quasi-static properties of magnetic thin films. Optical resolution $\sim 100\,\mu$m, magnetic field up to $2\,$T, automated sample positioning and rotation.

Microfocus Kerr microscope with rotation unit: Longitudinal MOKE geometry to probe quasi-static properties of micro-structured magnetic elements. Optical resolution $< 1\,\mu$m, magnetic field up to $0.6\,$T, automated sample positioning, rotation and stabilization.

Dual MOKE magnetometer: Two combined MOKE magnetometers working in parallel, one in longitudinal and one in polar geometry to study the quadratic MOKE effects on magnetic thin films. Optical resolution $\sim 100\,\mu$m, two orthogonal pairs of magnet coils to provide any in-plane field direction up to $0.25\,$T, automated sample positioning and rotation.

Time resolved scanning Kerr microscope: Longitudinal or polar MOKE geometry to study dynamic magnetization reversal properties of micro-structured elements. Optical resolution $<$ $500\,$nm, time resolution $\sim 60\,$ps, magnetic field up to $150\,$mT, automated sample positioning and stabilization.

References

[1] J. Kerr, *On rotation of the plane of polarization by reflection from the pole of a magnet*, Phil. Mag. **4** (5), 321 (1877).

3.4 Molecular beam epitaxy (MBE)

The Molecular Beam Epitaxy (MBE) technique involves highly controlled evaporation of materials in an ultra-high vacuum chamber (base pressure in the low $10^{-11}\,$mbar region). This deposition from the vapor phase can lead to single crystal film growth. For this reason MBE possesses a dominant role in the world of nanotechnology regarding fabrication of materials for high performance applications.

Our group operates two Molecular Beam Epitaxy (MBE) growth clusters. Both systems are equipped with tools for cleaning the substrates, for controlling the evaporation from the sources and the film deposition, for *in-situ* structural and chemical characterization, as well as sample storage.

The first cluster is called MDA (Multidepositionsanlage). The MDA has been heavily loaded this year with the growth of magnetic structures. The growth chamber contains two Knudsen cells, and one electron gun with 5 crucibles that are used to heat and evaporate the materials. The growth procedure is controlled *in-situ* by a quartz crystal. Additionally *in-situ* Low-Energy Electron Diffraction (LEED) and Auger analytics can be performed. Furthermore, the linear construction of the sample holder reduces the total time for sample preparation drastically.

Our second cluster, called MBE, contains two Knudsen cells, and one electron gun with 5 crucibles. The growth procedure is also controlled *in-situ* by a quartz crystal. One of the great advantages of our MBE system is the capability to control the *in-situ* growth by means of Reflection of High-Energy Electron Diffraction (RHEED). The characteristics of the RHEED technique is not to interfere with the deposition. An example of layer by layer deposition controlled by RHEED is shown in Fig. 1. This renders it as a unique tool for real-time structural characterization of the sample during the growth process. There is also here the option for Low-Energy Electron Diffraction (LEED) and Auger analytics.
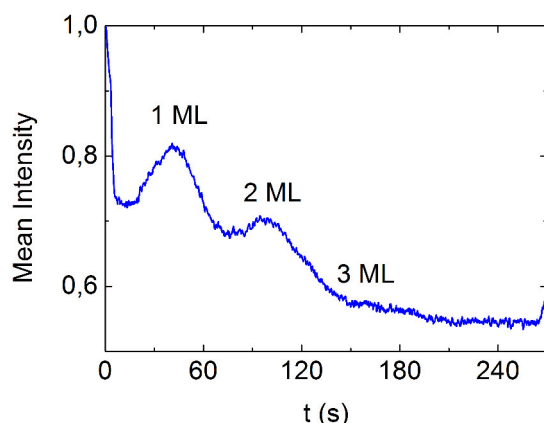
Fig. 1: RHEED oscillation observed for the growth of 3 ML Cr on top of Fe. RHEED offers unique advantages in controlling the growth procedure at the atomic level.

In addition to the aforementioned techniques and linked to the MBE, an scanning tunnelling microscope (STM) set-up is used for *in-situ* atomic probing. This increases further the capabilities of our MBE chamber. STM is a unique tool for surface investigation of the evaporated samples. The cluster includes furthermore a load chamber for inserting samples in vacuum and preparation chamber. The latter is used for cleaning the samples since there is the possibility to heat up to 800 °C the samples. Furthermore, there is an option for optical coatings. The ionization chamber is equipped with a fine-focus noble gas keV ion source. A transfer chamber connects all the parts of the growth cluster while a repository chamber is also available. The MBE chamber has another unique feature: that of *in-situ* magnetic characterization with Brillouin light scattering (BLS) spectroscopy and Kerr effect magnetometry. The applied magnetic field can reach 1.2 T. There is an option for implementation of a cryostat.

The MBE evaporation technique offers unique advantages for the fabrication of patterned samples. The good control of the film growth and the directionality of the beam renders MBE suitable to grow materials on patterned masks. Patterned samples of extreme quality can be produced either with pre- or post treatment techniques.

2016 was a very successful year for both of our growth chambers. We have produced a series of fully epitaxial Fe/Pt bilayers, see Fig. 2, as well as Fe/Au, Fe/Pd, Fe/Rh, Co/Au, Ni/Au bilayers and Pd/Fe/Pd, Fe/MgO/Pt trilayers for studies in magnetisation dynamics and magneto-plasmonics. We have also used YIG substrates to evaporate Au and Pt on top.
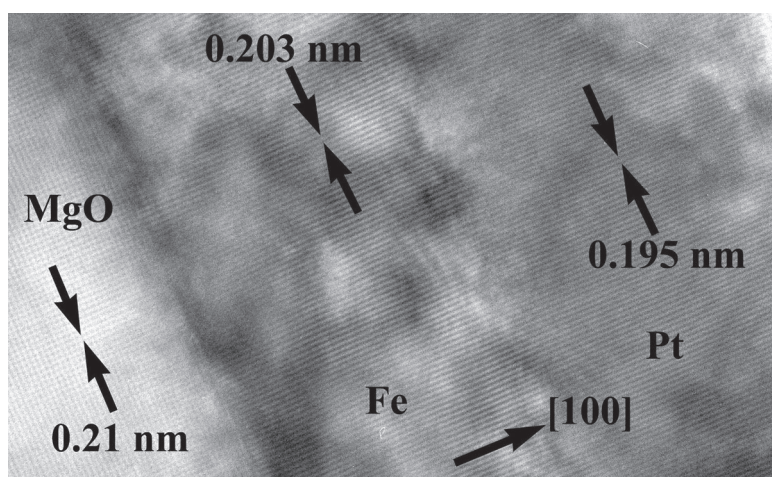
Fig. 2: Cross-sectional high resolution transmission electron microscopy image of epitaxial Fe/Pt bilayer grown on a MgO substrate. Image is taken from reference: Conca et al. PRB 93, 134405 (2016). The growth of fully epitaxial bilayers was one of the milestones regarding the growth facilities of this year.

Chapter 4: Reports on Experimental Results

A.   Magnon Gases and Condensates

In ferromagnetic materials atoms having unpaired electrons act as individual magnets. Their magnetism is mostly caused by the magnetic moments of the uncompensated electron spins. Since these atomic magnets tend to be oriented in the same direction due to quantum-mechanical exchange interaction, a macroscopic magnetic moment appears. As the atoms strongly interact, a reversal of a single atomic magnetic moment is not spatially localized but spreads through the solid as a wave of discrete magnetic momentum transfer. This wave is known as a spin wave, and in frame of second quantization it is associated with a quasi-particle named magnon. Weakly interacting magnons can be considered as a gas of magnetic bosonic quasi-particles and, therefore, this is referred to as a magnon gas.

Nowadays magnon gases are recognized as an excellent model environment for the experimental investigation of collective classical and quantum macroscopic properties of bosonic systems. Its potential is due to the wide controllability of the magnon density as well as of the spectral properties influencing the magnon-magnon interaction. For example, the dispersion branch of a magnon gas can be frequency shifted or otherwise modified by change in the strength or orientation of a bias magnetic field. The magnon population density can be effectively controlled by means of electromagnetic parametric pumping (see Gurevich and Melkov, Magnetization Oscillation and Waves, CRC, Cleveland, 1996). In the simplest case one photon of the pumping electromagnetic field excites two magnons with half the energy/frequency that propagate in opposite directions. Such a mechanism creates a huge quantity of phase correlated magnons, which are called a condensate of photon-coupled magnon pairs. The behavior of parametrically created magnon condensates, of gaseous magnon phases, and of Bose-Einstein condensates (BEC), which can be formed at the lowest energy state of a magnon gas, constitutes a hot research topic. The main goal of our work is to study the phase transition processes resulting in the formation of quantum macroscopic states of a magnon gas and to understand the role of magnon-magnon and magnon-phonon interactions in the properties of these correlated states of matter in comparison with the dynamics of ultra-cold quantum gases and quantum spin systems. We investigate the dynamics of the magnon system in a low-damping magnetic insulator (yttrium-iron-garnet, YIG) using wavevector- and time-resolved Brillouin light scattering (BLS) spectroscopy with special attention on the free evolution of the magnetic medium after pumping.

Magnonic BECs are described by a unique wavefunction, and thus they can be considered as a macroscopic quantum state. In such a state transport of energy or momentum is possible via a supercurrent mechanism, analogous to charge supercurrents in superconductivity or mass supercurrents in superfluidity. Using the concept of a magnonic macroscopic quantum state opens up a new research field for us, which is the research subject of the ERC Advanced Grant we have obtained this year.

Several very interesting findings are presented this year.

In Report 4.1 "Supercurrent in a room-temperature Bose-Einstein magnon condensate" we present the further development in the theoretical understanding of magnon supercurrents excited in a magnon BEC subject to a thermal gradient. The model is based on rate equations for the gaseous and condensed magnons. It takes into account both the temperature induced magnon supercurrent and a diffusion-like dispersive magnon counterflow. The high quantitative agreement between the experimentally determined and the analytically modelled magnon behavior at the bottom of

the magnon spectrum evidences the existence of a temperature induced supercurrent in the room-temperature magnon BEC. The reported results have been recently published in D.A. Bozhko *et al.*, "Supercurrent in a room temperature Bose-Einstein magnon condensate", Nature Physics (2016).

In Report 4.2 "Bottleneck accumulation of hybrid bosons in a ferrimagnet" we report on the discovery of a novel condensation phenomenon mediated by magneto-elastic interaction: A spontaneous accumulation of hybrid magneto-elastic bosonic quasiparticles at the intersection of the lowest magnon mode and a transversal acoustic wave. The developed theory describes the formation of the experimentally observed peak in the population of the magneto-elastic bosons as a result of a bottleneck effect in the magnon transfer from high to low energy states through the magnon-phonon hybridization region.

In Report 4.3 "Parametric excitation of magnons in YIG films at low temperatures" we investigate the relaxation of parametrically excited dipolar and exchange magnons in the temperature range from 40 K to 340 K. We have done this to pave the way to deepen our insight into the mechanisms underlying the formation of a magnon BEC. We have found that in a YIG film epitaxially grown on a gallium-gadolinium-garnet (GGG) substrate the magnon lifetime strongly decrease at cryogenic temperatures. The observed relaxation behavior is related to the magnetic damping caused by dipolar coupling of magnons to the paramagnetic spin system of the GGG substrate.

A. Magnonengase und -kondensate

In ferromagnetischen Materialien treten Atome, die ungepaarte Elektronen haben, als einzelne elementare Magnete auf. Ihr Magnetismus wird in der Regel durch die magnetischen Momente des nicht kompensierten Elektronenspins verursacht. Diese atomaren Magnete richten sich häufig aufgrund der quantenmechanischen Austauschwechselwirkung in einem Ferromagneten parallel zueinander aus. Daher beobachtet man ein makroskopisches magnetisches Moment. Da die Atome stark miteinander wechselwirken, wird das Umklappen eines einzelnen atomaren magnetischen Moments nicht räumlich lokalisiert sein, sondern breitet sich als Welle mit einem diskreten magnetischen Moment über den gesamten Festkörper aus. Diese Welle wird als Spinwelle bezeichnet und ist im Rahmen der zweiten Quantisierung mit einem Quasiteilchen, dem so genannten Magnon, verbunden. Schwach miteinander wechselwirkende Magnonen können als Gas von magnetischen bosonischen Quasiteilchen angesehen werden und werden daher auch als Magnonengas bezeichnet.

Magnonengase sind unlängst als hervorragendes Modellsystem erkannt worden und dienen zur Untersuchung von korrelierten bosonischen Systemen mit sowohl klassischen Eigenschaften als auch makroskopischen Quanteneigenschaften. Ihr Potenzial liegt dabei in der guten Kontrollierbarkeit der Magnonendichte und den Eigenschaften des Spektrums, welches die Magnon-Magnon-Wechselwirkung beeinflusst. Zum Beispiel kann durch die Änderung der Richtung oder der Stärke eines externen Magnetfelds das Spektrum des Magnonengases in der Frequenz verschoben oder auch stark verändert werden. Der wirkungsvollste Mechanismus, die Dichte eines Magnonengases zu erhöhen, ist parametrisches Pumpen mittels Mikrowellen (s. Gurevich und Melkov, Magnetization Oscillation and Waves, CRC, Cleveland, 1996). Im einfachsten Fall erzeugt ein Photon des elektromagnetischen Pumpfeldes zwei Magnonen mit je der Hälfte der Energie/Frequenz des Photons, die sich in entgegengesetzte Richtungen ausbreiten. Dieser Mechanismus erzeugt eine große Anzahl von phasenkorrelierten Magnonen, ein sogenanntes Kondensat von photonengekoppelten Magnonenpaaren. Die Verhaltensweisen parametrisch erzeugter Magnonenkondensate, gasförmiger Magnonenzustände, und von magnonischen Bose-Einstein-Kondensaten (BEC), welche

im Zustand niedrigster Energie des Magnonengases erzeugt werden können, bilden ein aktuelles Forschungsthema. Das Hauptziel unserer Forschung ist die Untersuchung der Phasenübergänge, die zu der Bildung von Zuständen mit makroskopischen Quanteneigenschaften in Magnonengasen führen, und das Verständnis der Funktion der Viel-Magnonen-Wechselwirkungen in diesen korrelierten Zuständen der Materie im Vergleich mit der Dynamik von ultrakalten Quantengasen und Quanten-Spinsystemen. Wir untersuchen die Dynamik des Magnonensystems in einem magnetischen Isolator mit niedriger Dämpfung (Yttrium-Eisen-Granat, YIG) mit Hilfe von wellenvektor- und zeitaufgelöster Brillouin-Lichtstreuspektroskopie mit besonderem Augenmerk auf die pumpfreie Entwicklung des magnetischen Mediums nach dem Pumpprozess.

Magnonische BECs werden durch eine wohldefinierte Wellenfunktion beschreiben. Daher kann man sie als einen makroskopischen Quantenzustand auffassen. In solch einem Zustand kann Transport von Energie oder Drehimpuls durch einen Suprastrom-Mechanismus stattfinden, analog zu einem Ladungs-Suprastrom in der Supraleitung oder zu einem Teilchen-Suprastrom in der Suprafluidität. Das Konzept eines magnonischen makroskopischen Quantenzustands öffnet für uns ein neues Forschungsfeld. Dies ist auch der Forschungsgegenstand des in diesem Jahr eingeworbenen ERC-Advanced Grants.

Dieses Jahr werden einige sehr interessante Ergebnisse vorgestellt.

Im dem Bericht 4.1 "Supercurrent in a room-temperature Bose-Einstein magnon condensate" präsentieren wir die Verbesserung des theoretischen Verständnisses von Magnonen-Supraströmen, die durch einen thermischen Gradienten in einem Magnonen-BEC angeregt werden. Das Model basiert auf den Ratengleichungen für die gasförmigen und kondensierten Magnonen. Es berücksichtigt beides, die durch die Temperatur induzierte Magnonen-Supraströme sowie den diffusionsähnlichen dispergierenden Magnonen-Gegenstroms. Die hohe quantitative Übereinstimmung zwischen den experimentellen Daten und dem analytisch modellierten Verhalten der Magnonen am Boden des Spektrums, weist auf die Existenz von Temperatur induzierten Supraströmen hin, welche in Magnonen-BECs bei Raumtemperatur auftreten. Die gezeigten Resultate wurden kürzlich in D.A. Bozhko *et al.*, "Supercurrent in a room temperature Bose-Einstein magnon condesate", Nature Physics (2016) veröffentlicht.

Im Bericht 4.2 "Bottleneck accumulation of hybrid bosons in a ferrimagnet" zeigen wir die Entdeckung eines neuen Kondensationsphänomens welches durch die magnetoelastische Interaktion entsteht: Eine spontane Ansammlung von hybriden magnetoelastischen bosonischen Quasiteilchen an dem Schnittpunkt der untersten Magnonenmode und einer transversalen akustischen Welle. Die entwickelte Theorie beschreibt die Bildung des experimentell beobachteten Anstiegs der Magnonenpopulation, der magnetoelastischen Bosonen als Resultat des Engpasses im Transfer der Magnonen von hohen zu niedrigen Engeriezuständen, dabei wird der Engpass durch die Magnonen-Phononen Hybridisierungsregion verursacht.

Im Bericht 4.3 "Parametric excitation of magnons in YIG films at low temperatures" untersuchen wir die Relaxation parametrisch angeregter Magnonen im Dipol- und Austauschregime in einem Temperaturbereich von $40\,\mathrm{K}$ bis $340\,\mathrm{K}$. Das Ziel dabei ist ein tieferes Verstädnis des zugrundeliegenden Prozesses für die Erzeugung von Magnonen-BECs zu gewinnen. Wir fanden heraus, dass sich in einer YIG Schicht, die epitaktisch auf einem Gallium-Gadolinium-Granat (GGG) Substrat gewachsen ist, die Lebenszeit der Magnonen für tiefe Temperaturen stark verringert. Das beobachtete Relaxationsverhalten ist mit der magnetischen Dämpfung verknüpft, diese beruht dabei auf der Dipolkopplung zwischen Magnonen und dem paramagnetischen Spinsystem des GGG Substrates.

4.1   Supercurrent in a room-temperature Bose-Einstein magnon condensate

D.A. Bozhko, A.A. Serga, P. Clausen, V.I. Vasyuchka, F. Heussner, and B. Hillebrands

In collaboration with A. Pomyalov and V.S. L'vov, Department of Chemical Physics, Weizmann Institute of Science, 76100 Rehovot, Israel;
G.A. Melkov, Faculty of Radiophysics, Electronics and Computer Systems, Taras Shevchenko National University of Kyiv, 01601 Kyiv, Ukraine

A supercurrent is a macroscopic effect of a phase-induced collective motion of a quantum condensate. So far, experimentally observed supercurrent phenomena such as superconductivity and superfluidity have been restricted to cryogenic temperatures. Recently, we reported on the discovery of a supercurrent in a Bose-Einstein condensate (BEC) of magnons prepared in a room-temperature yttrium iron garnet (YIG) film [1, 2]. The magnon condensate was formed in a parametrically pumped magnon gas and was subject to a thermal gradient created by local laser heating of the film. The appearance of the supercurrent driven by a thermally induced phase shift in the condensate wavefunction is evidenced by analysis of the temporal evolution of the magnon density measured by means of Brillouin light scattering (BLS) spectroscopy. Laser heating locally changes the saturation magnetization and, thus, induces a weak frequency shift $\delta\omega_c$ between different parts of the magnon condensate. In the course of time this frequency shift results in an increasing phase gradient in the magnon BEC. As a result, a phase-gradient-induced magnon current or, in other words, a magnon supercurrent, flowing out of the hot region of the focal spot, is excited. This efflux reduces the density of the magnon BEC in the probing point. After some time, the enhanced decrease in the magnon density results in the disappearance of the condensate, and thus in the disappearance of the supercurrent. Consequently, this leads to the recovery of the conventional relaxation dynamics which exists in the residual incoherent gaseous magnon phase.

In this Report we present a quantitative model to describe our experimental findings [1,2]. To quantify our interpretation, that a magnon supercurrent is acting, recall that a BEC of magnons can be described by the Gross-Pitaevskii equation for the complex wave function $C(\boldsymbol{r},t) = \sqrt{N_c}\exp(i\varphi)$, where $N_c(\boldsymbol{r},t)$ and $\varphi(\boldsymbol{r},t)$ are the magnon number density per unit volume and the BEC phase, respectively. This equation is the well known equation for the envelope of a narrow wave packet (see e.g. Refs. [3,4]). It conserves the total number of condensed magnons $\mathcal{N}_c = \int N_c(\boldsymbol{r},t)\,d\boldsymbol{r}$ and leads to the continuity equation for the BEC density $N_c(\boldsymbol{r},t)$:

$$\frac{\partial N_c}{\partial t} + \nabla \cdot \boldsymbol{J} = 0, \quad J_i = \frac{N_c}{2}\sum_j \frac{\partial^2 \omega(\boldsymbol{q})}{\partial q_i \partial q_j}\frac{\partial \varphi}{\partial r_j}\,. \tag{1}$$

Here $\boldsymbol{J}(\boldsymbol{r},t)$ is a supercurrent formed by the BEC magnons. In the (x,y)-plane of a YIG film (see Fig. 1) it has two components $J_x = N_c D_x \partial\varphi/\partial x$, $J_y = N_c D_y \partial\varphi/\partial y$, where $D_x = d^2\omega(\boldsymbol{q})/(2\,dq_x^2)$ and $D_y = d^2\omega(\boldsymbol{q})/(2\,dq_y^2)$ are the anisotropic dispersion coefficients. At our experimental conditions $D_x \simeq 21 D_y$ and, thus, $J_x \gg J_y$. This allows us to neglect J_y in the global balance of the magnon numbers and to simplify the problem to a 1D case along the x-axis, see Fig. 1b,c.
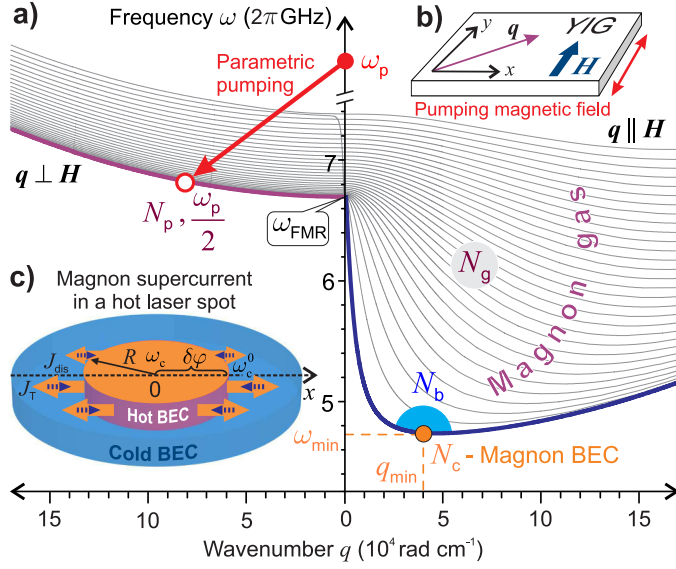

Fig. 1: a) Magnon spectrum of a 5.6 μm-thick in-plane magnetized YIG film. The arrow illustrates the magnon injection process by means of parallel parametric pumping. N_p – total number of parametrically excited magnons at $\omega_p/2$; N_c – number of BEC magnons at $\omega_c = \omega_{min}$; N_b – number of gaseous magnons near ω_{min} and q_{min}; N_g – number of magnons in the parametrically overpopulated gas of magnons below $\omega_p/2$. b) The geometry of the in-plane magnon wavevector q, the bias field H, and the pumping microwave magnetic field. c) The schematic illustration of a supercurrent flowing in the magnon BEC subject to a thermal gradient.

There are two reasons for the x-dependence of the BEC phase φ in our experiment. The first one is the already mentioned temperature dependence of ω_c. Within the hot spot of radius R centered at $x = 0$ (i.e. for $|x| < R$) the temperature $T(x)$ is higher than the temperature T_0 of the rest of the film. (Fig. 1c). Since in an in-plane magnetized YIG film $d\omega_c(T)/dT < 0$, the BEC frequency in the spot is smaller than outside: $\delta\omega_c(x) = \omega_c(T(x)) - \omega_c(T_0) < 0$. Correspondingly, the phase accumulation $\delta\varphi(x) = \delta\omega_c(x)t$ inside of the spot is smaller than in the surrounding cold film. Therefore, the phase gradient $\partial\delta\varphi(x)/\partial x$ is positive for $x > 0$ and negative for $x < 0$. It means that a thermally induced supercurrent flows out from the spot (mostly in x-direction) as it is shown by solid arrows in Fig. 1c: $J_T(x) = N_c D_x \partial(\delta\omega_c t)/\partial x$. This outflow decreases the magnon BEC density $N_c(x)$ in the spot, $|x| < R$, with respect of that in the cold film, where $N_c(x \gg R) = N_c^0$.

Spatial deviations in the density $N_c(x)$ of the magnon condensate constitute the second reason for the variation of its phase $\partial\varphi/\partial x \neq 0$. It results in an additional contribution to the supercurrent given by Eq. (1), which can be named a "dispersive" current J_{dis}. In order to estimate J_{dis} notice that the 1D Gross-Pitaevskii equation has the self-similar solution $C(x,t) = \mathscr{F}(\xi)$ with $\xi = x^2/(D_x t)$, where the function $\mathscr{F}(\xi)$ satisfies the ordinary differential equation $\xi d\mathscr{F}/d\xi = i(d\mathscr{F}/d\xi + 2\xi d^2\mathscr{F}/d\xi^2)$. It describes the well known phenomenon of dispersive spreading of a wave packet with the width $\delta x = \sqrt{D_x t}$ permanently increasing in time. It is worth to notice that exactly the same law is satisfied by the diffusion process with the diffusion current $J_{dif}(x) = D_x(\partial N_c(x)/\partial x)$. Ignoring the difference between the self-similar profiles in the dispersion and the diffusion processes (it is well below the resolution of our experiment), we can estimate the dispersive current J_{dis} by its diffusion counterpart: $J_{dis}(x) \simeq -D_x \partial N_c(x)/\partial x$. This current is directed to the lower $N(x)$ region, i.e. towards the hot spot as shown in Fig. 1c by dashed arrows.

We describe the evolution of a parametrically driven magnon system towards BEC by rate equations for the total number of magnons in particularly chosen parts of the q-space shown in Fig. 1a. The first part is the BEC with density N_c (solid dot at the bottom of the magnon spectrum in Fig. 1a). The second one is the magnon gas with density N_b at the bottom of the magnon spectrum in close vicinity to the BEC (semi-circle area $\mathbb{R}_b$ surrounding the BEC point in Fig. 1a). These parts are directly coupled via four-magnon scattering processes ($\mathbb{R}_b \to$ BEC) and are *simultaneously* detected due to the finite resolution of our frequency- and wavenumber-resolved BLS setup. The third part is given by the magnon gas area $\mathbb{R}_g$ above $\mathbb{R}_b$. In our simplified model the parametri-

cally injected magnons of density N_p (open dot in Fig. 1a) populate first the gas area $\mathbb{R}_g$ ($N_p \to \mathbb{R}_g$) and afterwards move to the bottom part $\mathbb{R}_b$ of the magnon spectrum due to four-magnon scattering processes between these areas ($\mathbb{R}_g \rightleftarrows \mathbb{R}_b$).

In the rate equations for the magnon numbers N_g, N_b and N_c we have to account that the kinetic equations for the four-magnon scattering processes conserve the total number of magnons and that the leading term for the magnon flux from the j to the i sub-system is proportional to N_j^3 and can be written as $A_{ij}N_j^3$ with A_{ij} being dimensional (s^{-1}) phenomenological constants. Thus, the rate equations take the following form:

$$\frac{\partial N_g}{\partial t} = -\Gamma_g N_g + \Gamma_g N_p e^{-\Gamma_0 t} - A_{gb}N_g^3 + A_{bg}N_b^3, \tag{2-a}$$

$$\frac{\partial N_b}{\partial t} = -\Gamma_b N_b + A_{gb}N_g^3 - A_{bg}N_b^3 - A_{bc}(N_b^3 - N_{cr}^3)\Theta(N_b - N_{cr}), \tag{2-b}$$

$$\frac{\partial N_c}{\partial t} = -\Gamma_c N_c + A_{bc}(N_b^3 - N_{cr}^3)\Theta(N_b - N_{cr}) - \frac{\partial J}{\partial x}. \tag{2-c}$$

Here Γ_g, Γ_b and Γ_c are relaxation frequencies of corresponding magnons in the processes that do not conserve magnon numbers (mainly caused by spin-orbit interaction). Their experimental values are close enough and for simplicity are replaced by the same mean value $\Gamma = 6.1\,\text{MHz}$.

The second term in the right-hand-side of Eq. (2-a) represents the external magnon source and is proportional to the number of parametrically pumped magnons N_p. The factor $\exp(-\Gamma_0 t)$ models the processes of magnon thermalization after the end of the pump pulse. The terms $\propto A_{ij}$ in Eqs. (2) describe the magnon fluxes between the chosen spectral areas, leading finally to the population of the BEC state. The flux $\mathbb{R}_b \to \mathbb{R}_c$ contains the Heaviside function $\Theta(N_b - N_{cr})$ that involves N_{cr}— a critical number of magnons at which the chemical potential μ of the magnon gas reaches $\omega_{\min}$. The function $\Theta(N_b - N_{cr}) = 1$ for $N_b - N_{cr} > 0$ and 0 otherwise. Therefore, for $N_b \leq N_{cr}$ there is no flux of magnons to the condensate. For $N_b > N_{cr}$ this flux appears and an excess of magnons $N_b - N_{cr}$ populates the condensate.

In a numerical solution of this model we have chosen the initial BEC value $N_c = 0$ because the gaseous magnons do not populate the lowest energy state in the case of powerful pumping [5]. In such cases, no magnon condensation occurs during the pump action and the BEC in the global energy minimum $(\omega_{\min}, q_{\min})$ is formed *after* the termination of the pump pulse. The initial value of $N_b = 135$ (in units of BLS counts) was taken from our experiment (measured value $N_b + N_c$ at $t = 0$ in Fig. 2). The initial values $N_p = 250$ and $N_g = 1000$ are found from the best fit to the reference case of no heating, shown by the first solid line in Fig. 2.

As we have discussed above, the supercurrent J in Eq. (2-c) consists of two parts: $J = J_T + J_{dis}$. Their modelling is, probably, the most delicate issue. We adopt the simplest version, assuming a constant temperature gradient from the center ($x = 0$) of the heated spot to R:

$$J = -B_s N_c \delta \omega_c t + B_{dis}(N_c^0 - N_c), \text{ where } B_s \sim B_{dis} \sim -D_x/R. \tag{3}$$

The results of the numerical solution of Eqs. (2) and (3) for different T in the center of the hot spot and, accordingly, for different $\delta\omega_c(T)$, are shown in Fig. 2 by smooth solid lines together with the respective experimental data. One clearly sees the good agreement between the theoretical and experimental curves. The initial rise of the theoretical curves occurs faster than in the experiment. This is likely due to our simplified model with only three zones in the q-space. We ignore here the multistage character of the $N_p \to \mathbb{R}_g$ magnon transfer.
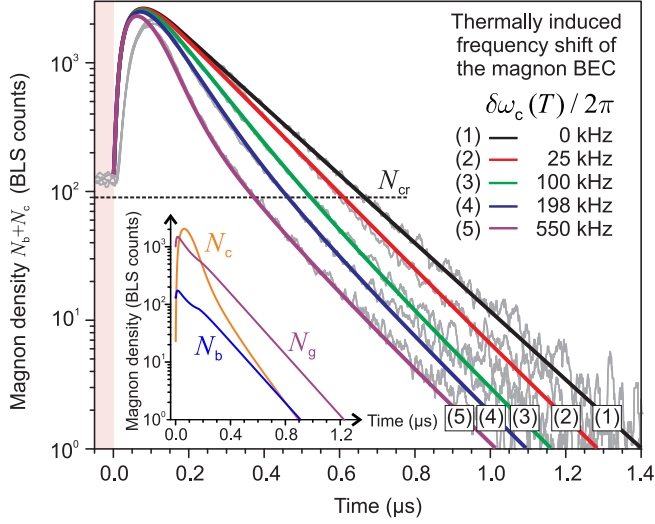
Fig. 2: Theoretically calculated magnon dynamics in a thermal gradient. Theoretical dependencies (smooth solid lines 1-5) of the observable magnon densities $(N_c + N_b)$ calculated according to Eqs. (2) for different temperature dependent shifts $\delta\omega_c(T)$ of the BEC frequency ω_c are shown in comparison with the corresponding experimental data (noisy gray curves). The inset shows the calculated temporal behaviour of N_c, N_b, and N_g for the case of the strongest heating of the magnon BEC.

In the comparison of our model with experiments performed at different spot temperatures T, we used only one T-dependent parameter $\delta\omega_c(T)$, related to the temperature dependence of the saturation magnetization $M(T)$ of YIG at standard ambient conditions $dM(T)/dT \simeq -4\,\mathrm{G/K}$ giving $d\omega_c/dT = -116\,\mathrm{kHz/K}$. For the largest frequency shift ($\delta\omega_c = 550\,\mathrm{kHz}$), assumed in our calculations, it requires a rather mild heating of the spot by about 4.7 K. This value agrees well with a numerically found temperature rise of 5.7 K in the center of the focal spot. This value was obtained by solving a 3D heat conduction model in the COMSOL Multiphysics simulation package using known values of the light absorption coefficient, heat capacity, duration of the laser pulse, etc.

To summarize, we proposed and analyzed a model based on rate equations for the gaseous and condensed magnons, taking into account both the temperature induced magnon supercurrent and the diffusion-like dispersive magnon counterflow via the boundary of the hot spot. The high quantitative agreement between the measured data and the analytically modelled magnon evolution at the bottom of the magnon spectrum serves as strong support in favor of the existence of a temperature-induced supercurrent in the Bose-Einstein magnon condensate.

References

[1] P. Clausen, D.A. Bozhko, V.I. Vasyuchka, B. Hillebrands, A.A. Serga, *Magnon supercurrent in a magnon Bose-Einstein condensate subject to a thermal gradient*, Annual Report 2015: http://www.physik.uni-kl.de/hillebrands/publications/annual-reports/annual-report-2015/.

[2] D.A. Bozhko, A.A. Serga, P. Clausen, V.I. Vasyuchka, F. Heussner, G.A. Melkov, A. Pomyalov, V.S. L'vov, B. Hillebrands, *Supercurrent in a room-temperature Bose-Einstein magnon condensate*, Nature Physics **12**, 1057 (2016).

[3] L.D. Landau, E.M. Lifshitz, *Quantum mechanics (Non-relativistic theory), Course of theoretical physics*, 3rd edn, Vol. 3, (Pergamon Press, Oxford, 1977).

[4] V.S. L'vov, *Wave turbulence under parametric excitations (Applications to magnetics)*, (Springer, Berlin, 1994).

[5] A.A. Serga, V.S. Tiberkevich, C.W. Sandweg, V.I. Vasyuchka, D.A. Bozhko, A.V. Chumak, T. Neumann, B. Obry, G.A. Melkov, A.N. Slavin, B. Hillebrands, *Bose-Einstein condensation in an ultra-hot gas of pumped magnons*, Nat. Commun. **5**, 3452 (2014).

4.2 Bottleneck accumulation of hybrid bosons in a ferrimagnet

D.A. Bozhko, P. Clausen, V.I. Vasyuchka, A.V. Chumak, B. Hillebrands, and A.A. Serga

In collaboration with A. Pomyalov and V.S. L'vov, Department of Chemical Physics, Weizmann Institute of Science, 76100 Rehovot, Israel;
G.A. Melkov, Faculty of Radiophysics, Electronics and Computer Systems, Taras Shevchenko National University of Kyiv, 01601 Kyiv, Ukraine

Our studies of the magnon Bose-Einstein condensate (BEC) in a film of yttrium iron garnet ($Y_3Fe_5O_{12}$, YIG) resulted in the discovery of a novel condensation phenomenon mediated by magneto-elastic interaction: A spontaneous accumulation of hybrid magneto-elastic bosonic quasi-particles at the intersection of the lowest spin-wave mode and a transversal acoustic wave.

We studied a magnon gas populated by parametric microwave pumping in an in-plane magnetized 6.7 μm thick YIG film by wavevector-resolved Brillouin light scattering spectroscopy (BLS) [1]. The pumping circuit (see Fig. 1a) is fed with 1.5 μs long microwave pulses with a carrier frequency $f_p = 13.62$ GHz. A microstrip resonator with a width of 0.5 mm creates an alternating Oersted field along the direction of a bias magnetic field, realizing, thus, parallel parametric pumping [2].

BLS intensity maps showing the population of the pumped magnon spectrum (an example is shown in Fig. 1b as a function of frequency and wavenumber are presented in Fig. 2a-b for two different bias magnetic fields and a relatively small pumping power of 2.6 W. In spite of the fact that the threshold of magnon BEC formation is still not reached at such power levels one can see a strong and sharp population peak, which appears in the region of the hybridization between the magnon and the transversal acoustic phonon dispersion branches (see white lines in Fig. 2). When the bias magnetic field is shifted from 1735 Oe to 1265 Oe, the population peak shifts in frequency and wavenumber together with the magneto-elastic crossover region. At the same time, there are no peculiarities in the thermal spectrum, measured at the same conditions, but without application of pumping (see Fig. 2c). It means that the observed phenomenon is associated with the accu-
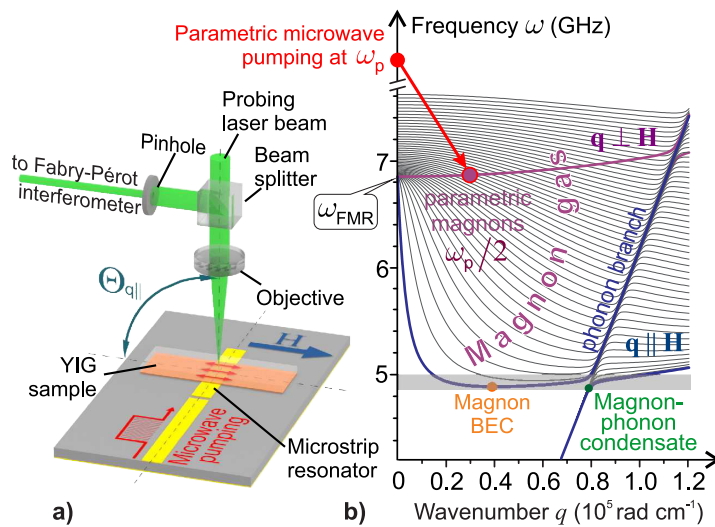
Fig. 1: a) Experimental setup. The probing laser beam is focused onto a spot with 25 μm diameter on a YIG film placed on top of a microstrip resonator. The light inelastically scattered by magnons is redirected to a Fabry-Pérot interferometer for frequency and intensity analysis. Wavenumber-selective probing of magnons with wavevectors $\pm \mathbf{q} \parallel \mathbf{H}$ is realized by varying the angle of light incidence $\Theta_{q\parallel}$. b) Magnon-phonon spectrum of a 6.7 μm-thick YIG film for $H = 1735$ Oe. 47 thickness modes with $\mathbf{q} \parallel \mathbf{H}$ are presented. The upper thick curve shows the lowest mode with $\mathbf{q} \perp \mathbf{H}$. The arrow illustrates the magnon injection process.
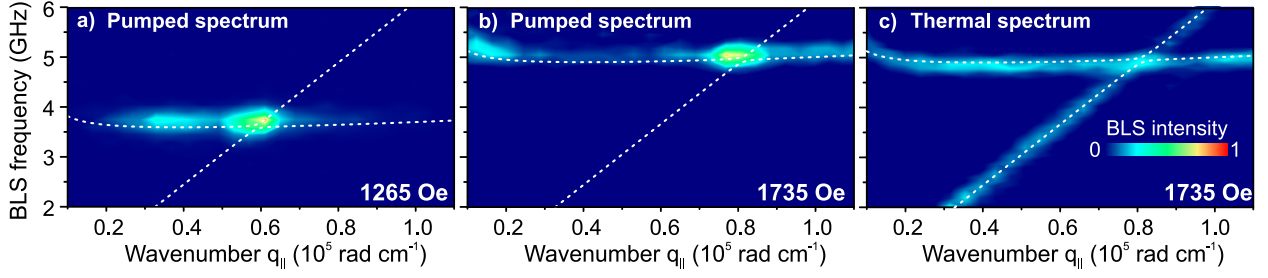
Fig. 2: Magnon-phonon spectra and their population under different pumping conditions. White dashed lines represent the calculated dispersion relation for the lowest magnon branch ($\mathbf{q} \parallel \mathbf{H}$), hybridized with a transversal acoustic mode. Strong population of states at the magnon-phonon hybridization area is clearly visible in the parametrically pumped spectra. No distinct peculiarities in the thermal magnon spectrum are detected.

mulation of hybrid magnon-phonon quasi-particles at the crossover region in the process of the thermalization of an externally populated magnon gas.

A microwave electromagnetic field with frequency ω_p and wavenumber $k_p \approx 0$ excites parametric magnons distributed over the isofrequency surface at $\omega_{\mathbf{q}}^m = \omega_p/2$. Due to $2 \Rightarrow 2$ four-magnon scattering, which satisfies the conservation laws $\omega_{\mathbf{q}_1}^m + \omega_{\mathbf{q}_2}^m = \omega_{\mathbf{q}_3}^m + \omega_{\mathbf{q}_4}^m$ and $\mathbf{q}_1 + \mathbf{q}_2 = \mathbf{q}_3 + \mathbf{q}_4$, parametrically exited magnons redistribute over the entire $\mathbf{q}$-space such that the magnon number $n(\mathbf{q})$ moves toward lower frequencies. At relatively high frequencies the main contribution to the scattering amplitude $T_{\mathbf{q}_1,\mathbf{q}_2:\mathbf{q}_3,\mathbf{q}_4}$ is given by the exchange interaction for which $T_q \equiv T_{\mathbf{q},\mathbf{q}:\mathbf{q},\mathbf{q}} \propto q^2$. Therefore, the most efficiently thermalized magnons have the largest wavenumbers q and, thus, for the case of an in-plane magnetized YIG film, belong to the lowest magnon mode with $\mathbf{q} \parallel \mathbf{H}$ [3,4].

In the presence of magnon-phonon coupling the unperturbed magnon $\omega_{\mathbf{q}}^m$ and phonon $\omega_{\mathbf{q}}^p$ spectra, shown in Fig. 3a by dashed lines, split up in the Upper and Lower Magneto-Elastic Modes (U-MEM, $\Omega_{\mathbf{q}}^U$ and L-MEM, $\Omega_{\mathbf{q}}^L$), shown in Fig. 3a by solid lines. The population dynamics of these modes is determined by both intramodal ($2L \Rightarrow 2L$, $2U \Rightarrow 2U$) and intermodal ($2L \Rightarrow 2U$) scattering of hybrid magneto-elastic bosons with the following conservation laws and interaction amplitudes:

$$\Omega_{\mathbf{q}_1}^L + \Omega_{\mathbf{q}_2}^L = \Omega_{\mathbf{q}_3}^L + \Omega_{\mathbf{q}_4}^L, \quad T_{q_1,q_2:q_3,q_4}^{LL}, \tag{1a}$$

$$\Omega_{\mathbf{q}_1}^U + \Omega_{\mathbf{q}_2}^U = \Omega_{\mathbf{q}_3}^U + \Omega_{\mathbf{q}_4}^U, \quad T_{q_1,q_2:q_3,q_4}^{UU}, \tag{1b}$$

$$\Omega_{\mathbf{q}_1}^L + \Omega_{\mathbf{q}_2}^L = \Omega_{\mathbf{q}_3}^U + \Omega_{\mathbf{q}_4}^U, \quad T_{q_1,q_2:q_3,q_4}^{LU}. \tag{1c}$$

All interaction amplitudes $T_{q_1,q_2:q_3,q_4}^{\cdots}$ originate from the four-magnon interaction amplitude $T_{q_1,q_2:q_3,q_4}$ and, thus, are proportional to the magnon contribution to MEMs. It can be shown that this contribution is given by $\cos\varphi_q$ regarding the L-MEM and $\sin\varphi_q$ regarding the U-MEM, whose values are determined by the dimensionless frequency distance from the crossover o_q:

$$\cos\varphi_q = \sqrt{(1 + o_q(o_q^2 + 1)^{-1/2})/2}, \quad o_q = (\omega_q^p - \omega_q^m)/\Delta, \tag{2}$$

where $\Delta = \Omega_{\mathbf{q}_0}^U - \Omega_{\mathbf{q}_0}^L$ is the magneto-elastic frequency and $\mathbf{q}_0$ is the crossover wavevector at which $\omega_{\mathbf{q}_0}^p = \omega_{\mathbf{q}_0}^m \equiv \omega_0$. In particular

$$T_q^{LL} = T_0 \cos^4\varphi_q, \quad T_q^{LU} = T_q \cos^2\varphi_q \sin^2\varphi_q, \tag{3}$$
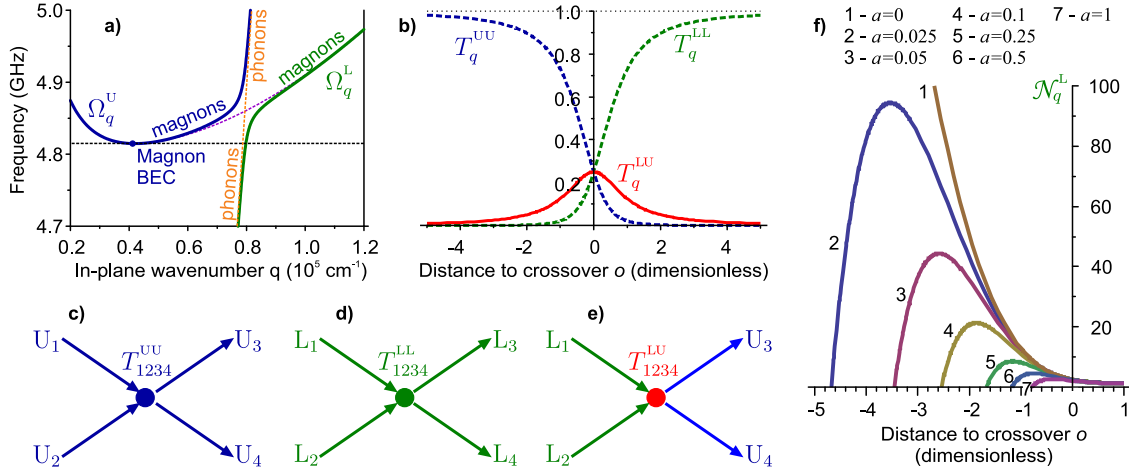
Fig. 3: Theory. a) Calculated magnon-phonon spectrum near the hybridization region. b) Interaction amplitudes T_q^{UU}, T_q^{LL} and T_q^{UL}, normalized by T_0, vs dimensionless distance from the hybridization crossover o. c)-e) Schematic representation of the scattering and cross-scattering 4-particle processes in the hybridization region. f) Dimensionless L-MEM density $\mathcal{N}_q^L$, for different values of parameter a.

and $T_q^{UU} \simeq T_q \sin^4 \varphi_q$, where $T_q^{...} \equiv T_{q,q;q,q}^{...}$. Plots of T_q^{LL}, T_q^{LU} and T_q^{UU} vs. o_q are shown in Fig. 3b.

As expected, for positive o (when $q > q_0$), the L-MEM becomes a pure magnon mode and $T_q^{LL} \to T_q$, while $T_q^{UU} \to 0$ because the U-MEM becomes a pure phonon mode (see Figs. 3a and 3b. The cross-amplitude T_q^{LU} requires the presence of magnon parts both in the L- and U-MEMs, therefore its value is significant only in the hybridization region, where $|o| \lesssim 1$, as shown by the solid line in Fig. 3b. As it is clear from Fig. 3b, for $o > 1$ we can take into account only the intramodal 2L$\Rightarrow$2L scattering described by Eq. (1a), which conserves the total number $\int N_q^L dq$ of L-MEM quasi-particles. This allows us to write the balance equation for N_q^L in the form of the continuity equation

$$\partial N_q^L(t)/\partial t + \partial \mu_q^L/\partial q = 0, \quad \text{where } \mu_q \text{ is the L-MEM flux towards the hybridisation area.} \quad (4)$$

Using a classical Hamiltonian approach we estimated μ_q in the vicinity of the hybridization as

$$\mu_q^L \simeq q_0^3 (T_q^{LL})^2 (N_q^L)^3 / \omega_0 . \quad (5)$$

In the steady-state Eq. (4), which neglects the intermodal 2L$\Rightarrow$2U scattering described by Eq. (1c), the flux μ_q^L should be q independent. Together with Eq. (3) this gives

$$N_q^L \propto (T_q^{LL})^{-2/3} \propto 1/(\cos^{8/3} \varphi_q) = \left[(1 + o_q(o_q^2 + 1)^{-1/2})/2 \right]^{-4/3}, \quad (6)$$

i.e. a fast population increase, as shown in Fig. 3f by curve 1. We call this effect "*bottleneck accumulations of magneto-elastic bosons in the hybridization region*".

When ω goes down below ω_0, the magnon part in the L-MEM goes to zero and $N_q^L \to \infty$. However, the direct particle transfer from lower to higher MEMs makes N_q^L finite. This effect is proportional to $|T_q^{LU}|^2$, shown in Fig. 3b by the solid line. In the presence of this process the steady-state balance equation (4) takes the form:

$$d\mu_q^L/dq = F_q^{LU} , \quad (7)$$

AG MAGNETISMUS
TU KAISERSLAUTERN

where F_q^{LU} is the transport rate $N_q^{\mathrm{L}} \to N_q^{\mathrm{U}}$ caused by the intermodal 2L$\Rightarrow$2U scattering. The F_q^{LU} can be estimated as

$$F_q^{\mathrm{LU}} \simeq q^2 (T_q^{\mathrm{LU}})^2 (N_q^{\mathrm{L}})^2 N_-^{\mathrm{U}}/\omega_q , \qquad (8)$$

where N_-^{U} is the density of U-MEMs at a sufficiently large negative o, say for $o \simeq -5$. Using estimates (3), (5) and (8) the balance Eq. (7) can be presented as:

$$\frac{d}{dq}\Big[\cos^8 \varphi_q (\mathscr{N}_q^{\mathrm{L}})^3\Big] = 3a\,(\mathscr{N}_q^{\mathrm{L}})^2 \cos^4 \varphi_q \sin^4 \varphi_q . \qquad (9)$$

Here, $\mathscr{N}_q^{\mathrm{L}} = N_q^{\mathrm{L}}/N_+^{\mathrm{L}}$ is the dimensionless L-MEM density, normalized by the density N_+^{L} at a sufficiently large positive o, say at $o \simeq +5$. The dimensionless damping parameter $a = bN_-^{\mathrm{U}}/N_+^{\mathrm{L}}$ contains the dimensionless coefficient b (presumably of the order of unity) comprising numerical parameters that were not controlled in the estimates (5) and (8). The ordinary differential equation (9) can be solved in quadratures with the boundary conditions $\lim_{q\to\infty} \mathscr{N}_q^{\mathrm{L}} = 1$, giving the relative L-MEM population in the hybridization region

$$\mathscr{N}_q^{\mathrm{L}} = \frac{1}{\cos^{8/3} \varphi_q}\Big[1 - a \int_q^\infty \frac{\sin^4 \varphi_p\, dp}{\cos^{4/3}\varphi_p}\Big] . \qquad (10)$$

Solutions of Eq. (10) for different values of a are shown in Fig. 3f. For $a = 0$ we return to Eq. (6) which corresponds to the maximum possible (asymptotic) bottleneck accumulation of the L-MEM density in the hybridization region giving an infinite grow of $\mathscr{N}_q^{\mathrm{L}} \propto |q|^{8/3}$ for large negative o. For finite a this growth is suppressed. However, when the transfer of quasi-particles from the L-MEM to the U-MEM is small ($a \ll 1$), the L-MEM density accumulation is quite significant. For large $a \simeq 1$ (see the two lower lines in Fig. 3f for $a = 1$ and 0.5), there is practically no MEM accumulation. It is necessary to note that the increase in the population of the U-MEM in the course of the BEC formation must lead to the suppression of the bottleneck effect and to the consequent saturation of the MEM population peak. This effect is clearly visible in our previous observations [5].

Concluding, our model describes the formation of the experimentally observed peak in the MEM population and, thus, evidences that this accumulation appears due to the bottleneck effect in the transfer of magneto-elastic bosons from high to low frequencies through the hybridization region.

References

[1] C.W. Sandweg, M.B. Jungfleisch, V.I. Vasyuchka, A.A. Serga, P. Clausen, H. Schultheiss, B. Hillebrands, A. Kreisel, P. Kopietz, *Wide-range wavevector selectivity of magnon gases in Brillouin light scattering spectroscopy*, Rev. Sci. Instrum. **81**, 073902 (2010).
[2] A.G. Gurevich, G.A. Melkov, *Magnetization Oscillations and Waves* (CRC Press, New York, 1996).
[3] D.A. Bozhko, P. Clausen, A.V. Chumak, Yu.V. Kobljanskyj, B. Hillebrands, A.A. Serga, *Formation of Bose-Einstein magnon condensate via dipolar and exchange thermalization channels*, Low Temp. Phys. **41**, 1024 (2015).
[4] P. Clausen, D.A. Bozhko, V.I. Vasyuchka, B. Hillebrands, G.A. Melkov, A.A. Serga, *Stimulated thermalization of a parametrically driven magnon gas as a prerequisite for Bose-Einstein magnon condensation*, Phys. Rev. B **91**, 220402(R) (2015).
[5] A.A. Serga, P. Clausen, A.V. Chumak, B. Hillebrands, *Phonon mediated Bose-Einstein condensation of magnons*, Annual Report 2012: http://www.physik.uni-kl.de/fileadmin/hillebrands/Jahresberichte/Annual_report_2012/AR2012-Chapter4-2.pdf.

4.3   Parametric excitation of magnons in YIG films at low temperatures

L. Mihalceanu, V.I. Vasyuchka, D.A. Bozhko, T. Langner, A.A. Serga, and B. Hillebrands

Parametric pumping is one of the most efficient ways to excite magnons in a wide range of wavenumbers [1] and is a powerful tool for the investigation of fundamental properties of magnetization dynamics. Nowadays its importance is becoming even more evident since the efficient injection of magnons into the spin system of low damping yttrium-iron-garnet ($Y_3Fe_5O_{12}$, YIG) films allows for the observation of such prominent phenomena as magnon Bose-Einstein condensates (BECs) [2] and magnon supercurrents [3]. Up to date all experiments with magnon condensates and supercurrents have been performed at normal ambient conditions. At the same time, it is expected that the density of a magnon BEC can be significantly increased and the critical pumping power decreased at lower temperatures [4]. Moreover, since the magnon relaxation time increases with temperature decrease [5] the related prolongation of the BEC's lifetime will allow to investigate the BEC's dynamics at long-time intervals and will help to reveal such relatively slow effects as Josephson oscillations, etc. As the first step on the way to the investigation of the dynamics of magnon BECs at cryogenic temperatures we have studied the parametric excitation of magnons in the temperature range from 40 K to 340 K. To be able to directly correspond our findings with magnon BEC experiments we utilised parallel parametric pumping applied to an in-plane magnetized YIG film epitaxially grown in the (111) crystallographic plane on a gadolinium-gallium-garnet (GGG) substrate. Specifically, we address the impact of temperature on the saturation magnetization $4\pi M_s$, and further derive an estimate for the behavior of the magnon-relaxation parameter Γ_q on the low-temperature scale.

Figure 1a provides a sketch of the experimental setup. A microwave pump pulse of 10 μs duration is generated by a microwave source at a frequency of 13.76 GHz with 10 ms repetition time and is subsequently amplified. A rotary-vane attenuator allows for the precise regulation of the applied pumping power P_p up to 2.5 W. After passing a Y-circulator (Fig. 1a, port 1→ port 2) the pump pulse feeds a 50 μm-wide microstrip resonator inside a closed cycle refrigerator system. Here, a 6.7 μm thick YIG film having a ferromagnetic resonance (FMR) linewidth of 0.6 Oe at 3 GHz is placed on a resonator as it is shown in Fig. 1b. The reflected microwave signal is directed by the Y-circulator (Fig. 1a, port 2→port 3) to a semiconductor detector and an oscilloscope for rectification and observation.

The concept of parallel parametric pumping is based on the excitation of two magnons with a frequency ω_q and opposite wavevectors $\pm\mathbf{q}$ by the annihilation of a microwave photon with the frequency of $\omega_p = 2\omega_q$. The microstrip resonator induces an Oersted field $\mathbf{h}_p$, which is parallel to the bias magnetic field $\mathbf{H}$ (see Fig. 1b and is coupled to the longitudinal component of the
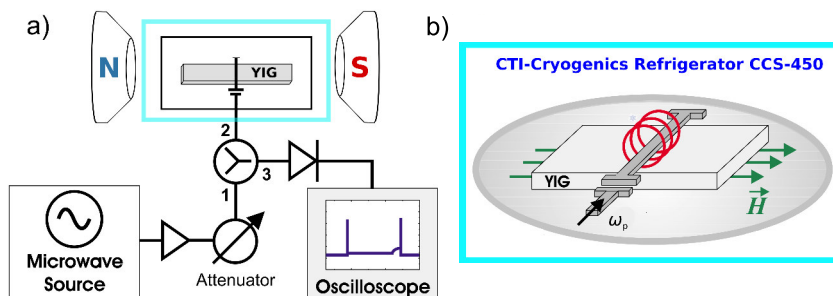
Fig. 1: a) Parametric pumping setup. b) Resonator on top of magnetic sample with applied magnetic fields. Adapted from [6]. The square surrounding the sample represents the implemented cryogenic station.
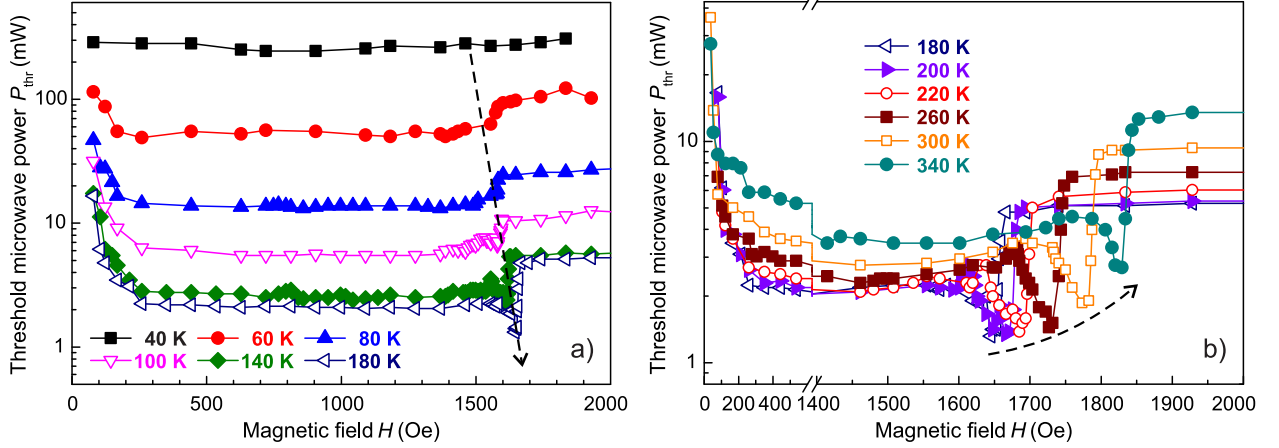
Fig. 2: Threshold curves $P_{thr}(H)$ measured at different temperatures in the temperature ranges: a) $40 - 180\,\mathrm{K}$ and b) $180 - 340\,\mathrm{K}$. The minima of the threshold curves at $H = H_c$ correspond to the excitation of dipolar magnons with wavenumbers $q \cong 0$ near the frequency of the ferromagnbetic resonance. Dipolar-exchange and exchange magnons are excited at $H < H_c$.

dynamic magnetization $\mathbf{M} \| \mathbf{H}$. When the threshold condition $h_p = h_{thr}$ is reached, the action of the microwave Oersted field completely compensates the spin-wave damping and gives rise to the parametric excitation process. The increasing absorption of the microwave energy in course of this process detunes the resonator and a kink, which indicates a threshold microwave power $P_p = P_{thr}$, appears at the end of the reflected signal (schematically shown on the oscilloscope in Fig. 1a.

By changing the bias field H the threshold power P_{thr} can be measured for different areas of the magnon spectrum. Figure 2 presents the dependencies $P_{thr}(H)$ recorded for a number of temperatures in the range from $40\,\mathrm{K}$ to $340\,\mathrm{K}$. At the critical field $H = H_c$ spin waves with $q \cong 0$ are excited near the frequency of the ferromagnetic resonance ω_{FMR}. In Fig. 2 this situation corresponds to the minima of the threshold curves $P_{thr}(H)$. The sharp jump up in the threshold power just above H_c is due to the transition from the parallel to the perpendicular parametric excitation regimes in the confined pumping geometry realized by the narrow microstrip resonator [6].

The dashed arrows in Fig. 2 indicate the shift of the critical point $P_{thr}(H_c)$ with temperature. In Fig. 2a a *decrease* of the threshold power with increasing temperature is shown in the range of $40\,\mathrm{K}$ to $180\,\mathrm{K}$. On the contrary, Fig. 2b shows an *increase* in the threshold power with further increasing temperature. At the same time, the experimentally determined critical field H_c monotonically increases with temperature along the whole temperature range. We use this dependence to calculate the effective saturation magnetization $4\pi M_s^{eff}$ by applying the Kittel formula:

$$\omega_p/2 = \omega_{FMR} = \gamma\sqrt{H_c(H_c + 4\pi M_s^{eff})}, \tag{1}$$

where γ is the gyromagnetic ratio. Here, $4\pi M_s^{eff}$ includes contributions of cubic and uniaxial anisotropies of the YIG film, which have been previously found to be smaller of $10\,\mathrm{Oe}$ over the temperature range in our experiments [7]. A small demagnetizing effect caused by a stray magnetic field induced by the paramagnetic GGG substrate is also expected at temperatures below $100\,\mathrm{K}$ [8]. Figure 3a shows the almost linear decrease of the effective saturation magnetization $4\pi M_s^{eff}$ with increasing temperature. The rate of $\Delta(4\pi M_s^{eff})/\Delta T = -3.05 \pm 0.08\,\mathrm{G/K}$ is in good agreement with previously reported results [9, 10].

The variation of the saturation magnetization directly affects the coupling between the microwave pumping field $\mathbf{h}_p$ and a longitudinal component of the precessing magnetization $\mathbf{M}$. As a result, the
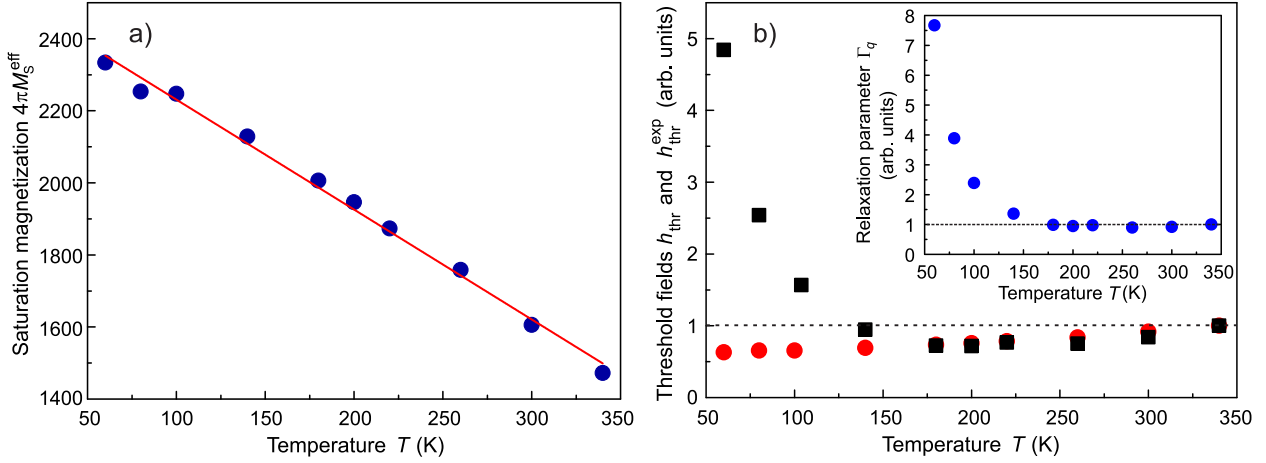
Fig. 3: a) Dependence of the effective saturation magnetization on the temperature. Line – the linear approximation of the experimental data. b) Temperature dependence of the threshold pumping field for magnons parametrically excited near the FMR frequency. Squares – the h_{thr}^{exp} values are determined using the measured threshold powers P_{thr}. Circles – the h_{thr} values are calculated using Eq. 2 for the experimentally determined values of $4\pi M_s^{eff}(T)$ in the assumption that $\Delta H_q = const$. The inset shows the calculated relaxation parameter Γ_q.

threshold field h_{thr}, which depends on both the spin-wave relaxation and the parametric coupling, is influenced by temperature. This influence can be estimated using the equation for the threshold field from Ref. [11]:

$$h_{thr} = \min\left\{\frac{\omega_p \Delta H_q}{\omega_M \sin^2 \theta_q}\right\}. \tag{2}$$

Here, $\omega_M = \gamma 4\pi M_s$, and θ_q is the angle between the magnon wavevector $\mathbf{q}$ and the magnetization direction. For the parametric excitation near and above the FMR frequency ($H \leq H_c$), we can assume $\theta_q \approx 90°$. ΔH_q is the width of a linear resonance curve of the parametrically excited spin-wave mode with the wavenumber q. It is defined as $\Delta H_q = 1/(\gamma T_q) = \Gamma_q/\gamma$, where T_q and Γ_q are the relaxation time and the relaxation parameter, respectively.

By assuming the value of ΔH_q in Eq. 2 to be constant over the entire temperature range and taking into account the experimentally determined values of $4\pi M_s^{eff}$ we have calculated the normalized temperature dependence of the threshold field, which is solely determined by the change in the parametric coupling strength. This dependence is shown by the circles in Fig. 3b.

The *experimental* threshold field h_{thr}^{exp}, which contains the information about the relaxation of parametrically excited magnons, can be found from the *measured* threshold powers using the relation $h_{thr}^{exp} = C\sqrt{P_{thr}}$. The parameter C depends on the pumping frequency ω_p, the geometry and the quality factor of the pumping resonator. As the resonance frequency and the quality factor of our microstrip resonator do almost not change with temperature we assume C to be a constant. The experimental values of the dimensionless threshold field normalized to the reference value at the temperature of 340 K are plotted in Fig. 3b (squares) for magnons excited near the FMR frequency ($H = H_c$). Its behavior is visibly non-monotonic: down to 180 K the threshold field h_{thr}^{exp} slightly decreases, while below 180 K it increases up to 5 times compared to the reference value. The comparison of the calculated ($h_{thr}(T)$, circles) and experimental ($h_{thr}^{exp}(T)$, squares) threshold dependencies clearly evidences that the high temperature part ($T \geq 180$ K) of the experimental dependency is mostly determined by the variation in the parametric coupling strength.

On the contrary, the strong increase of h_{thr}^{exp} in the low-temperature range ($T < 180$ K) is caused by

the spin-wave relaxation. The inset in Fig. 3b shows the dimensionless relaxation parameter Γ_q calculated with help of Eq. 2 using $h_{\text{thr}}(T)$ and $4\pi M_{\text{s}}^{\text{eff}}(T)$ derived from the experimental data. It becomes evident that for the temperature decrease from 180 K to 60 K the relaxation parameter Γ_q increases more than 7.5 times. This increase is considered to be untypical for pure YIG, for which a monotonic decrease of Γ_q is expected with decreasing temperature [5]. The observed relaxation behavior at low temperatures can be related either to the contribution of fast-relaxing rare-earth ions contaminating the chemical composition of YIG [12] or to the magnetic losses caused by the dipolar coupling of magnons with the spin-system of the paramagnetic GGG substrate [13]. Taking into account the quality of the used YIG film the latter cause seems to be the most probable.

In summary, in the temperature range from 40 K to 340 K we have investigated the relaxation of parametrically excited dipolar and exchange magnons in a YIG film epitaxially grown on a GGG substrate. We have found that the magnon lifetime strongly decreases at cryogenic temperatures. The observed relaxation behavior can be related to the magnetic damping caused by dipolar coupling of magnons to the paramagnetic spin system of the GGG substrate. These results show that low-temperature magnon BEC experiments must be performed in chemically-pure and substrate-free YIG samples.

References

[1] A.A. Serga, C.W. Sandweg, V.I. Vasyuchka, M.B. Jungfleisch, B. Hillebrands, A. Kreisel, P. Kopietz, M.P. Kostylev, *Brillouin light scattering spectroscopy of parametrically excited dipole-exchange magnons*, Phys. Rev. B **86**, 134403 (2012).

[2] S.O. Demokritov, V.E. Demidov, O. Dzyapko, G.A. Melkov, A.A. Serga, B. Hillebrands, A.N. Slavin, *Bose-Einstein condensation of quasi-equilibrium magnons at room temperature under pumping*, Nature **443**, 430 (2006).

[3] D.A. Bozhko, A.A. Serga, P. Clausen, V.I. Vasyuchka, F. Heussner, G.A. Melkov, A. Pomyalov, V.S. L'vov, B. Hillebrands, *Supercurrent in a room-temperature Bose-Einstein magnon condensate*, Nature Phys. **12**, 1057 (2016).

[4] A.I. Bugrij, V.M. Loktev, *On the theory of Bose-Einstein condensation of quasiparticles: on the possibility of condensation of ferromagnons at high temperatures*, Low Temp. Phys. **33**, 51 (2007).

[5] R.C. LeCraw, E.G. Spencer, *Intrinsic relaxation of uniform precession in ferromagnetic resonance of yttrium iron garnet*, J. Phys. Soc. Jpn. **17**, 401 (1962).

[6] T. Neumann, A.A. Serga, V.I. Vasyuchka, B. Hillebrands, *Field-induced transition from parallel to perpendicular parametric pumping for a microstrip transducer*, Appl. Phys. Lett. **94**, 192502 (2009).

[7] M. Kaack, S. Jun, S.A. Nikitov, J. Pelzl, *Magnetostatic spin wave modes excitation in yttrium-iron-garnet film under various temperatures*, J. Magn. Magn. Mater. **204**, 90 (1999).

[8] V.V. Danilov, D.L. Lyfar', Y.V. Lyubon'ko, A.Yu. Nechiporuk, S.M. Ryabchenko, *Low-temperature ferromagnetic resonance in epitaxial garnet films on paramagnetic substrates*, Soviet Physics Journal **32**, 276 (1989).

[9] T. Langner, A. Kirihara, A.A. Serga, B. Hillebrands, V.I. Vasyuchka, *Damping of parametrically excited magnons in the presence of the longitudinal spin Seebeck effect*, arXiv: 1607.07274 (2016).

[10] B. Obry, V.I. Vasyuchka, A.V. Chumak, A.A. Serga, B. Hillebrands, *Spin-wave propagation and transformation in a thermal gradient*, Appl. Phys. Lett. **101**, 192406 (2012).

[11] A.G. Gurevich, G.A. Melkov, *Magnetization oscillations and waves*, CRC New York (1994).

[12] G.F. Dionne, G.L. Fitch *Temperature dependence of spin-lattice relaxation in rare-earth iron garnets*, J. Appl. Phys. **87**, 4963 (2000).

[13] M.G. Balinskii, V.V. Danilov, A.Yu. Nechiporuk, V.M. Talalaevskii, *Damping of magnetostatic spinwaves in substrates*, Radiofizika **29**, 1253 (1986).

B. Insulator Magnon Spintronics

The field of science that refers to information transport and processing by spin waves is known as magnonics. This name relates to the magnon – the spin-wave quantum associated with the flip of a single spin. The usage of magnonic approaches in the field of spintronics, hitherto dealing with electron-carried spin currents, gave birth to the field of magnon spintronics [Nat. Phys. **11**, 453 (2015)]. This field is currently emerging, and considers magnon-based data buses, data processing elements operating with analogous and digital information, as well as converters between the magnon subsystem and the electron-carried spin and charge currents. In this context, a magnetic insulator such as yttrium iron garnet (YIG) is of particular interest for magnon spintronics due to its extremely small damping parameter that ensures transport of spin information over macroscopic distances up to centimeters. Moreover, a magnetic insulator provides Joule-heat-free transfer and processing of spin information.

The first Report (Report 4.4) is devoted to the experimental studies of the temporal evolution of pulsed Spin Hall Effect - Spin Transfer Torque (SHE-STT) driven auto-oscillations in a YIG/Pt microdisc using time-resolved BLS measurements. The focus lies on the temporal evolution of the spin dynamics in the microstructure as soon as the anti-damping STT overcompensates the intrinsic Gilbert damping in the system. It was demonstrated that the intensity, frequency, and the temporal evolution of the SHE-STT-excited magnetization precession behave differently in different regions of the investigated microstructure. Furthermore, the BLS intensity is found to saturate on a time scale of 25 ns or longer, dependent on the current density. For this reason, our findings suggest that a proper ratio between the voltage and the pulse duration is of crucial importance for the potential STT-based devices.

A majority gate is of especial interest for spin-wave based data processing since it can perform majority logic operations as well as AND, OR, NAND, and NOR operations. In Report 4.5 we present the experimental realization and investigation of a macroscopic spin-wave majority gate, which on the microscopic scale has already been investigated numerically in our group (see Annual Reports 2014 and 2015). A majority gate features three inputs and one output and was fabricated from micron-thick YIG. The input logic signals were defined by the phases of 0 or π of the applied microwave signals. The operation of the device as a majority gate was proven using microwave techniques - the output phase of the signal was defined by the majority of the input phases. Additional time-resolved measurements have shown that the majority gate can switch logic output within approximately 11 ns.

Finally, in Report 4.6 we use micromagnetic simulations to study a spin-wave directional coupler in the form of two dipolarly-coupled spin-wave waveguides separated by a gap. A spin wave excited in one waveguide transfers all its energy into the second waveguide after the propagation of a certain distance. This distance is defined by the strength of the coupling between the waveguides and can be tuned by a variety of parameters. In particular, the waveguides magnetized in parallel or anti-parallel configurations have different coupling strengths what opens access to the reconfigurability of the device functionality. Our studies show that the directional coupler can be used as a crossing for magnonic conduits as well as a power and frequency splitter for microwave signal processing.

B.   Isolator-Magnon-Spintronik

Die Magnonik umfasst das Fachgebiet, das sich mit der Informationsübertragung und -verarbeitung mittels Spinwellen befasst. Die Bezeichnung bezieht sich auf das Magnon, das Quant einer Spinwelle, welches einem einzelnen Spin-Flip entspricht. Die Verwendung magnonischer Konzepte in der Spintronik, welche sich bis dahin nur ladungsgebundener Spinströme bediente, brachte das Fachgebiet der Magnon-Spintronik hervor [Nat. Phys. **11**, 453 (2015)]. Dieses Forschungsfeld befindet sich momentan im großen Wachstum und befasst sich mit magnon-basierter Datenübertragung und Komponenten zur Verarbeitung von analogen und digitalen Informationen, sowie mit Umwandlern an den Schnittstellen zwischen dem magnonischen Untersystem und den elektronenbasierten Spin- und Ladungsströmen. In diesem Zusammenhang ist ein magnetischer Isolator wie das Yttrium-Eisen-Granat (YIG) besonders interessant, da dieses Material aufgrund seiner äußerst geringen Spinnwellen-Dämpfung den Transport von Spin-Informationen über makroskopische Entfernungen bis in den Zentimeterbereich ermöglicht. Zudem erlaubt ein magnetischer Isolator die Übertragung und Verarbeitung von Spin-Informationen ohne Beeinträchtigung durch Joulsche Erwärmung.

Bericht 4.4 beschäftigt sich mit der experimentellen Untersuchung der Zeitentwicklung von Auto-Oszillationen in YIG|Pt-Mikroscheiben, welche gepulst durch ein Spintransfer-Drehmoment getrieben werden. Dieses Spintransfer-Drehmoment wird durch einen Spinstrom verursacht, welcher in der Platinschicht aufgrund des Spin-Hall-Effekts erzeugt wird. Die Messungen wurden hierbei mithilfe der zeitaufgelösten BLS-Spektroskopie durchgeführt. Dabei liegt das Hauptaugenmerk auf der Zeitentwicklung der Spindynamik in den Mikrostrukturen für den Fall, dass das der Gilbertdämpfung entgegenwirkende Spintransfer-Dreh-moment selbige kompensiert. Es wurde gezeigt, dass die Intensität, die Frequenz und die Zeitentwicklung der angeregten Präzession der Magnetisierung innerhalb der Mikrostruktur lokal variieren. Zudem wurde festgestellt, dass die ermittelte BLS-Intensität abhängig von der Stromdichte auf einer Zeitskala von 25 ns oder mehr sättigt. Diese Ergebnisse weisen auf die enorme Bedeutung eines geeigneten Verhältnisses zwischen Spannung und Pulsdauer für die Umsetzung von Anwendungen hin.

Ein Majoritätsgatter ist von besonderem Interesse für die spinwellenbasierte Datenverarbeitung, da damit sowohl die logische Majoritätsoperation, als auch die Operationen AND, OR, NAND oder NOR implementiert werden können. Wir stellen im Bericht 4.5 die experimentelle Realisierung und Untersuchung eines makroskopischen Spinwellen-Majoritätsgatters vor, welches auf mikroskopischer Ebene in unserer Gruppe bereits numerisch untersucht wurde (s. Jahresberichte 2014 und 2015). Das Majoritätsgatter besitzt drei Eingänge und einen Ausgang und wurde aus einem YIG-Film mit einer Dicke im Mikrometerbereich hergestellt. Die logischen Zustände der Eingangssignale wurden über eine Phase von 0 oder π der entsprechenden Mikrowellensignale definiert. Auch die Untersuchung des Gatters erfolgte mithilfe von Mikrowellentechnik - die Phase des Ausgangssignals wird definiert durch die Majorität der Eingangsphasen. Zusätzliche zeitaufgelöste Messungen zeigen, dass das Umschalten des logischen Ausgangszustandes innerhalb von etwa 11 ns stattfindet.

Abschließend werden in Bericht 4.6 die Ergebnisse mikromagnetischer Simulationen zur Untersuchung eines Spinwellen-Richtkopplers in der Form zweier dipolar gekoppelter und räumlich separierter Spinwellen-Wellenleiter vorgestellt. Eine in einem der Wellenleiter angeregte Spinwelle transferiert nach einer gewissen Distanz in den benachbarten Wellenleiter. Diese Distanz ist durch die Stärke der Kopplung bestimmt und kann durch eine Vielzahl von Parametern eingestellt werden. Im Speziellen besitzen parallel oder antiparallel zueinander magnetisierte Wellenleiter

unterschiedliche Kopplungsstärken, womit die Möglichkeit einer rekonfigurierbaren Funktionalität eröffnet wird. Unsere Untersuchungen zeigen die mögliche Verwendung des Richtkopplers als Knoten in magnonischen Schaltkreisen oder als Leistungs- und Frequenzweiche in der mikrowellenbasierten Signalverarbeitung.

4.4   Temporal evolution of auto-oscillations in a YIG/Pt microdisc driven by spin-transfer torque induced by the spin Hall effect

V. Lauer, M. Schneider, T. Meyer, T. Brächer*, P. Pirro, B. Heinz, B. Lägel, B. Hillebrands, and A.V. Chumak

In collaboration with M.C. Onbasli and C.A. Ross, Department of Materials Science and Engineering, Massachusetts Institute of Technology, Cambridge, Massachusetts 02139, USA

*Current affiliation: Univ. Grenoble Alpes, CNRS, CEA, INAC-SPINTEC, 17, rue des Martyrs 38054, Grenoble, France

Magnetization auto-oscillations in magnetic microstructures driven by spin-transfer torque (STT) [1], which is induced by the spin Hall effect (SHE) [2] in an adjacent heavy metal layer, attracted attention in the last few years [3]. First successful experiments were performed on patterned all-metallic bilayers of NiFe/Pt [4] and, later, also on bilayers of the ferrimagnetic insulator yttrium iron garnet (YIG) and Pt [5, 6]. YIG is known for its very low Gilbert damping and thus is important for fundamental research in magnonics and for potential future application. Up to now, experiments have been typically performed by applying continuous direct currents to the Pt layer in such a way that the generated spin current exerts an anti-damping STT on the magnetization in the magnetic layer. To the best of our knowledge, only in the experiments of Ref. [7] the temporal behavior of SHE-STT-driven spin dynamics have been investigated so far, where a time resolution of 20 ns has been achieved. However, pulsed excitation of the magnetization precession using a pulse duration of a few nanoseconds or shorter is more realistic to the working regime of future spintronic devices. Therefore, further time-resolved investigations of the onset of auto-oscillations, which provide insight into the processes of SHE-STT-driven spin dynamics, are of great interest.
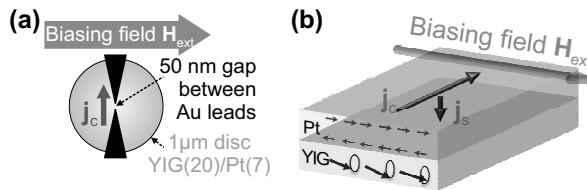
Fig. 1: a) Sketch of the investigated YIG/Pt disc with tapered Au leads on top. The charge current is applied perpendicular to the biasing field. b) Configuration of the biasing field, the applied charge and the SHE-STT-generated spin current densities ($\mathbf{j}_c$ and $\mathbf{j}_s$) for the exertion of anti-damping STT on the magnetization in the YIG layer.

This Report addresses the experimental investigation of pulsed SHE-STT-driven auto-oscillations in a YIG/Pt microdisc by using time-resolved BLS measurements. The focus lies on the temporal evolution of the spin dynamics in the microstructure as soon as the anti-damping STT [8] overcompensates the intrinsic Gilbert damping in the system. The probed YIG/Pt microdisc has a diameter of 1 μm, and the layer thicknesses of YIG and Pt are $d_{YIG} = 20$ nm and $d_{Pt} = 7$ nm, respectively. In order to fabricate the microstructures, a YIG film was grown by pulsed laser deposition on a gadolinium gallium garnet substrate [9]. Subsequently, a Pt film was deposited on top by means of sputter deposition. Microwave-based ferromagnetic resonance measurements yielded a Gilbert damping parameter of $\alpha_{YIG} = 1.2 \times 10^{-3}$ for the YIG film before the Pt deposition, and an increased damping value of $\alpha_{YIG/Pt} = 5.7 \times 10^{-3}$ for the YIG/Pt bilayer. The subsequent struc-

turing of the microdiscs was achieved by electron-beam lithography and argon-ion milling [10]. Eventually, tapered Au leads on top of the microdisc with a spacing of 50 nm (see Fig. 1a) were patterned by using electron-beam lithography and vapor deposition to allow for the application of high current densities.

Time-resolved BLS measurements are performed by using a probing laser with a wavelength of 491 nm and a power of 2 mW, focused down to a laser-spot diameter of approximately 400 nm on the structure under investigation. In the experiment, 75 ns long dc voltage pulses with a repetition rate of 500 ns are applied to the Au leads that results in a corresponding charge current flowing in the Pt layer of the microdisc. An external biasing field of $\mu_0 H_{ext} = 110$ mT magnetizes the microdisc perpendicular to the current flow direction. An exemplary configuration of the biasing field $\mathbf{H}_{ext}$ relative to the charge current density $\mathbf{j}_c$, and the SHE-STT-generated spin current density $\mathbf{j}_s$ are depicted in Fig. 1b for the case of a resulting anti-damping STT on the magnetization in the YIG layer. It should be mentioned that a threshold-like onset of auto-oscillations for a certain field polarity is observed above a critical voltage value of $V_{crit} = (0.7 \pm 0.1)$ V only for the current direction which is expected to generate an anti-damping STT according to the theory of the SHE. Such a behavior is consistent with other experimental findings as, e.g., in Refs. [4–6]. These observations moreover prove that, unlike in Report 4.13, the auto-oscillations cannot originate from the spin Seebeck effect (SSE) due to a thermal gradient, since the SSE is known to excite magnetization precession for both current orientations. As discussed in Report 4.13, the Au leads on top of the Pt layer are assumed to prevent the formation of sufficiently large thermal gradients required for triggering of auto-oscillations due to the SSE.
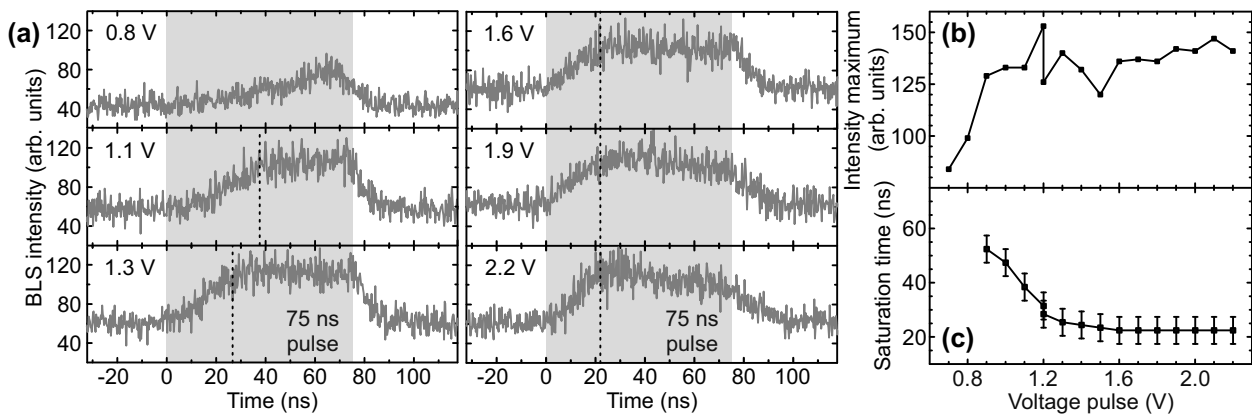
Fig. 2: a) Frequency-integrated BLS intensity detected in the center of the microdisc as a function of time for different applied dc voltage pulses above the threshold. The pulse duration of 75 ns is depicted by the grayish areas. b) The maximum BLS intensity reached during the pulse as a function of the applied voltage. c) The saturation time of the BLS intensity within the pulse duration before reaching saturation.

Figure 2a shows the temporal evolution of excited auto-oscillations (represented by the BLS intensity) detected in the center of the microdisc for different applied voltages above the critical voltage. Spin dynamics are apparently excited during the pulse duration of 75 ns illustrated by the grayish areas in the graphs. We find that for voltages higher than 1 V the BLS intensity saturates within the pulse duration. Nonlinear magnon scattering processes could be responsible to limit further increase. It is noteworthy that the BLS intensity maximum saturates also as a function of the applied voltage (see Fig. 2b). Furthermore, the saturation time values (as indicated by the dashed lines in Fig. 2a) are plotted in Fig. 2c. This saturation time drops with the applied voltage and saturates at

a value of approximately 23 ns at high voltages.

Our findings, moreover, suggest that there is an optimization potential for the signal output of pulsed auto-oscillations regarding energy consumption, by choosing an ideal ratio between operating voltage and pulse duration (compare Fig. 2b and Fig. 2c). In the structure under investigation, the pulse duration must not fall below 23 ns and the optimal operating voltage is at approximately 1.3 V, that corresponds to a current density of 2.1×10^{12} A/m^2 in the center of the disc. The importance of the appropriate voltage value in particular is emphasized by the temporal behavior observed at rather low and rather high voltages. For applied voltages below 1 V, but still above the threshold, such as, e.g., for 0.8 V shown in the upper left graph of Fig. 2a, the pulse duration is too short to reach saturation. On the other hand, for high voltages of, e.g. 2.2 V, as shown in the lower right graph of Fig. 2a, the BLS signal slowly drops within the pulse duration after reaching its maximum after 23 ns. This intensity decrease over time within the pulse duration is assumed to result from a decrease in the spin-mixing conductance due to the increase in the total temperature in the microdisc [11], which consequently leads to a reduced injection of the SHE-generated spin current, and to a reduction of the anti-damping STT. These crucial features need to be considered for potential spintronics applications based on pulsed SHE-STT-driven nano-oscillators.
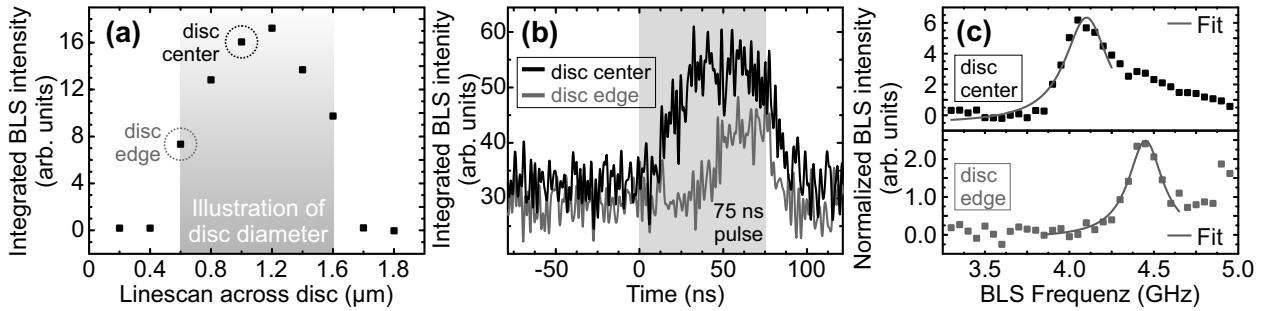
Fig. 3: a) Linescan perpendicular to the current flow direction showing the time- and frequency-integrated BLS intensity. b) Frequency-integrated BLS intensity as a function of time in the center and at the edge of the disc, respectively. c) Time-integrated BLS intensity during the pulse as a function of the BLS frequency, normalized to the BLS intensity when the pulse is switched off. The solid lines are Lorentzian fits.

A linescan at an applied voltage of 1.3 V is performed across the disc in the direction perpendicular to the current flow in order to investigate the spatial distribution of SHE-STT-driven spin dynamics. The BLS intensity integrated during the pulse over all investigated BLS frequencies is plotted in Fig. 3a as a function of the position along the disc. It shows a maximum in the disc center, and moderate intensities at the disc edges. This observation can be understood in terms of the inhomogeneous current distribution in structures such as the one investigated here [4] and, additionally, due to the finite size of the laser spot which is partially outside the microstructure when the disc edge is probed. In order to discuss the differences in the spin dynamics driven during the pulse in the disc center compared to the disc edge, Fig. 3b shows the frequency-integrated BLS intensity as a functions of time, and Fig. 3c shows the time-integrated BLS intensity as a functions of the BLS frequency. As it can be seen in Fig. 3b, the BLS intensity at the disc edge saturates at a lower level, and shows a much longer saturation time. The lower intensity level is attributed to the finite spot size of the laser as mentioned before. However, the longer saturation time cannot be explained by the spot size, but in terms of the current distribution in the microdisc. As already discussed, the saturation time depends on the applied voltage, viz. it depends on the current density. According to Fig. 2c, the saturation time extracted from measurements in the disc center does not reach its

saturation value of 23 ns for voltages below 1.3 V, which is the value used for the linescan data in Figs. 3a-c. Due to the decreased current density at the disc edge, the corresponding saturation time is expected to be in a regime below saturation, and thus, is expected to be longer then in the disc center. This is in agreement with the experimental findings in Fig. 3b. Furthermore, the BLS frequency in the disc center is lower compared to the edge, as can be seen in Fig. 3c, which we believe is a consequence of the inhomogeneous current distribution. A decrease in the BLS frequency with an increase of the current has been observed in various comparable experiments in Refs. [4, 6, 7].

In summary, we used time-resolved BLS measurements to investigate the onset of pulsed SHE-STT-driven magnetization auto-oscillations in a YIG/Pt microdisc. The BLS intensity is found to saturate on a time scale of 23 ns or longer, dependent on the particular current density which originates from the applied voltage and the position on the microdisc. Furthermore, both the maximum intensity and the saturation time saturate with increasing operating voltage. For this reason, our findings suggest that a proper ratio between the voltage and the pulse duration is of crucial importance for the power consumption of potential devices based on pulsed auto-oscillations. It was demonstrated that the intensity, frequency and the temporal evolution of the SHE-STT-excited magnetization precession behave differently in different regions of the investigated microstructure.

References

[1] J.C. Slonczewski, *Current-driven excitation of magnetic multilayers*, J. Magn. Magn. Mater. **159**, L1-L7 (1996).

[2] J.E. Hirsch, *Spin Hall effect*, Phys. Rev. Lett. **83**, 1834 (1999).

[3] A.V. Chumak, V.I. Vasyuchka, A.A. Serga, B. Hillebrands, *Magnon spintronics*, Nature Phys. **11**, 453 (2015).

[4] V.E. Demidov, S. Urazhdin, H. Ulrichs, V. Tiberkevich, A. Slavin, D. Baither, G. Schmitz, S.O. Demokritov, *Magnetic nano-oscillator driven by pure spin current*, Nature Mater. **11**, 1028-1031 (2012).

[5] M. Collet, X. de Milly, O. d'Allivy Kelly, V.V. Naletov, R. Bernard, P. Bortolotti, J. Ben Youssef, V.E. Demidov, S.O. Demokritov, J.L. Prieto, M. Muñoz, V. Cros, A. Anane, G. de Loubens, O. Klein, *Generation of coherent spin-wave modes in yttrium iron garnet microdiscs by spin-orbit torque*, Nat. Commun. **7**, 10377 (2016).

[6] V.E. Demidov, M. Evelt, V. Bessonov, S.O. Demokritov, J.L. Prieto, M. Muñoz, J. Ben Youssef, V.V. Naletov, G. de Loubens, O. Klein, M. Collet, P. Bortolotti, V. Cros, A. Anane, *Direct observation of dynamic modes excited in a magnetic insulator by pure spin current*, Sci. Rep. **6**, 32781 (2016).

[7] V.E. Demidov, S. Urazhdin, E.R.J. Edwards, M.D. Stiles, R.D. McMichael, S.O. Demokritov, *Control of magnetic fluctuations by spin current*, Phys. Rev. Lett. **107**, 107204 (2011).

[8] V. Lauer, D.A. Bozhko, T. Brächer, P. Pirro, V.I. Vasyuchka, A.A. Serga, M.B. Jungfleisch, M. Agrawal, Yu.V. Kobljanskyj, G.A. Melkov, C. Dubs, B. Hillebrands, A.V. Chumak, *Spin-transfer torque based damping control of parametrically excited spin waves in a magnetic insulator*, Appl. Phys. Lett. **108**, 012402 (2016).

[9] M.C. Onbasli, A. Kehlberger, D.H. Kim, G. Jakob, M. Kläui, A.V. Chumak, B. Hillebrands, C.A. Ross, *Pulsed laser deposition of epitaxial yttrium iron garnet films with low Gilbert damping and bulk-like magnetization*, APL Mater. **2**, 106102 (2014).

[10] P. Pirro, T. Brächer, A.V. Chumak, B. Lägel, C. Dubs, O. Surzhenko, P. Görnert, B. Leven, B. Hillebrands, *Spin-wave excitation and propagation in microstructured waveguides of yttrium iron garnet/Pt bilayers*, Appl. Phys. Lett. **104**, 012402 (2014).

[11] K. Uchida, T. Kikkawa, A. Miura, J. Shiomi, E. Saitoh, *Quantitative temperature dependence of longitudinal spin Seebeck effect at high temperatures*, Phys. Rev. X **4**, 041023 (2014)

AG MAGNETISMUS
TU KAISERSLAUTERN

4.5   A macro-scaled YIG Majority Gate

T. Fischer*, M. Kewenig, D.A. Bozhko*, A.A. Serga, B. Hillebrands, and A.V. Chumak
*Graduate School Materials Science in Mainz, Staudingerweg 9, 55128 Mainz, Germany

*In collaboration with I.I. Syvorotka, Department of Crystal Physics and Technology,
Scientific Research Company Carat, Lviv, Ukraine*

Over the last decades, CMOS-based devices have seen permanent technological progress resulting in steadily increasing speed and capabilities in computational technology [1]. However, with miniaturization of circuitry [2], handling the increasing power density in processing units becomes more challenging and, thus, requires for future technologies favorably making use of transport mechanisms other than electric currents. Under these aspects, the concept of magnonics [3–6] and spin wave-based logic [7, 8] provides a promising draft to compete with challenges related to future information processing. This technology allows for wave-based computing and data processing rates in the region of characteristic spin-wave frequencies, which can be extended to the upper GHz region. Small logic elements can be realized by accessing the exchange region of the spin-wave spectrum featuring wavelengths in the nanometer range [9]. The highly versatile dispersion relation depending on material parameters as well as magnetization and field configuration [6] makes spin waves useful in a wide range of devices [10, 11]. By allowing for new logics concepts based on the interference of waves, a significant reduction of the number of logic elements compared to the number of transistors in CMOS-based concepts is possible [12].

We present here the experimental realization and investigation of a macroscopic spin-wave majority gate, which on the microscopic scale has already been investigated numerically in our group [13]. In general, a majority gate features three inputs and one output [14]. For the majority operation, the output state represents the majority of the input states, which is illustrated in Table 1. In our experiments, the information is encoded in the phase of the spin waves and, without loss of generality, we use a phase of $\phi^{(0)} = 0$ for a logic '0' and $\phi^{(1)} = \pi$ for a logic '1'.

Input phases			Logic input state	Output
i1	i2	i3		
0	0	0	000	0
0	0	π	001	0
0	π	0	010	0
π	0	0	100	0
π	0	π	101	1
π	π	0	110	1
0	π	π	011	1
π	π	π	111	1

Table 1: Truth table of the majority operation. In the case of a spin-wave majority gate, the logic state is encoded in the phase of the waves.

A photograph of the device investigated in this work is shown in Fig. 1b. The magnetic structure has been fabricated from a LPE-YIG (Yttrium Iron Garnet, $Y_3Fe_5O_{12}$) film with a thick-
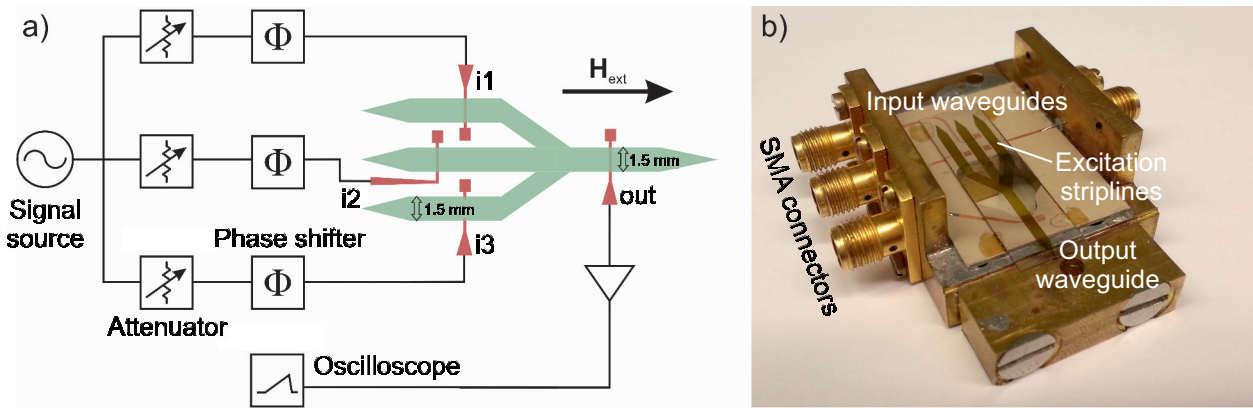
Fig. 1: (a) Sketch of the microwave setup used in the experiments, (b) photograph of the device under test. The input signals are conditioned with respect to phase and amplitude. When passing the copper striplines (red), the RF signals excite spin waves in the respective waveguide and the output signal is probed with a separate stripline and measured employing a fast oscilloscope.

ness of $5.4\,\mu m$ on a Gallium Gadolinium Garnet substrate by means of photolithography and wet-chemical etching. Before the patterning process, the linewidth of the ferromagnetic resonance of the full film has been determined to $\mu_0\Delta H_0 = 0.062\,mT$. All spin-wave waveguides feature a width of $w_g = 1.5\,mm$ and spin waves can be excited inductively by RF currents sent through copper striplines featuring a width of $w_a = 75\,\mu m$. The magnetic structure is depicted in Fig. 1a together with the microwave setup employed for signal conditioning and the excitation of spin waves. The input RF current is provided by a single microwave generator and split into three input signals. A phase shifter in each channel allows for encoding the logic information into the phase of the spin waves. Attenuators are used to level out the different transmission characteristics of the equipment and the different spin-wave excitation efficiencies of the respective input striplines. The propagation of waves through the bended waveguides into the combiner and the output waveguide is expected to feature comparably larger losses. However, it has been shown that propagation of spin waves through bended structures is possible [15]. Propagating through the output waveguide, the spin waves will evoke a signal in a copper stripline which can be mapped directly by using a fast oscilloscope.
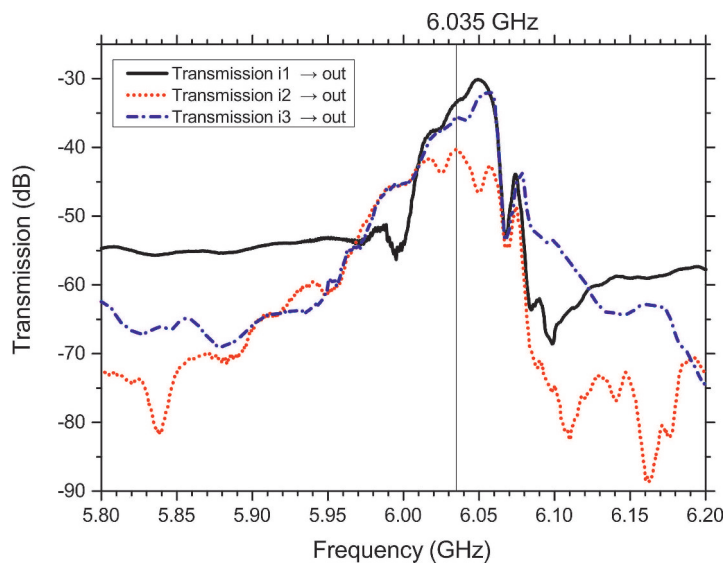
Fig. 2: Transmission spectra of the respective input channels towards the output channel. The characteristic BVMSW behavior is clearly visible. The attenuation differs due to varying excitation efficiency, electromagnetic coupling, and different properties of the microwave components.

AG MAGNETISMUS
TU KAISERSLAUTERN

Operation of the device is performed in the regime of Backward Volume Magnetostatic Spin Waves (BVMSW) [6] with the external field applied parallel to the waveguides. However, we have also tested the device in the configuration of Magnetostatic Surface Spin Waves. Although the transmission spectra differ, the operational characteristics appear to be qualitatively the same. In order to determine a suitable working point for an efficient operation of the device, spin-wave transmission through each of the channels towards the output is measured with a Vector Network Analyzer. The input power is kept at a level of $-3\,\mathrm{dBm}$ to avoid the occurence of nonlinear effects. Figure 2 shows the recorded transmission spectra. With an externally applied field of $\mu_0 H_\mathrm{ext} = 142.9\,\mathrm{mT}$, for all three spectra the BVMSW transmission characteristic is visible with the FMR frequency lying at about $f_\mathrm{FMR} \approx 6.06\,\mathrm{GHz}$. Variations of the attenuation mainly depend on the anisotropic character of spin waves in in-plane magnetized films: The transmission through the combiner requires a modification of the wavenumber in the bends. However, a certain part of energy is expected to be reflected.

We subsequently choose an operational spin-wave carrier frequency of $f_\mathrm{c} = 6.035\,\mathrm{GHz}$. Nevertheless, our studies have shown that the choice of the working point is not critical and the majority gate can be operated in a wide range of frequencies. Besides equality of the signal amplitudes in each channel, the desired phases of 0 and π for each signal have to be defined consistently with the phases of the remaining channels. Therefore, a signal whose phase is defined as 0 is directly provided to the input i2 serving as the reference channel. Applying a signal with equal amplitude to one of the remaining channels and continuously adjusting its phase, the amplitude of the output signal exhibits maxima and minima which allows for assigning phase shifts of 0 and π to the input signal. We employ a fast oscilloscope with a sampling rate of $40\,\mathrm{GSa/s}$ allowing for a direct mapping of the signal evoked in the stripline by the output spin wave. In our experiments, all possible logic states have been applied to the input of the device and the corresponding output signals are presented in Fig. 3. Since the phase of the signal serves as the carrier of information, this quantity is most important to the output signal. For the case of a logic input state '100' (full downward triangles) and '011' (hollow squares), respectively, Fig. 3 reveals
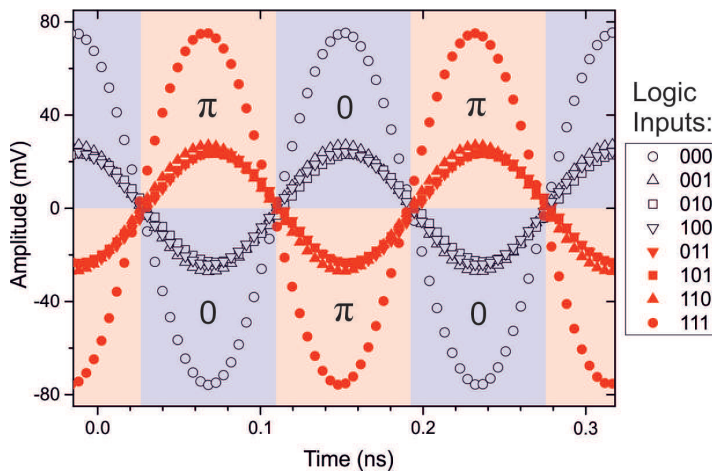
Fig. 3: Measured time traces of the output signals corresponding to the respective input logic states. The experimental setup is depicted in Fig. 1a. The dependence of the output phase on the majority of the input phases is clearly visible.

that with shifting all input signals by π, the phase of the output signal phase accordingly shifts by π. Assigning a logic '0' and '1' to the respective output phases, a reliable operation of the device is possible with the phase of the output signal representing the majority of the phase of the input signals. However, these measurements also resemble a major drawback of the characteristics of the majority gate which is the dependence of the output amplitude on the input state: In the case of

an input state of '111', the output signal amplitude at the oscilloscope is $U_a \approx 75\,\mathrm{mV}$ whereas for the input state '110' it only amounts to $U_a \approx 25\,\mathrm{mV}$. Nevertheless, this challenge will only become relevant for the construction of integrated magnon circuits and might, for instance, be solved by employing nonlinear effects in the output waveguide.

All in all, we succeeded in the experimental realization of a majority gate logic device based on the interference of spin waves. However, further improvement is needed on the route towards the implementation of spin-wave logic circuits. A promising concept could be a phase control by electric fields as described in the work by Ustinov *et al.* [16] or by spin-polarized currents. Progress in the production of ultra-thin YIG films with low Gilbert damping constant as well as the possible use of alternative materials such as Heusler compounds [17] might facile the realization of a spin-wave majority gate on the microscale.

References

[1]   R.W. Keyes, *The Impact of Moore's Law*, IEEE SSCS Newsletter (2006).

[2]   C. Wagner, N. Harned, *EUV lithography: Lithography gets extreme*, Nature Photonics **4**, 24 (2010).

[3]   A.V. Chumak, V.I. Vasyuchka, A.A. Serga, B. Hillebrands, *Magnon spintronics*, Nature Physics **11**, 6 (2015).

[4]   A. Khitun, K.L. Wang, *Nano scale computational architectures with Spin Wave Bus*, Superlattices and Microstructures **38**, 184 (2005).

[5]   V.V. Kruglyak, S.O. Demokritov, D. Grundler, *Magnonics*, Journal of Physics D: Applied Physics **43**, 264001 (2010).

[6]   A.A. Serga, A.V. Chumak, B. Hillebrands, *YIG magnonics*, Journal of Physics D: Applied Physics **43**, 264002 (2010).

[7]   T. Schneider, A.A. Serga, B. Leven, B. Hillebrands, R.L. Stamps, M.P. Kostylev, *Realization of spin-wave logic gates*, Applied Physics Letters **92**, 022505 (2008).

[8]   K. Ganzhorn, S. Klingler, T. Wimmer, S. Geprägs, R. Gross, H. Huebl, S.T.B. Goennenwein, *Magnon based logic in a multi-terminal YIG/Pt nanostructure*, arXiv1604.07262v1 (2016).

[9]   C.W. Sandweg, Y. Kajiwara, A.V. Chumak, A.A. Serga, V.I. Vasyuchka, M.B. Jungfleisch, E. Saitoh, B. Hillebrands, *Spin pumping by parametrically excited exchange magnons*, Physical Review Letters **106**, 216601 (2011).

[10]   A.V. Chumak, A.A. Serga, B. Hillebrands, *Magnon transistor for all-magnon data processing*, Nature Communications **5**, 4700 (2014).

[11]   A.A. Nikitin, A.B. Ustinov, A.A. Semenov, A.V. Chumak, A.A. Serga, V.I. Vasyuchka, E. Lähderanta, B.A. Kalinikos, B. Hillebrands, *A spin-wave logic gate based on a width-modulated dynamic magnonic crystal*, Applied Physics Letters **106**, 102405 (2015).

[12]   A. Khitun, *Multi-frequency magnonic logic circuits for parallel data processing*, Journal of Applied Physics **111**, 054307 (2012).

[13]   S. Klingler, P. Pirro, T. Brächer, B. Leven, B. Hillebrands, A.V. Chumak, *Design of a spin-wave majority gate employing mode selection*, Applied Physics Letters **105**, 152410 (2014).

[14]   A. Khitun, M. Bao, K.L. Wang, *Magnonic logic circuits*, Journal of Physics D: Applied Physics **43**, 264005 (2010).

[15]   P. Clausen, K. Vogt, H. Schultheiss, S. Schäfer, B. Obry, P, Pirro, B. Leven, B. Hillebrands, *Mode conversion by symmetry breaking of propagating spin waves*, Applied Physics Letters **99**, 162505 (2011).

[16]   A.B. Ustinov, B.A. Kalinikos, G. Srivivasan, *Nonlinear microwave phase shifter on electromagnetic-spin waves*, Technical Physics **59**, 1406 (2014).

[17]   T. Kubota, S. Tsunegi, M. Oogane, S. Mizukami, T. Miyazaki, H. Naganuma, Y. Ando, *Half-metallicity and Gilbert damping constant in $Co_2Fe_xMn_{1-x}Si$ Heusler alloys depending on the film composition*, Applied Physics Letters **94**, 122504 (2009).

AG MAGNETISMUS
TU KAISERSLAUTERN

4.6   Spin-wave directional coupler

Q. Wang, P. Pirro, B. Hillebrands, and A.V. Chumak

In collaboration with Roman Verba, Institute of Magnetism, National Academy of Sciences of Ukraine, Kyiv 03142, Ukraine and Andrei Slavin, Department of Physics, Oakland University, Rochester, MI 48309, USA

The research field of magnonics attracts growing attention due to its potential applications in spintronics devices in which spin waves carry information instead of electrons [1, 2]. Several novel concepts of spin-wave logic devices have been proposed recently [3, 4]. However, although data transfer and processing have been successfully demonstrated in independent devices, the connection of different spin-wave elements in a magnon circuit is still a bottleneck. Crossing structures, in which two independent magnon conduits cross each other without interaction, are a prerequisite for the realization of complex integrated two-dimensional spin-wave circuits [5, 6]. A simple X-type crossing [6] does not satisfy the requirements at the nanometer scale because the crossing part of the structure acts as a spin-wave re-emitter into all four spin-wave channels.

In this Report, we use micromagnetic simulations to study a spin-wave directional coupler in the form of two dipolarly-coupled spin-wave waveguides separated by a gap. This scenario is reminiscent to coupling between two optical waveguides with narrow spacing in integrated optics [7]. A spin wave excited in one waveguide transfers all its energy into the second waveguide after the propagation of a certain distance. This distance is defined by the strength of the coupling between the waveguides and can be tuned by a variety of parameters.
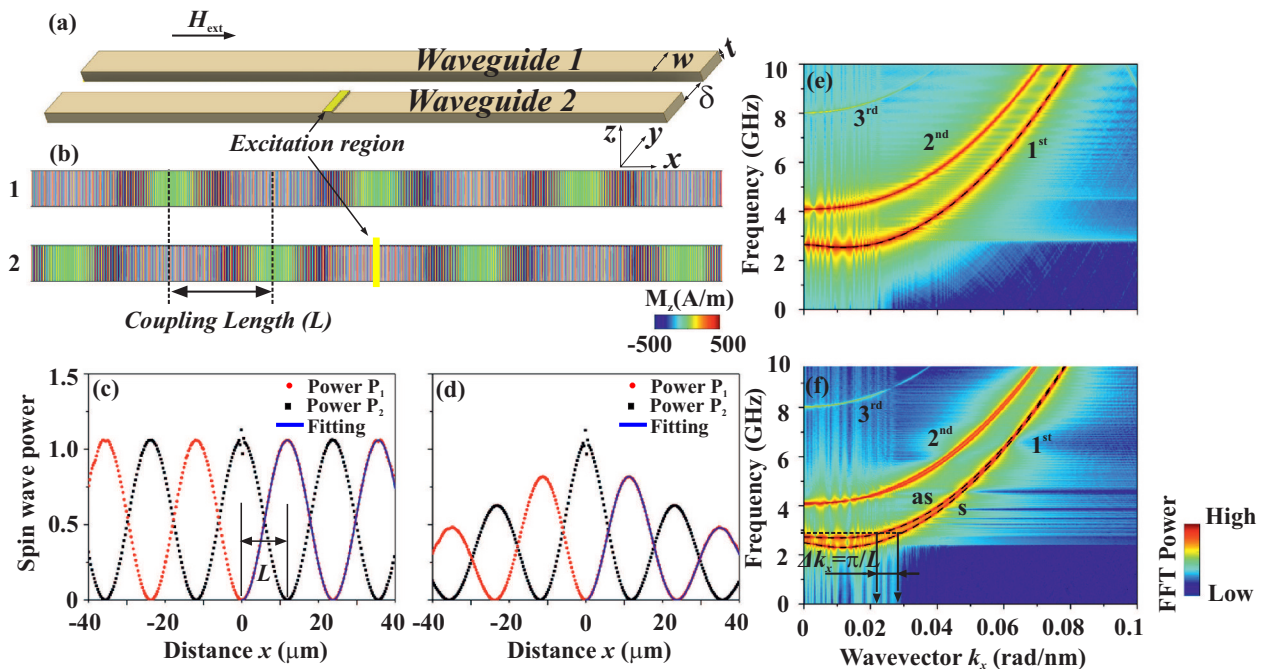
Fig. 1: A schematic view of the dipolarly-coupled spin-wave waveguides (a) and a snapshot of the spin-wave amplitudes in them (b). The variation of the spin-wave power in both waveguides as a function of distance x for the case of zero damping (c) and for the real damping parameter α (d). Dispersion characteristics for the case of the isolated single spin-wave waveguide (e) and for the same waveguide but coupled to a second one (f).

In particular, the waveguides magnetised in parallel or anti-parallel configurations have different coupling strengths what opens access to the reconfigurability of the device functionality. Our studies show that the directional coupler can be used as a crossing for magnonic conduits as well as a power and frequency splitter for microwave signal processing.
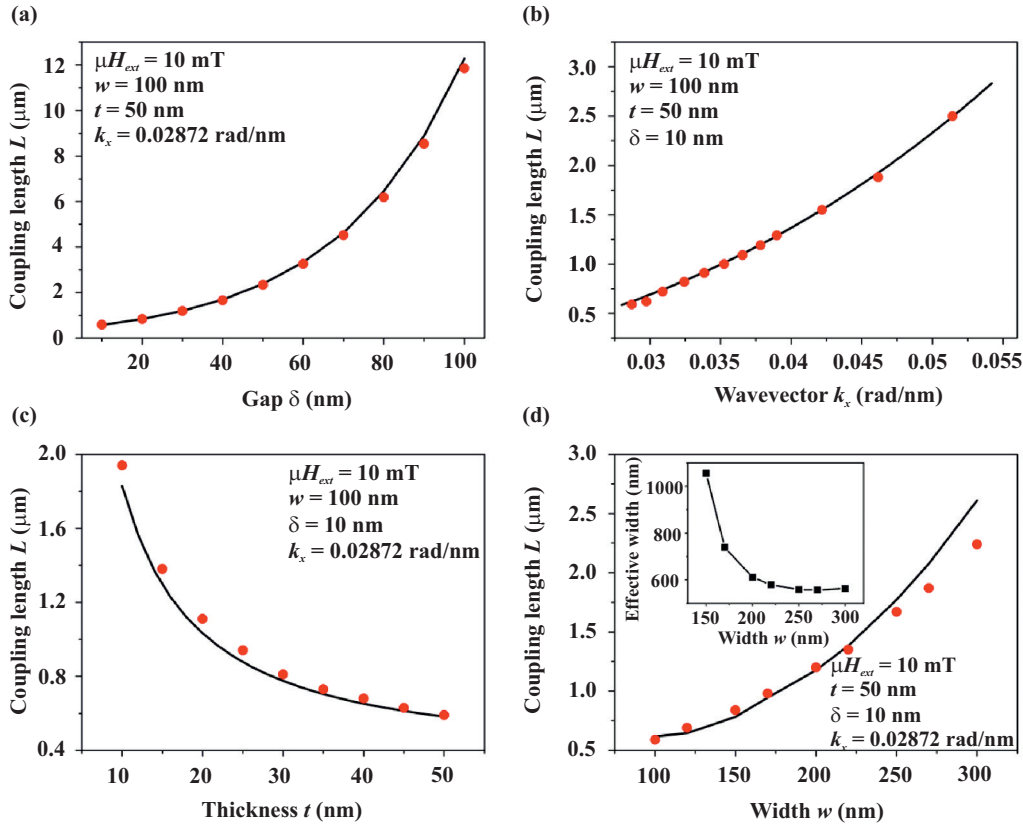
Fig. 2: Coupling length L as a function of (a) the distance between the waveguides δ, (b) the wavevector k_x, (c) the thickness t, and (d) the width w, obtained by means of numerical simulations (symbols) and analytics (lines). The inset in panel (d) shows the dependence of the effective width of the waveguide on the real width w (the line is a guide to the eyes).

The structure under investigation is schematically shown in Fig. 1a. Two parallel waveguides of $100\,\mu\mathrm{m}$ length, of width w in the range from 100 to 300 nm, and of thickness t in the range from 10 to 50 nm are placed with a gap δ in between from 10 to 100 nm. The simulations are performed for the parameters of a Yttrium Iron Garnet (YIG) nanometer-thick film [8]: saturation magnetization $M_s = 1.4 \times 10^5\,\mathrm{A/m}$, exchange constant $A = 3.5\,\mathrm{pJ/m}$, Gilbert damping $\alpha = 2 \times 10^{-4}$. The Gilbert damping α at the ends of the waveguides exponentially increases to 0.5 in order to prevent spin-wave reflection. The simulation is performed using Mumax3 [9]. The cell size is $10 \times 10 \times t\,nm^3$ (t is the thickness). A small external magnetic field $\mu_0 H_{\mathrm{ext}} = 10\,\mathrm{mT}$ is applied along the waveguides (in x direction). In order to excite spin waves, a sinc field pulse $h_{\mathrm{ac}} = h_0 \mathrm{sinc}(2\pi f_c t)$ is applied in the center of the waveguide 2 within an 20 nm wide area (see the area shown in Fig. 1a), with $\mu_0 h_0 = 1\,\mathrm{mT}$ and a cutoff frequency of $f_c = 20\,\mathrm{GHz}$.

Figure 1b shows the snapshot of the amplitude of the spin wave in the coupled waveguides of width $w = 100\,\mathrm{nm}$, gap $\delta = 100\,\mathrm{nm}$, and thickness $t = 50\,\mathrm{nm}$. The frequency of the spin wave in this case is 2.96 GHz. That corresponding to a wavevector $k_x = 0.02872\,\mathrm{rad/nm}$. One can see, that after the spin wave is excited in waveguide 2, its energy is transferred completely to the waveguide 1

AG MAGNET/SMUS
TU KA/SERSLAUTERN
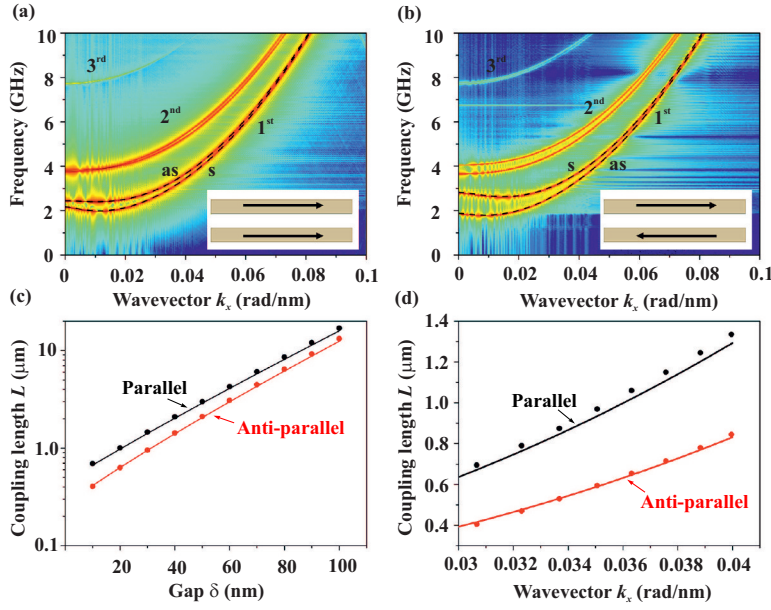
Fig. 3: The dispersion characteristics of a spin-wave waveguide coupled to a second one for the parallel (a) and anti-parallel (b) magnetisation configurations. The widths of the waveguides are 100 nm, thickness is 50 nm, gap is 10 nm. Coupling length as a function of gap (c) and wavevector (d) for parallel and anti-parallel configurations. The circle points and lines are calculated by micromagnetic simulation and analytic theory, respectively.

after the propagation of a certain distance. We refer to this distance as to the coupling length L - see Fig. 1b. Figure 1c and Fig. 1d show the variations of the spin-wave intensities in the coupled waveguides as a function of distance x for the case of zero damping and for the case of a nonzero damping parameter, respectively. The coupling length $L = 11.85\,\mu\text{m}$ can be easily extracted from Fig. 1c and Fig. 1d. The simulations performed for the damping-free waveguides clearly show that the spin-wave energy oscillates between the waveguides without any losses. The line is a fit to the data using $P_1 = P_i \sin^2(\pi x/(2L))$, where P_i is the power launched into the waveguide 2 and P_1 is the power in the waveguide 1. For the case of real spin-wave damping, the spin-wave intensity gradually decreases as expected. The results can be fitted by a similar model including the damping term $P_1 = P_i \sin^2(\pi x/(2L))\exp(-|2x|/x_{\text{freepath}})$, where $x_{\text{freepath}} = 88\,\mu\text{m}$ is the exponential decay length.

Figure 2 shows the dependence of the coupling length L on the gap size δ – Fig. 2a, the spin-wave wavevector k – Fig. 2b, the waveguides thickness t – Fig. 2c and the width w – Fig. 2d. The calculation parameters are shown in the panels. In general, one can clearly see that the increase in the dipolar coupling between the waveguides results in a decrease of L. The coupling can be increased by a decrease in the gap δ between the waveguides, by an increase in their thickness t, by a decrease in their widths w, and finally by a decrease in the spin-wave wavenumber k_x. The results obtained by micromagnetic simulations (circle points) and analytic theory (lines, not discussed in this Report) are practically consistent. The effective widths due to the spin pinning at the edges of the waveguides were calculated by simulations and used for the analytic calculations. The inset in Fig. 2d shows the dependence of the effective width on the geometrical width w of the waveguides. The effective width strongly increases with the decrease in w due to the transfer from pinned to unpinned states at the edges of the waveguides [10].

Next, we present the dependence of the coupling lengths L on the magnetization orientation of the waveguides. In order to build the anti-parallel configuration, the external field is removed. Panel a and b of Fig. 3 show the dispersion characteristics obtained by micromagnetic simulation (color map) and analytic theory (dash lines) for the parallel configuration, when both waveguides are magnetised in the same direction, and for the anti-parallel configuration. The dispersions for

the anti-parallel configuration have a pronounced difference compared to the parallel case. The mode splitting due to the dipolar interaction is larger for the anti-parallel case. That means that the waveguides are stronger coupled in such a configuration. The same conclusion is supported by the dependences of the coupling length L on the gap δ and on the spin-wave wavevector k shown in Figure 3c and Figure 3d, respectively. The coupling length for the anti-parallel configuration is always smaller than that of the parallel one.

The directional coupler based on the coupled spin-wave waveguides can have different functionalities depending on the ratio between the coupling length L and the length of the coupled waveguides l_{eff}. Thus, if $l_{\text{eff}} = (2n + 1)L$, where n is an integer value, the whole energy will be transferred from one waveguide to the other and the directional coupler can be used as a crossing of magnonic conduits. If $l_{\text{eff}} = (n + 1/2)L$ the coupler can be used as a $3\,\text{dB}$ microwave power splitter. Taking into account that L strongly depends on the spin-wave wavenumber k and, consequently, on the signal frequency, the directional coupler can be used as a frequency splitter. Finally, the change in the magnetization direction of one of the waveguides allows for the switching of such reconfigurable directional coupler functionality for fixed l_{eff} and signal frequency. Taking into account nano-meter sizes of the studied device, it represents an interesting approach for processing of both digital and analogue information.

References

[1] Y. Kajiwara, K. Harii, S. Takahashi, J. Ohe, K. Uchida, M. Mizuguchi, H. Umezawa, H. Kawai, K. Ando, K. Takanashi, S. Maekawa, E. Saitoh, *Transmission of electrical signals by spin-wave interconversion in a magnetic insulator*, Nature **464**, 262 (2010).

[2] A.V. Chumak, V.I. Vasyuchka, A.A. Serga, B. Hillebrands, *Magnon spintronics*, Nat. Phys. **11**, 453 (2015).

[3] S. Klingler, P. Pirro, T. Brächer, B. Leven, B. Hillebrands, A.V. Chumak, *Design of a spin-wave majority gate employing mode selection* Appl. Phys. Lett. **105**, 152410 (2014).

[4] M.P. Kostylev, A.A. Serga, T. Schneider, B. Leven, B. Hillebrands, *Spin-wave logical gates*, Appl. Phys. Lett. **87**, 153501 (2005).

[5] K.S. Lee, S.K. Kim, *Conceptual design of spin wave logic gates based on a Mach-Zehnder type spin wave interferometer for universal logic functions*, J. Appl. Phys. **104**, 053909 (2008).

[6] S. Klingler, P. Pirro, T. Brächer, B. Leven, B. Hillebrands, A.V. Chumak, *Spin-wave logic devices based on isotropic forward volume magnetostatic waves*, Appl. Phys. Lett. **106**, 212406 (2015).

[7] A.V. Krasavin, , A.V. Zayats, *Active Nanophotonic Circuitry Based on Dielectric-loaded Plasmonic Waveguides*, Advanced Optical Materials, **3**, 1662 (2015).

[8] P. Pirro, T. Brächer, A.V. Chumak, B. Lägel, C. Dubs, O. Surzhenko, P. Gornert, B. Leven, B. Hillebrands, *Spin-wave excitation and propagation in microstructured waveguides of yttrium iron garnet/Pt bilayers*, Appl. Phys. Lett. **104**, 012402 (2014).

[9] A. Vansteenkiste, J. Leliaert, M. Dvornik, M. Helsen, F. Garcia-Sanchez, B. Van Waeyenberge, *The design and verification of MuMax3*, AIP Adv. **4**, 107133 (2014).

[10] K.Y. Guslienko, A.N. Slavin, *Boundary conditions for magnetization in magnetic nanoelements*, Phys. Rev. B **72**, 014463 (2005).

C.   Metallic Magnon Spintronics

The combination of standard spintronics with spin-wave dynamics led to the emergence of the field of *magnon spintronics*. *Magnon spintronics* aims for the magnon to charge current conversion and for magnon-based data processing devices. A magnon, i.e. the quantum of a spin wave, carries an angular momentum or spin as well and can be used for storage, processing and transport of spin information, building on its outstanding properties such as long lifetime and potential for dissipationless transport. Furthermore, the utilization of spin Hall effects to create and detect spin currents and magnetization dynamics has push *magnon spintronics* even further. In this section we focus on spin Hall related effects like spin-pumping (SP) and inverse spin Hall effect (ISHE) by addressing systems like CoFeB/Ta-Pt bilayers, Fe/Pt, Py/Pt and YIG/Pt bilayers. In addition, we present new designs and understanding of novel spin-wave devices that push the field of magnon spintronics even further.

Report 4.8 refers to the conversion of a magnon current into a charge current via the spin pumping effect in CoFeB sample series by using different capping layers such as Pt and Ta. The spin pumping is strong and efficient in Ta, while we were not able to quantify it in Pt, due to the lack of correlation between effective spin mixing conductance g_{eff} and the detected ISHE voltage. Angular resolved spin pumping measurements have further shown that spin rectification in CoFeB systems are dominated by the anomalous Hall effect while the anisotropic magnetoresistance plays a minor role.

Report 4.7 presents an overview of the factors that influence the spin current generation in magnetic/-non-magnetic bilayers. We show the in-plane angular dependencies of the SP/ISHE and spin rectification effects such as anisotropic magentoresistance (AMR) and anomalous Hall effect (AHE), of bilayers composed of different FM, such as Fe, Py, and YIG, and capping layers with significant spin Hall angle, such as Pt and Ta, and small spin Hall angle, such as Al and MgO. Spin rectification effects do scale differently in Fe, Py and YIG bilayer systems. AMR is more pronounced than AHE in RF magnetron sputtered Py, while AHE seems to be almost equal in magnitude for epitaxial Fe systems. Pronounced AHE is occurring in nanometer thin films YIG/Pt samples. In Py/Al and Py/Pt there exists a non negligible out-of-plane excited AMR, that does not directly correlate with the microwave induced currents. Epitaxial Fe/MgO shows pronounced features at angles, where the magnetization traverses the magnetic hard axis of Fe.

Report 4.10 presents work for the realisation of prototype devices in the field of magnon spintronics. The development of a nano-scale reconfigurable magnonic crystal (MC) as universal magnonics component suitable for versatile operations with data, was achieved by using electric field-induced perpendicular magnetic anisotropy (PMA). The voltage-controlled PMA induces a spatial variation of the internal field along the waveguide resulting in pronounced band gaps in the spin-wave spectra. The reconfigurable magnonic crystal can be dynamically controlled by applying a voltage to different metallic gates. The report opens the path to low loss, low power voltage-controlled reconfigurable magnonic crystals that can be used in future nano-sized magnon spintronics devices.

Report 4.11 presents a design for a dynamically switchable spin wave signal splitter as pivotal element for magnon-based networks. The basic concept of the studied structure is to create spin waves caustics and to control them by an inhomogeneous external field. We demonstrate the ability of the local manipulation of the spin waves caustic direction by an inhomogeneous magnetization distribution and its dynamic controllability by locally applied magnetic fields. Based on these results, the concept of a switchable spin wave signal splitter is developed: channeling spin waves

into different output waveguides or blocking them depending on the applied DC-current.

Report 4.9 focuses on the spin-wave band structure and the resulting density of states (DOS) for the design and understanding of novel spin-wave devices. The interplay of dipolar and exchange energies in thin magnetic films leads to a rich variety in the dispersion relations of different spin wave modes. Here, we compare μBLS spectra obtained from NiFe films of different thicknesses with the calculated spin-wave DOS. A simple model is able to explain the characteristics of the experiment qualitatively but a more accurate description will need to include the magnon-photon scattering processes in more detail.

C.   Metallische Magnon-Spintronik

Die Kombination von Standard-Spintronik und Spinwellendynamik führte zur Entstehung des Feldes der Magnon-Spintronik. Dieses Forschungsgebiet hat die Konversion zwischen Magnonen- und Ladungsträgerströmen und die Entwicklung Magnonen-basierter Datenverarbeitungsbauteilen zum Ziel. Ein Magnon, d.h. das Quant einer Spinwelle, trägt einen Drehimpuls oder Spin und kann zur Speicherung, Prozessierung und zum Transport einer Spin-Information Verwendung finden, basierend auf seinen hervorstechenden Eigenschaften wie großer Lebensdauer und potenziell ver- lustfreiem Transport. Weiterhin wurde die Magnon-Spintronik durch die Ausnutzung des Spin- Hall-Effekts zur Erzeugung und Detektion von Spinströmen und Magnetisierungsdynamik vor- angetrieben. In diesem Abschnitt konzentrieren wir uns auf die Spin-Hall-zugehörigen Effekte wie Spinpumpen (SP) und inversen Spin-Hall-Effekt (ISHE), wobei Systeme wie CoFeB/Ta-Pt-, Fe/Pt-, Py/Pt- und YIG/Pt-Doppelschichten behandelt werden. Zusätzlich präsentieren wir Ent- würfe und das Verständnis neuartiger Spinwellenbauteile, die das Feld der Magnon-Spintronik noch weiter vorantreiben.

Bericht 4.8 bezieht sich auf die Umwandlung eines Magnonenstroms in einen Ladungsstrom durch Spinpumpen in einer Reihe von CoFeB-Proben unter Verwendung verschiedener Deckschichten wie Pt und Ta. Spinpumpen findet in Ta stark und effizient statt, während es aufgrund einer fehlenden Korrelation zwischen der effektiven Spinmischungsleitfähigkeit g_{eff}, und der detek- tierten ISHE-Spannung nicht gelang, den Effekt in Pt zu quantifizieren. Winkelaufgelöste Mes- sungen des Spinpumpens haben weiterhin gezeigt, dass Spingleichrichtung in CoFeB-Systemen vom anomalen Hall-Effekt dominiert wird, der anisotrope magnetoresistive Effekt jedoch eine un- tergeordnete Rolle spielt.

Bericht 4.7 präsentiert einen Überblick über die Faktoren, die die Erzeugung von Spinströmen in magnetischen/nichtmagnetischen Doppelschichten beeinflussen. Wir zeigen die Winkelabhängig- keiten von SP/ISHE und von Spingleichrichtungseffekten wie dem anisotropen magnetoresistiven Effekt (AMR) und dem anomalen Hall-Effekt (AHE) in der Ebene von Doppelschichten, die aus verschiedenen magnetischen Materialien wie Fe, Py, und YIG mit Deckschichten aus Ma- terialien mit signifikantem Spin-Hall-Winkel wie Pt und Ta bzw. mit kleinem Spin-Hall-Winkel wie Al und MgO aufgebaut sind. Die Spingleichrichtungseffekte skalieren unterschiedlich in Fe-, Py- und YIG-Doppelschichtsystemen. AMR überwiegt AHE in RF-magnetrongesputtertem Py, während AHE in epitaktischen Fe-Systemen fast den gleichen Beitrag zu leisten scheint. Ein aus- geprägter AHE tritt ebenfalls in Nanometer-dünnen YIG/Pt-Schichten auf. In Py/Al und Py/Pt existiert eine nicht vernachlässigbare AMR-Anregung aus der Ebene heraus, die nicht direkt mit den mikrowelleninduzierten Strömen korreliert. Epitaktisches Fe/MgO zeigt ausgeprägte Merk- male bei Winkeln, bei denen die Magnetisierung die magnetisch schwere Achse der Fe-Schicht durchläuft.

Bericht 4.10 zeigt eine Richtung für die Realisierung von Bauteilprototypen im Feld der Magnon-Spintronik auf. Die Entwicklung eines rekonfigurierbaren magnonischen Kristalls (MC) im Nanometerbereich als universelles magnonisches Bauteil für vielseitige Anwendungen in Verbindung mit Daten wurde mit Hilfe einer durch ein elektrisches Feld induzierten senkrechten magnetischen Anisotropie (PMA) erreicht. Die spannungsgesteuerte PMA induziert eine räumliche Variation des internen Feldes entlang des Wellenleiters, was eine Ausprägung der Bandlücken im Spinwellenspektrum zur Folge hat. Der rekonfigurierbare magnonische Kristall kann dynamisch kontrolliert werden, indem eine Spannung an verschiedenen metallischen Gattern angelegt wird. Der Bericht eröffnet den Weg zu verlustarmen, spannungskontrollierten, rekonfigurierbaren magnonischen Kristallen mit geringer Leistungsanforderung, die in zukünftigen magnon-spintronischen Bauteilen im Nanobereich genutzt werden können.

Bericht 4.11 bietet einen Entwurf für einen dynamisch schaltbaren Spinwellensignalteiler als zentrales Element für magnonenbasierte Netzwerke. Das grundlegende Konzept der untersuchten Struktur ist die Erzeugung von Spinwellenkaustiken und deren Kontrolle durch ein inhomogenes externes Feld. Wir demonstrieren die Fähigkeit zur lokalen Beeinflussung der Richtung der Spinwellenkaustiken durch eine inhomogene Magnetisierungsverteilung und die dynamische Kontrollierbarkeit durch lokal angelegte magnetische Felder. Basierend auf diesen Ergebnissen wird das Konzept eines schaltbaren Spinwellensignalteilers entwickelt: Spinwellen werden abhängig vom angelegten Gleichstrom in unterschiedliche Ausgangswellenleiter gelenkt oder blockiert.

Bericht 4.9 fokussiert sich auf die Spinwellen-Bandstruktur und die resultierende Zustandsdichte (DOS) für den Entwurf und das Verständnis neuartiger Spinwellen-Geräten. Das Zusammenspiel von dipolaren Energien und Austauschenergien in dünnen magnetischen Schichten führt zu einer großen Vielfalt von Dispersionsrelationen verschiedener Spinwellenmoden. Hier vergleichen wir von unterschiedlich dicken NiFe-Schichten erhaltene μBLS-Spektren mit der berechneten Spinwellen-Zustandsdichte. Ein einfaches Modell ist in der Lage, Charakteristiken des Experiments qualitativ zu erklären, aber eine genauere Beschreibung wird Magnonen-Photonen-Streuung detaillierter einbeziehen müssen.

4.7   Angular dependencies of spin pumping and rectification effects

S. Keller, J. Greser, M.R. Schweizer, B. Hillebrands, and E.Th. Papaioannou

In spintronics bilayers composed of a ferromagnetic (FM) and a nonmagnetic (NM) layer with large spin-orbit-interaction, at ferromagnetic resonance (FMR) the spin pumping (SP) and the inverse spin Hall effects (ISHE) allow for the generation of a spin current and its conversion into a charge current, respectively. A wide range of ferromagnets [1], such as metallic, semiconducting and insulators, and NM [2] materials, e.g. Au, Pd, Ta, W, and Pt, have been investigated to this point [3]. In metallic FM layers overlapping additional effects take place, such as the so called spin rectification (SR) effect, which impede the access to the pure ISHE signal. Different approaches for separation have been thoroughly investigated. Thickness variation of the FM and the NM layers show different dependencies onto ISHE and SR, but requires a lot of effort for producing whole sample series or wedged microstructures. Another method is a sweep of the excitation frequency, which cannot be applied to all experimental setups and requires a careful analysis of the microwave properties of the setup. Also the minimization of the electrical microwave field at the location of the sample by using a microwave cavity is possible, but in most cases only certain frequencies can be applied. The rotation of the magnetization angle by rotating the external magnetic field in- and out-of-plane is one of the most common and practicable methods, while out-of-plane rotation normally requires higher magnetic fields for thin films [3, 4].

In this article, we present our studies on in-plane angular dependencies of the SP/ISHE and SR effects, such as anisotropic magnetoresistance (AMR) and anomalous Hall effect (AHE), of bilayers composed of different FM materials, such as Fe, Py, and YIG, and capping layers with significant spin Hall angle Θ_{SH}, such as Pt, and small Θ_{SH}, such as Al and MgO, excited by a microwave stripline antenna. For a fixed excitation frequency and external field angle, the external field amplitude is to match the resonance condition. The measured voltage peaks is then fitted by the following equation:

$$V_{meas} = V_{sym}\frac{(\Delta H)^2}{(H-H_{FMR})^2+(\Delta H)^2} + V_{asym}\frac{-2\Delta H(H-H_{FMR})}{(H-H_{FMR})^2+(\Delta H)^2} \quad , \tag{1}$$

where V_{sym} is the amplitude of the symmetric part, V_{asym} is the amplitude of the antisymmetric part, ΔH is the linewidth, H is the applied external magnetic field, and H_{FMR} is the corresponding FMR field value. While the SP/ISHE effect contributes only to V_{sym}, the SR effects contribute to both voltage amplitudes. The relative contributions of AHE and AMR to V_{sym} and V_{asym} are determined by the phase difference between the dynamic magnetization $\mathbf{m}(t)$ and the microwave induced AC current $\mathbf{j}(t)$ inside the FM layer. This phase difference is not easily accessible [2]. To understand the shape of the measured voltage amplitudes one needs to calculate the angular dependencies of SP/ISHE and SR (a detailed derivation can be seen in [3, 4]). Let us consider the coordinate system (see at Fig. 1a), where x' and z' are the in-plane and y the out-of-plane lab fixed coordinates, Θ_H is the angle between the external magnetic field $\mathbf{H}$ and the z' axis. The electrical contacts are either in x' or z' direction and $I_{x'}$ and $I_{z'}$ are the microwave induced currents. The dynamic magnetic microwave fields $h_{x'}$, $h_{z'}$ (in-plane) and h_y (out-of-plane) are determined by the microwave excitation. In our case, seen in Fig. 1b, where the contacts are in x' direction, the microwave stripline antenna is along the z' direction and the samples are macroscopic. One
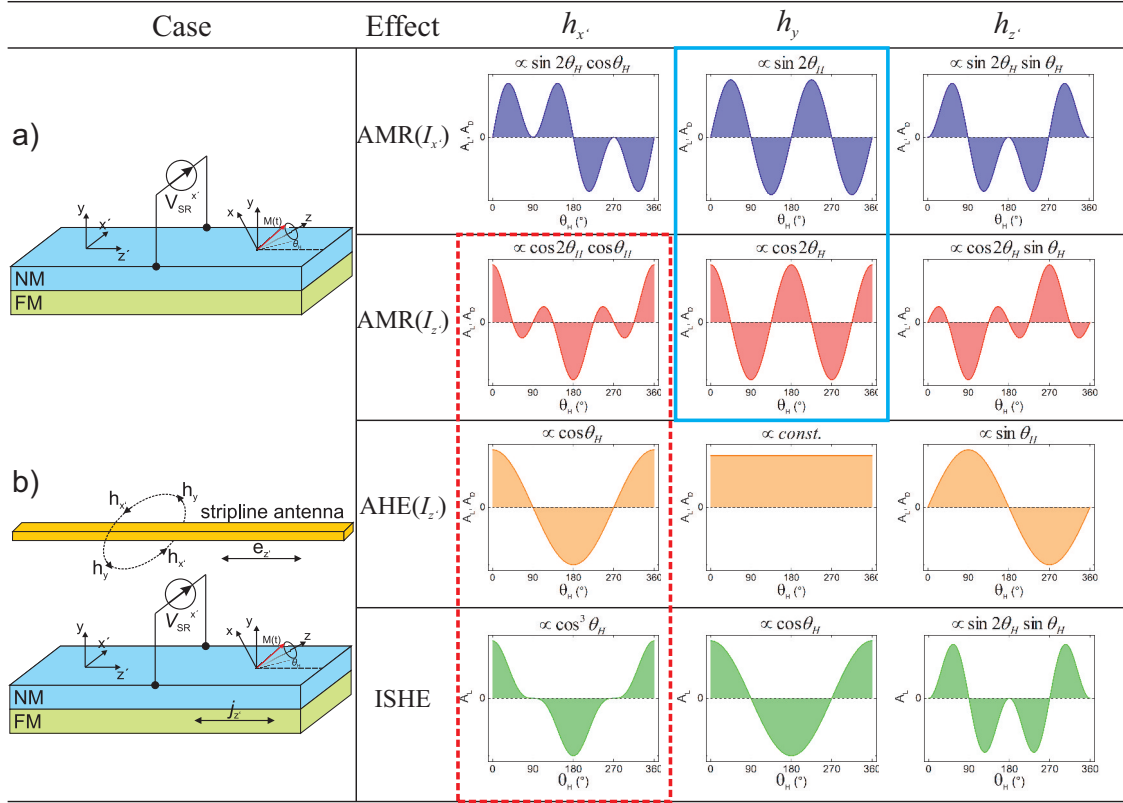
Fig. 1: Left: a) General case of experiments, b) Case of our experiments. Right: Theoretical in-plane magnetization angular dependencies of Spin Rectification effects and ISHE with transverse contacts and different dynamic external magnetic field geometries [4]. Graphs in red (dashed) box show main effects and in blue (solid) box show side effects of our experiments.

needs to consider primarily $I_{z'}$ and $h_{x'}$ (in-plane dynamic magnetic fields), and h_y (out-of-plane dynamic magnetic fields) which is approximately a magnitude smaller than the in-plane fields. Here, the signal obtained from AHE ($\propto \cos(\Theta_H)$) is similar to ISHE ($\propto \cos^3(\Theta_H)$). The results of the calculations can be seen in Fig. 1 right side, where the angular dependencies of all effects are shown. The fitting of the experimental data is a linear combination of the relevant effects.

In Fig. 2 the measurements for the angular dependence of V_{sym} and V_{asym} are shown for RF magnetron sputtered Py/Al and Py/Pt and epitaxially grown Fe/MgO and Fe/Pt bilayers. Since Al and MgO bear no significant spin-orbit interaction, Py/Al and Fe/MgO should not exhibit ISHE. Those samples should only primarily have AMR and AHE caused by $I_{z'}$ and $h_{x'}$. What can be seen, is that in Fe/MgO AHE seems to be more prominent than AMR, seen from the lack of side-maxima occuring with AMR at angles around 90° and 270°, while in Py/Al it seems to be contrary. Additionally the epitaxial Fe/MgO sample shows pronounced features around angles, where the external field is oriented around the magnetic hard axis of Fe. This could be due to the intrinsic magnetic anisotropy influencing the angular dependencies of ISHE and SR. Py/Al and Py/Pt also show an antisymmetry around the central maximum, which is correlated to AMR with an out-of-plane dynamic magnetic field h_y, while this term is negligible for the Fe samples. This h_y-correlated AMR is not caused by a current in z', as it is the case for the other effects, but caused by a current 45° tilted to the z' direction. Those currents may be eddy currents, since they are flowing mostly along the edges of the layers and the edges of the rectangular samples are tilted by 45° [5]. This out-of-plane AMR is mainly visible in Py samples and is negligible for other materials, like Fe or

YIG.
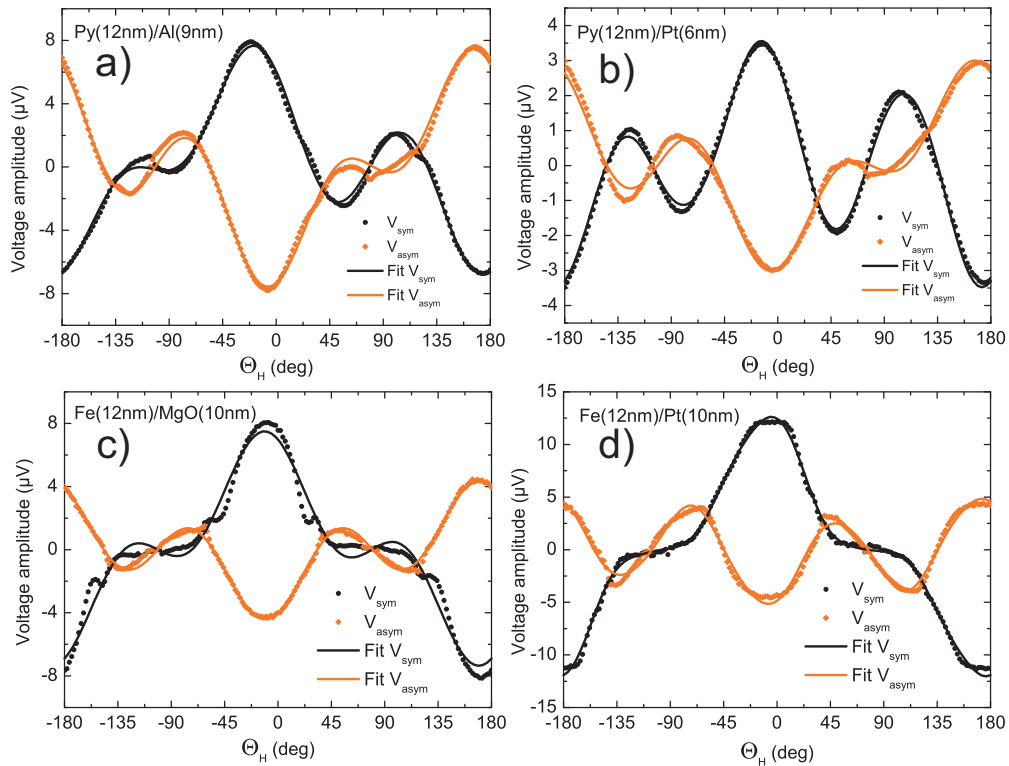
Fig. 2: Angular dependent spin pumping measurements of a) Py(12nm)/Al(10nm),b) Py(12nm)/Pt(10nm), c) Fe(12nm)/Mgo(10nm)and Fe(12nm)/Pt(10nm) at 13 GHz excitation frequency.

For comparison, a YIG(100 nm)/Pt(10nm) sample was also measured with this setup, shown in Fig. 3. The symmetrical voltage amplitude seems to be consisting mainly of a ISHE contribution and, surprisingly, of a contribution similar to AHE. The sample has a non-vanishing antisymmetrical voltage with angular dependencies similar to AMR and AHE. Other authors also reported rectification effects in YIG/Pt bilayers in spin pumping experiments at room temperature caused by spin Hall magnetoresistance (SMR) [6].

There is an intrinsic uncertainty with the method of rotating the external magnetic field in-plane and also having in-plane excitation $h_{x'}$. Eq. 2 shows that the main contributions of this measurement configuration, namely ISHE, AMR and AHE are mathematically linear dependent and therefore the fittings are not definite, as it is the case for Py/Pt, Fe/Pt and YIG/Pt. As one can see in Fig. 1, by changing the excitation from in-plane to out-of-plane (h_y), for example by using coplanar waveguide or microwave cavity, the effects can be clearly distinguished from each other.

$$\cos(2\Theta_H)\cos(\Theta_H) = [2\cos^2(\Theta_H) - 1]\cos(\Theta_H) = 2\cos^3(\Theta_H) - \cos(\Theta_H) \quad . \tag{2}$$

In conclusion, we have shown, that spin rectification effects do scale differently in Fe, Py and YIG bilayer systems, as summarized in Table 1: While AMR is more pronounced than AHE in RF magnetron sputtered Py, AHE seems to be almost equal in magnitude for epitaxial Fe systems (for comparison see Chapter 4.8 addressing CoFeB/Pt and CoFeB/Ta angular spin pumping measurements). Spin rectification, pronounced AHE in fact, is also occurring in nanometer thin YIG/Pt films by SMR. In Py/Al and Py/Pt there exists a non negligible out-of-plane excited AMR, that

$V_\text{sym}/V_\text{asym}$	Sample	ISHE (μV)	AHE (μV)	AMR (μV)	OOP-AMR (μV)
V_sym	Py/Al	0	1,43 ± 0,04	5,63 ± 0,06	1,68 ± 0,03
	Py/Pt	0,55*	-1,03*	3,92*	-0,61 ± 0,02
	Fe/MgO	0	2,52 ± 0,10	4,90 ± 0,14	-0,09 ± 0,07
	Fe/Pt	4,32*	3,46*	4,39*	0,24 ± 0,05
	YIG/Pt	-1,27*	-1,35*	0,00*	-0,04 ± 0,02
V_asym	Py/Al	0	-1,49 ± 0,05	-5,95 ± 0,07	-1,02 ± 0,04
	Py/Pt	0	-0,61 ± 0,03	-2,36 ± 0,04	-0,44 ± 0,02
	Fe/MgO	0	0,20 ± 0,03	-4,56 ± 0,05	-0,06 ± 0,02
	Fe/Pt	0	2,59 ± 0,11	-7,63 ± 0,15	-0,16 ± 0,08
	YIG/Pt	0	0,53 ± 0,02	0,20 ± 0,03	0,03 ± 0,02

Table 1: Results of the angular spin pumping measurements: Symmetrical and antisymmetrical voltage amplitudes. OOP-AMR is the acronym for out-of-plane excited AMR. Values marked with * are ambiguous. Absolute values between samples are not comparable because of different excitation frequencies or applied powers.
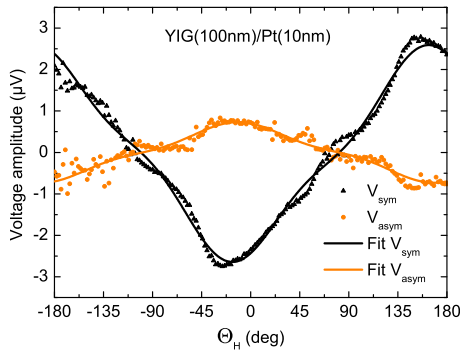
Fig. 3: Angular dependent spin pumping measurements of YIG(100nm)/Pt(10nm) at 6.4 GHz excitation frequency.

does not directly correlate with the microwave induced currents. Epitaxial Fe/MgO shows pronounced features around angles, where the external field is oriented around the magnetic hard axis of Fe. In-plane rotation of magnetization with in-plane dynamic magnetic excitation field exhibits ambiguities, when either ISHE, AMR or AHE are not negligible. In future experiments this will be avoided by out-of-plane excitation.

References

[1] F.D. Czeschka, L. Dreher, M.S. Brandt, M. Weiler, M. Althammer, I.-M. Imort, G. Reiss, A. Thomas, W. Schoch, W. Limmer, H. Huebl, R. Gross, and S.T.B. Goennenwein, *Scaling behavior of the spin pumping effect in ferromagnet/platinum bilayers*, arXiv:1012.3017v2 (2011).

[2] A. Azevedo, L.H. Vilela-Leão, R.L. Rodríguez-Suárez, A.F. Lacerdo Santos, S.M. Rezende, *Spin pumping and anisotropic magnetoresistance voltages in magnetic bilayers: Theory and experiment*, Phys. Rev. B **83**, 144402 (2011).

[3] R. Iguchi, and E. Saitoh, *Measurement of spin pumping voltage separated from extrinsic microwave effects*, arXiv:1607.04716v1 (2016).

[4] M. Harder, Y. Gui, and C.-M. Hu, *Electrical Detection of Magnetization Dynamics via Spin Rectification Effects*, arXiv:1605.00710v1 (2016).

[5] V. Flovik, and E. Wahlstrœm, *Eddy current interactions in a Ferromagnet-Normal metal bilayer structure, and its impact on ferromagnetic resonance lineshapes*, arXiv:1412.1385v3 (2015).

[6] P. Wang, S. W. Jiang, Z. Z. Luan, L. F. Zhou, H. F. Ding, Y. Zhou, X. D. Tao, and D. Wu, *Spin rectification induced by spin Hall magnetoresistance at room temperature*, J. Appl. Phys. **109**, 112406 (2016).

4.8 Spin pumping in CoFeB/Pt,Ta bilayers

A. Conca, B. Heinz, M.R. Schweizer, S. Keller, E.Th. Papaioannou, and B. Hillebrands

In spin pumping experiments [1, 2], the magnetization of a ferromagnetic layer (FM) in contact with a non-magnetic one (NM) is excited by a microwave field. A spin current is generated and injected into the NM layer and its magnitude is maximized when the ferromagnetic resonance (FMR) condition is fulfilled. The spin current can be detected by using the inverse spin Hall effect (ISHE) for conversion into a charge current in appropriate materials. The injected spin current in the NM layer has the form [1]

$$J_{\mathrm{s}} = \frac{\hbar}{4\pi} g^{\uparrow\downarrow} \hat{m} \times \frac{d\hat{m}}{dt} \quad, \tag{1}$$

where $\hat{m}$ is the magnetization unit vector and $g^{\uparrow\downarrow}$ is the spin mixing conductance which is controlling the intensity of the generated spin current. Its value is sensitive to the interface properties. The generation of the spin current represents an additional loss channel for the magnetic system and consequently produces an increase in the measured Gilbert damping parameter α:

$$\Delta\alpha_{\mathrm{sp}} = \frac{\gamma\hbar}{4\pi M_s\, d_{\mathrm{FM}}} g^{\uparrow\downarrow} \quad. \tag{2}$$

This expression is only valid for thick enough NM layers where no reflection of the spin current takes place at the interfaces. In principle, it allows the estimation of $g^{\uparrow\downarrow}$ by measuring the increase in damping compared to the intrinsic value. However, other phenomena, like the magnetic proximity effect (MPE) in the case of Pt or interface effects depending on the exact material combination or capping layer material, can have the same influence [3, 4], which challenges the measurement of the contribution from the spin pumping. In this sense, it is preferable to use an effective value $g_{\mathrm{eff}}^{\uparrow\downarrow}$. Still, if the spin pumping is the main contribution to the increase in α, a correlation between $g_{\mathrm{eff}}^{\uparrow\downarrow}$ and the measured ISHE voltages is expected.

Here, we report on results on polycrystalline $Co_{40}Fe_{40}B_{20}$/Pt,Ta bilayers grown by rf$-$sputtering on Si substrates passivated with SiO_2. A microstrip-based VNA-FMR setup was used to study the damping properties. For a more detailed description of the FMR measurement and analysis procedure see [3, 5]. A quadrupole-based lock-in setup was used in order to measure the ISHE generated voltage, (see Report 4.7 for details).
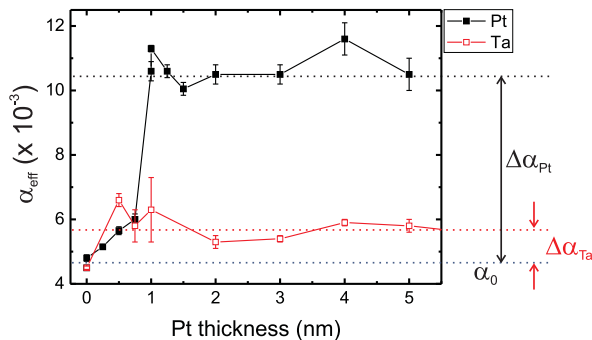

Fig. 1: Dependence of the effective Gilbert damping parameter α_{eff} on the thickness of the NM metal. A large increase in damping is observed for the Pt case while a very small but not vanishing increase is observed with Ta. From the change $\Delta\alpha$ the effective spin mixing conductance $g_{\mathrm{eff}}^{\uparrow\downarrow}$ is estimated using Eq. 2.
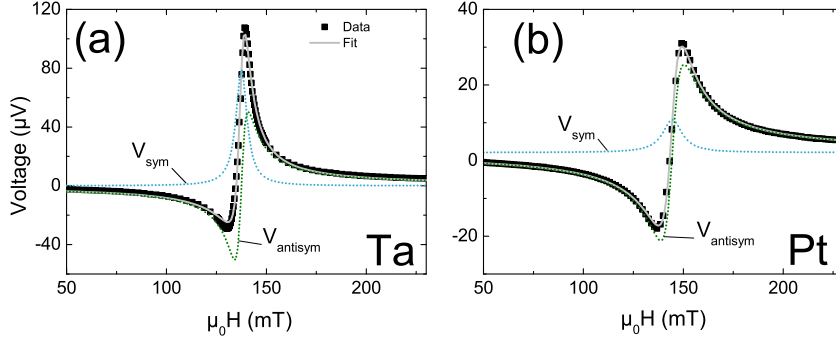
Fig. 2: Voltage spectra measured for (a) CoFeB/Ta and (b) CoFeB/Pt at 13 GHz. The solid line is a fit to Eq. 3. The symmetrical V_{sym} and antisymmetrical $V_{antisym}$ contribution are separated and plotted independently (dashed lines). The voltage signal is dominated by $V_{antisym}$ in the Pt case and by V_{sym} in the Ta case.

Figure 1 shows the dependence of the effective damping parameter α_{eff} (sum of all contributions) on the thickness of the NM metal and a CoFeB layer with a fixed 11 nm thickness. The case $d = 0$ nm represents the case of reference layers with Al capping. From previous studies in our group it is known that the use of an Al capping layer induces a large increase of damping in Fe epitaxial layers [3]. For polycrystalline NiFe and CoFeB layers this not the case and it allows the measurement of the intrinsic value α_0 [4].

The observed behavior differs strongly for Pt and Ta. In the Pt case a large increase in damping is observed with a sharp change around $d = 1$ nm and a fast saturation. This is qualitatively very similar to our previous report on Fe/Pt bilayers [3]. From the measured $\Delta\alpha$ we extract the value $g_{\mathrm{eff}}^{\uparrow\downarrow} = 6.2 \pm 0.5 \cdot 10^{19}\,\mathrm{m}^{-2}$. This value is larger than the one reported previously in our group for thinner CoFeB layers with larger intrinsic damping $4.0 \pm 1.0 \cdot 10^{19}\,\mathrm{m}^{-2}$ [4] and also larger than the value reported by Kim et al. [6], $5.1 \cdot 10^{19}\,\mathrm{m}^{-2}$. The impact of the Ta layer on damping is very reduced and, consequently, a low value for $g_{\mathrm{eff}}^{\uparrow\downarrow}$ of $0.9 \pm 0.3 \cdot 10^{19}\,\mathrm{m}^{-2}$ is obtained. This value is now smaller than the one reported by Kim et al. $(1.5 \cdot 10^{19}\,\mathrm{m}^{-2})$ indicating that the difference between CoFeB/Pt and Ta is larger in our case. A reference has also to be made to the work of Liu et al. on CoFeB films thinner than in this Report [7]. There, no value for the spin mixing conductance is provided, but the authors claim a vanishing impact on α for the Ta case. On the contrary the increase due to Pt is almost three times larger than ours, pointing to a huge difference between both systems. In any case, the trend is similar, only the relative difference between Ta and Pt changes.

Figure 2 shows two voltage measurements recorded at 13 GHz for a NM thickness of 3 nm. The measured voltage is the sum of the contribution of the ISHE effect and of spin rectification effects originating from the different magnetoresistive phenomena in the ferromagnetic layer. While the spin rectification effects generates both a symmetric and an antisymmetrical contribution [8–10], the pure ISHE signal is only symmetrical. For this reason a separation of both is carried out by fitting the voltage spectra (solid line) to

$$V_{meas} = V_{sym} \frac{(\Delta H)^2}{(H - H_{\mathrm{FMR}})^2 + (\Delta H)^2} + V_{antisym} \frac{-2\Delta H(H - H_{\mathrm{FMR}})}{(H - H_{\mathrm{FMR}})^2 + (\Delta H)^2} \quad , \qquad (3)$$

where ΔH and H_{FMR} are the linewidth and the resonance field, respectively. The dotted lines in Fig. 2 show the two contributions. When comparing the data for Pt and Ta some differences are observed. First of all, the absolute voltage values are smaller for the Pt cases and, more important, the relative weight of both contributions is different. While the first point is related to the different conductivity of Ta and Pt, the second one is related to the intrinsic effect causing the voltage. In
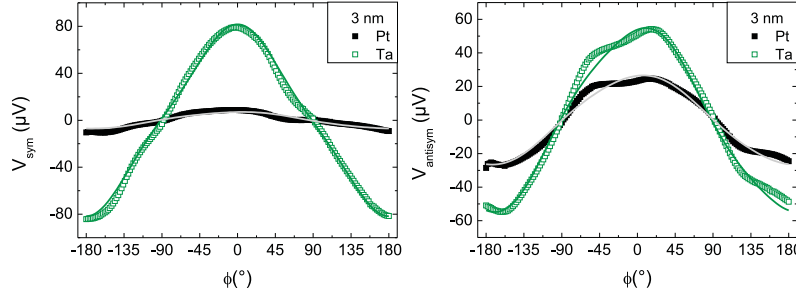
Fig. 3: Angular dependence of V_{sym} (left) and $V_{antisym}$ (right) for CoFeB/Pt,Ta samples with NM thickness of 3 nm. The lines are a fit to the model described in Eqn. 4.

the Pt case the antisymmetrical contribution is dominating with a ratio $S/A = V_{sym}/V_{antisym} = 0.37$ while the opposite is true for Ta with $S/A = 1.55$. Since the ISHE signal is contributing only to V_{sym} it might be concluded that spin pumping is taking place stronger in the Ta system. However, since also the spin rectification effect has a symmetrical contribution, this conclusion cannot be supported. Furthermore, since the spin Hall angle θ_{SHE} has an opposite sign in these two materials, also the ISHE signal should have it. In apparent contradiction to this, we observe that both symmetrical contributions have the same sign. This is pointing to the fact that for Pt, V_{sym} is dominated by the spin rectification effect, which does not change sign and overcompensates a smaller ISHE signal. All these considerations have the consequence that it is not possible to extract complete information of the origin of the measured voltage by analyzing single spectra. As already pointed out by many authors [8–11] and shown in Report 4.7, an analysis of the angular dependence (in-plane or out-of-plane) of the measured voltages can be used to separate the different contributions.

We performed in-plane angular dependent measurements of the voltage and Eq. 3 was used to extract $V_{sym,antisym}$ for each value of the azimuthal angle ϕ spanned between the direction of the magnetic field and the microstrip antenna used to excite the magnetization. We used a model based on the work of Harder et al. [8] to fit the dependence. This model considers two sources for the spin rectification, the anisotropic magnetoresistance (AMR) and the anomalous Hall effect (AHE):

$$
\begin{aligned}
V_{sym} &= V_{sp}\cos^3(\phi) + \\
&+ V_{AHE}\cos(\Phi)\cos(\phi) + V_{AMR-\perp}^{sym}\cos(2\phi)\cos(\phi) + V_{AMR-\parallel}^{sym}\sin(2\phi)\cos(\phi) \quad (4) \\
V_{antisym} &= V_{AHE}\sin(\Phi)\cos(\phi) + V_{AMR-\perp}^{antisym}\cos(2\phi)\cos(\phi) + V_{AMR-\parallel}^{antisym}\sin(2\phi)\cos(\phi) \quad (5)
\end{aligned}
$$

Here, V_{sp} and V_{AHE} are the contributions from spin pumping (pure ISHE) and from AHE, respectively. Φ is the phase between the rf electric and magnetic fields in the medium. The contribution from the AMR is divided in one generating a transverse $\perp$ (with respect to the antenna) or longitudinal $\parallel$ voltage. In an ideal case with perfect geometry and point-like electrical contacts $V_{AMR-\parallel}^{sym,antisym}$ should vanish.

Figure 3 shows the angular dependence of V_{sym} (left) and $V_{antisym}$ (right) for the samples with NM thickness of 3 nm. The lines are a fit to the model. From the data is clearly recognizable that while the values of $V_{antisym}$ are comparable, the values of V_{sym} are much larger for Ta. In order to compare the relative magnitudes of the different contributions we compute the quantities

AG MAGNETISMUS
TU KAISERSLAUTERN

	V_{sp}	V_{AHE}	$V_{\text{AMR}-\perp}$	$V_{\text{AMR}-\parallel}$
Ta	23.9 ± 1.5	59.3 ± 3	2.1 ± 0.7	4.7 ± 0.6
Pt	0.0 ± 0.7	27.3 ± 0.4	0.6 ± 0.5	1.9 ± 0.4

Table 1: Value of the different contributions to the measured voltage extracted from the angular dependence for CoFeB/Pt,Ta (3 nm) bilayers. Values in μV.

$$V_{\text{AMR}-\parallel,\perp} = \sqrt{\left(V_{\text{AMR}-\parallel,\perp}^{antisym} \right)^2 + \left(V_{\text{AMR}-\parallel,\perp}^{sym} \right)^2}$$ and we show them together with V_{AHE} and V_{sp} in Table 1.

Certain conclusions can be extracted from this data. First of all, the spin rectification effect in CoFeB systems are dominated by the AHE. AMR plays a minor role. This is a difference with respect to NiFe [9]. Secondly, while the spin pumping is efficient in Ta, we were not able to see it in Pt, that is, there is a lack of correlation between $g_{\text{eff}}^{\uparrow\downarrow}$ and the detected ISHE voltage. Two non mutually excluding explanations are possible here: $\Delta\alpha$ in Pt in mainly due do the MPE, or the spin current pumped into Pt vanishes at or close to the interface. In order to further clarify and confirm this result, measurements with different NM thicknesses and with the inclusion of interlayers are being carried out. In any case, CoFeB/Ta shows very interesting properties, with strong spin pumping accompained by only a minor impact on α.

References

[1] Y. Tserkovnyak, A. Brataas, G. E. W. Bauer, B. I. Halperin, *Nonlocal magnetization dynamics in ferromagnetic heterostructures*, Rev. Mod. Phys. **77**, No. 4, 1375 (2005).

[2] Y. Tserkovnyak, A. Brataas, G. E. W. Bauer, *Dynamic exchange coupling in magnetic bilayers*, Phys. Rev. Lett. **88**, 117601 (2002).

[3] A. Conca, S. Keller, L. Mihalceanu, T. Kehagias, G. P. Dimitrakopulos, B. Hillebrands, E. Th. Papaioannou, *Study of fully epitaxial Fe/Pt bilayers for spin pumping by FMR spectroscopy*, Phys. Rev. B **93**, 134405 (2016).

[4] A. Ruiz-Calaforra, T. Brächer, V. Lauer, P. Pirro, B. Heinz, M. Geilen, A. V. Chumak, A. Conca, B. Leven, B. Hillebrands, *The role of the non-magnetic material in spin pumping and magnetization dynamics in NiFe and CoFeB multilayer systems*, J. Appl. Phys. **117**, 163901 (2015).

[5] A. Conca, E. Th. Papaioannou, S. Klingler, J. Greser, T. Sebastian, B. Leven, J. Lösch, B. Hillebrands, *Annealing influence on the Gilbert damping parameter and the exchange constant of CoFeB thin films*, Appl. Phys. Lett. **104**, 182407 (2014).

[6] D.-J Kim, S.-I. Kim, S.-Y. Park, K.-D. Lee, B.-G. Park, *Ferromagnetic resonance spin pumping in CoFeB with highly resistive non-magnetic electrodes*, Current Appl. Phys. **14** 1344 (2014). Please note the different stoichiometry: $Co_{32}Fe_{48}B_{20}$.

[7] L. Liu, C.-F. Pai, Y. Li, H. W. Tseng, D. C. Ralph, R. A. Buhrman, *Spin-torque switching with the giant spin Hall effect of tantalum*, Science **336**, 555 (2012).

[8] M. Harder, Y. Gui, C.-M. Hu, *Electrical detection of magnetization dynamics via spin rectification effects*, arXiv:1605.00710v1 [cond-mat.mtrl-sci] (2016).

[9] W. T. Soh, B. Peng and C. K. Ong, *An angular analysis to separate spin pumping-induced ISHE from spin rectification in a Py/Pt bilayer*, J. Phys. D: Appl. Phys. **47** 285001 (2014).

[10] Y. Gui, L. Bai, C. Hu, *The physics of spin rectification*, Sci. China-Phys. Mech. Astron. **56**, 124 (2013).

[11] R. Iguchi, E. Saitoh, *Measurement of spin pumping voltage separated from extrinsic microwave effects*, arXiv:1607.04716v1 [cond-mat.mtrl-sci] (2016).

4.9   Spin-wave density of states and microfocussed Brillouin light scattering spectra as a function of magnetic film thickness

M. Geilen, T. Meyer, F. Heussner, B. Hillebrands, and P. Pirro

The interplay of dipolar and exchange energies in thin magnetic films leads to a rich variety in the dispersion relations of different spin-wave modes. For the design and understanding of novel spin-wave devices, this spin-wave band structure and the resulting density of states (DOS) is an important parameter since it has a strong influence on nonlinear spin-wave interactions [1]. On the other hand, from the viewpoint of microfocussed Brillouin light scattering (µBLS) experiments, the knowledge of the DOS is essential to develop a model which quantitatively describes the frequency dependence of the observed BLS intensity. This intensity depends on the DOS, but also on many other parameters, which are related to the experimental setup (e.g. the wave-vector distribution of the incident laser light) or to the efficiency of the photon-magnon scattering itself, also referred to as BLS scattering cross section. Thus, to make a first step towards a quantitative understanding, in this Report, we compare µBLS spectra obtained from NiFe films of different thicknesses with the calculated spin-wave DOS.

In thin magnetic films, the exchange interaction leads to a significant splitting between the dispersion relations of the spin-wave modes described by the mode number n with different quantized wave vector k_z along the film thickness t, with $k_z(n) = \frac{n\pi}{t}$ if unpinned surface spins are assumed. For $n > 0$, the modes are commonly known as perpendicular standing spin-wave modes (PSSW), since the group velocity of these modes is much smaller than the one of the fundamental mode $n = 0$. Due to the large frequency difference between modes with different mode number n but same in-plane wave vector, the most useful approach is to treat the system as two-dimensional with different energy levels defined by the quantization n of the out-of-plane wave vector. If we assume the in-plane field and the static magnetization to be aligned along the x-axis, the dispersion relation for the spin waves can be approximated by [4]:

$$f(k, \theta, n) = \sqrt{(f_H + V_{\text{ex}} k^2)(f_H + V_{\text{ex}} k^2 + f_M F_{nn}(k, \theta))}. \tag{1}$$

With the in-plane wave vector $k_{\text{in}} = \sqrt{k_y^2 + k_x^2}$, $\tan(\theta) = \frac{k_y}{k_x}$, the total wave vector $k = \sqrt{k_{\text{in}}^2 + k_z^2}$ and $V_{\text{ex}} = \gamma \cdot D_{ex} = \gamma \cdot \frac{2A}{M_s}$ (for further definitions of the elements, see [4]).

The DOS $D(f)$ is generally defined as the number of available states per frequency interval df at the frequency f (here for the 2D case):

$$D(f) = \frac{1}{S} \sum_{\mathbf{k} \in K} \delta(f - f(\mathbf{k})) \tag{2}$$

which in the continuum approximation becomes:

$$D(f) = \int_K \frac{d\mathbf{k}}{(2\pi)^2} \delta(f - f(\mathbf{k})) = \int_{f(\mathbf{k})=f} \frac{d\mathbf{k}}{(2\pi)^3} \frac{1}{|\mathbf{v}_g(\mathbf{k})|} \tag{3}$$

Here, S and K are the total surface in real and wave-vector space, respectively, and $\mathbf{v}_g(\mathbf{k}) = 2\pi \nabla_{\mathbf{k}}(f(\mathbf{k}))$ is the group velocity of the spin waves. To obtain $D(f)$, we numerically evaluate
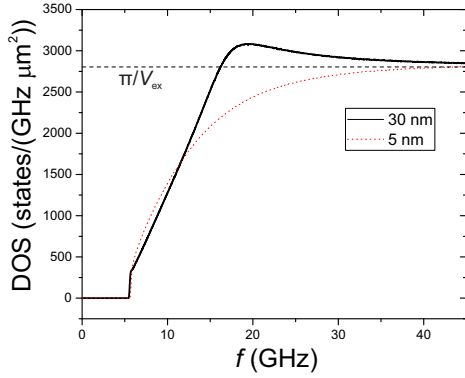
Fig. 1: Density of states (DOS) of the spin-wave mode $n = 0$ for an in-plane magnetized film of NiFe for two different film thicknesses as a function of the spin-wave frequency. For high frequencies, the dispersion relation is dominated by exchange and the DOS converges towards its pure exchange value of π/V_{ex}.

Eqn. 2 for the dispersion relations given in Eqn. 1. Exemplarily, Fig. 1 shows the DOS for the $n = 0$ mode for two different film thicknesses in the range from 0 to 45 GHz [1]. In general, it is important to notice that due to the interplay between dipolar and exchange energies, the spin-wave frequency f usually features a local minimum f_{min} for a finite wave vector k_{min}. This leads to a so-called critical point also known as Van-Hove singularity [2, 3] in the DOS at f_{min} since the term $1/\mathbf{v}_g(\mathbf{k})$ is diverging. Similar to a 2D electron system [3], this leads to a step-like increase of the DOS at the minimal frequency of the band. For the frequencies where the dispersion is strongly influenced by the dipolar interaction, the DOS is increasing almost linearly with f. In the high frequency limit, the dispersion is dominated by the exchange interaction and mathematically equivalent to the free electron gas in 2D. In this case, Eqn. 3 predicts a constant DOS of π/V_{ex}, which is in good agreement with the numerical calculations.

To be able to compare the DOS with experimentally obtained µBLS spectra, NiFe films with thicknesses in the range from $t = 5$ to 100 nm have been prepared by sputter deposition on oxidized Si substrates (100 nm SiO_2 thickness) and capped with 7 nm of Al. From all films, thermal spin-wave spectra have been measured using µBLS (532 nm laser wavelength, 0.75 numerical aperture of the focussing objective) at an external magnetic field of 40 mT applied in the film plane. All measurements have been performed with constant experimental parameters to be able to compare the BLS intensities from different thicknesses. Figure 2 shows exemplary BLS spectra for $t = 5$, 30, 60 and 100 nm. Based on this kind of raw data, Fig. 3 shows the BLS intensity for the modes $n = 0$ and $n = 1$ integrated over the frequency interval in which the signal from the spin waves could be discriminated from the noise of the measurement. The observed BLS intensity shows a significant change for the $n = 0$ mode when the film thickness is varied. For this mode, the largest BLS intensity has been obtained from the thinnest film ($t = 5$ nm), where a narrow peak is observed. With increasing thickness, the $n = 0$ peak is broadening and its maximum intensity is decreasing. For example, at $t = 100$ nm, the maximum peak intensity is about two orders of magnitude lower compared to $t = 5$ nm. As can be comprehended from Fig. 3a, also a general decrease of the frequency-integrated BLS signal with increasing thickness t is observed. In contrast, for the $n = 1$ mode, a clear trend has not been observed within in thickness range where this mode could be detected[2].

As a first comparison of the obtained BLS spectra with the spin-wave DOS, Fig. 4 shows the DOS for the modes $n = 0$ in Fig. 4a and $n = 1$ in Fig. 4c for different film thicknesses.[3] For $n = 0$,

---

[1] $M_{\text{eff}} = 800$ kA/m, $A_{\text{ex}} = 16$ pJ/m, gyromagnetic ratio $\gamma = 28$ GHz.

[2] For $t < 30$ nm, the frequencies of the $n > 0$ modes are larger than the maximum observed frequency (30 GHz).

[3] For this calculation, a thickness dependent effective magnetization based on the results of Ref. [5] has been used
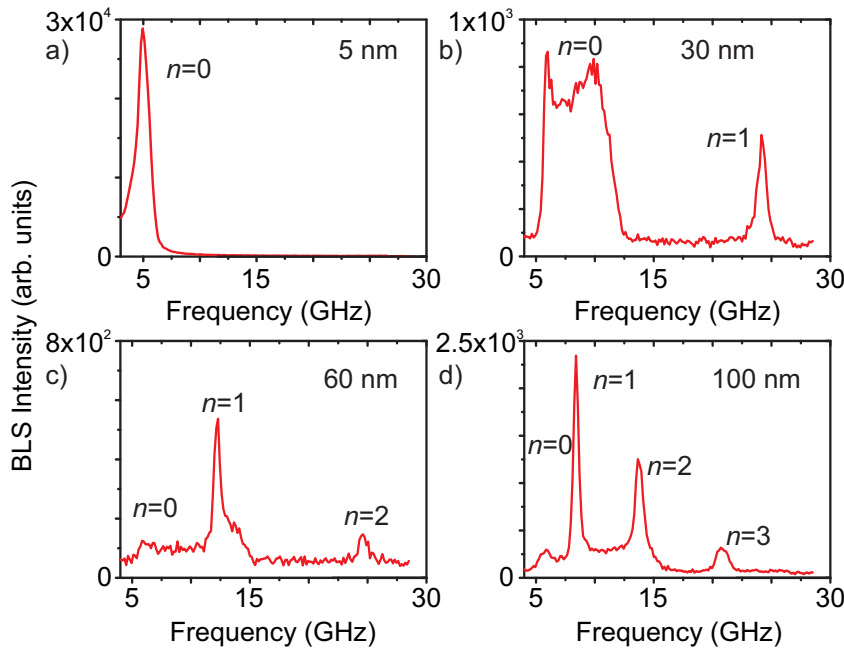
Fig. 2: BLS intensity spectra for different NiFe film thicknesses. The maximum intensities of the different thickness modes are labeled.

the minimum frequency of the dispersion is a function of the films thickness due to the thickness dependence of M_{eff} and due to the increasing strength of the dipolar interaction with increasing t. In the depicted frequency range, the DOS is increasing with f since the exchange dominated regime is not reached yet (compare Fig. 1). Compared to the obtained BLS intensities, it is obvious that the magnitude of the BLS signal cannot be explained only by the DOS since the variation of the latter is rather weak when t is changed. Thus, the wave-vector dependence of the µBLS sensitivity has to be taken into account. As a first step, this sensitivity is modeled using a Gaussian weighting function ($FWHM = 8.5\,\mathrm{rad/\mu m}$) multiplied to every addend in Eqn. 2 to take into account the wave-vector distribution of the incoming laser light. This crude approximation is only considering the in-plane wave-vector distribution of the incoming laser light determined by the numerical aperture of the used microscope objective, but it does not take into account the BLS scattering cross section itself. The modeled signal strength is shown in Fig. 4b and c for $n = 0$ and $n = 1$, respectively. Despite the strongly simplified model, the shapes of the modeled BLS spectra are in reasonable agreement with the experiment. Also the general trend that the intensity peak height for $n = 0$ is decreasing with increasing t is reproduced. However, the maximum intensity in the experiment is decreasing stronger with t than predicted by the model which could be evidence that the BLS scattering cross

Fig. 3: Integrated BLS intensity for a) $n = 0$ and b) $n = 1$ as a function of the NiFe film thicknesses.

with M_{eff} increasing from $738\,\mathrm{kA/m}$ for $t = 5\,\mathrm{nm}$ to $844\,\mathrm{kA/m}$ for $t = 100\,\mathrm{nm}$. Fixed parameters: $A_{ex} = 16\,\mathrm{pJ/m}$ and $\gamma = 28\,\mathrm{GHz}$.

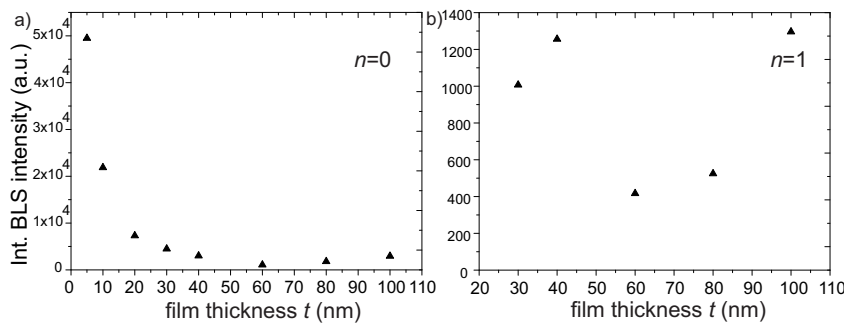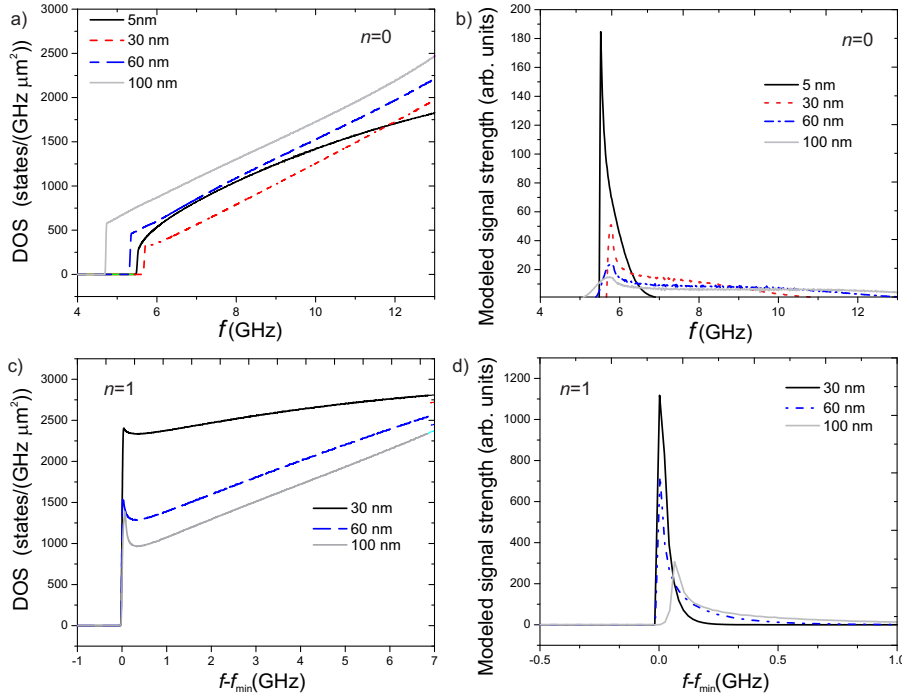Fig. 4: Spin-wave DOS (for $n = 0$ in a), for $n = 1$ in c)) and the modeled BLS intensity (for $n = 0$ in b), for $n = 1$ in d)) for different NiFe film thicknesses. For a better overview, the frequency axis for the mode $n = 1$ has been shifted by the respective minimum frequency f_{min} of this mode.

section itself is changing with the film thickness. When comparing the modes $n = 0$ and $n = 1$, the ratio of the modeled maximum BLS intensities is rather independent of the thickness. However, in the experiment, this ratio is a function of the thickness (compare Fig. 2b and c for example). This might be related to the finite penetration depth of the laser into the NiFe which could have a different influence on the BLS scattering cross section depending on the mode number n.

To conclude, we presented a first study attempting to quantify the intensity obtained in μBLS experiments by considering the thickness and frequency dependence of the spin-wave DOS. Due to the strong wave-vector dependence of the μBLS sensitivity, the frequency dependence of the intensity is in general not proportional to the DOS. A simple model is able to include the wave vector dependence qualitatively, but a more accurate description will need to include the thickness dependence of the magnon-photon scattering in more detail.

References

[1] A. L. Chernyshev, *Field dependence of magnon decay in yttrium iron garnet thin films*, Phys Rev B **86**, 060401 (2012).

[2] L. van Hove, *The occurrence of singularities in the elastic frequency distribution of a crystal*, Physical Review **89**, 1189 (1953).

[3] F. Bassani, G. Pastori Parravivini, R.A. Ballinger, *Electronic states and optical transitions in solids*, Pergamon Press (1975).

[4] B.A. Kalinikos and A. Slavin, *Theory of dipole-exchange spin wave spectrum for ferromagnetic films with mixed exchange boundary conditions*, Journal of Physics C: Solid State Physics **19**, 7013 (1986).

[5] A. Ruiz-Calaforra, T. Brächer, V. Lauer, P. Pirro, B. Heinz, M. Geilen, A.V. Chumak, A. Conca, B. Leven, and B. Hillebrands, *The role of the non-magnetic material in spin pumping and magnetization dynamics in NiFe and CoFeB multilayer systems*, J. Appl. Phys. **117**, 163901 (2015).

4.10 Voltage-controlled magnonic crystal

Q. Wang, A.V. Chumak, and B. Hillebrands

In collaboration with Lichuan Jin, Huaiwu Zhang and Zhiyong Zhong, State Key Laboratory of Electronic Thin Films and Integrated Devices, University of Electronic Science and Technology of China, Chengdu, 610054, China

Spin waves (SWs) are the eigen excitations of a spin system of a magnetic material. They have wavelengths orders of magnitude shorter than the wavelengths of electromagnetic waves of the same frequency, and thus, allow for the design of nano-scale devices [1–3]. Recent experimental and theoretical discoveries have shown that there is much potential for the use of spin waves for transfer [4], processing [5], and (short-time) storage of information [6]. An external control of spin waves, which is of key importance in these prototype devices, was realized using the application of, e. g., an electric current-induced magnetic field [7], a spin-polarized current [8], skyrmions [9], or laser light [10]. The spin-wave control by an electric field opens access to a new type of magnonic devices with decreased energy consumption [11]. Here we use electric field-induced perpendicular magnetic anisotropy (PMA) to develop a nano-scale reconfigurable magnonic crystal (MC) that is an universal magnonics component suitable for versatile operations with data.

In this work, a nano-scale reconfigurable magnonic crystal is designed using voltage-controlled perpendicular magnetic anisotropy (PMA) in ferromagnetic-dielectric hetero-structures. The investigated structure is schematically shown in Fig. 1a. The MC consists of a 1.5 nm thick Cobalt (Co) strip placed on the substrate and covered with a MgO layer. Gate metallic strips of $L = 10$ nm width are periodically placed on top of the MgO layer with a $P = 30$ nm periodicity (see Fig. 1b). This periodic structure is 1.6 µm long, includes 53 gate metallic strips, and is placed in the middle of the 2 µm-long and $w = 40$ nm wide Co strip. The voltage is applied between these gate electrodes and the Co strip in order to control the PMA at the Co/MgO interface. Consequently, the voltage-controlled PMA modulates the local perpendicular component of the anisotropy field H_z under the gate metallic strips and induces a periodic spatial distribution of the internal field and the component of the saturation magnetization M_z. The periodic variation of the internal field, consequently, causes partial or total Bragg reflection of spin waves propagating through the MC.

In order to excite spin waves in a wide frequency range from 0 to 200 GHz, a sinc field pulse $h_y(t) = H_0 \sin(2\pi f_{max} t)/(2\pi f_{max} t)$, is applied locally (in the volume $2 \times 40 \times 1.5$ nm^3) at the 100 nm position from the left edge of the waveguide. In our simulations, the magnetic field is $H_0 = 1000$ Oe and the cutoff frequency is $f_{max} = 200$ GHz. The numerically calculated SW frequency spectra, transmission characteristics, and dispersion curves are displayed in Fig. 2. The top and the bottom panels indicate the characteristic spin-wave propagation properties in the waveguide without and with an applied voltage in the static regime, respectively. The SW frequency spectra in terms of frequency f versus propagation distance x are obtained by a FFT of M_z on the time scale. The SW transmission characteristics are obtained by the integration of the SW intensity in space over the distance from 1800 nm to 1900 nm along the x-axis. The dispersion curves in terms of frequency f versus wavevector k_x are obtained by a 2D FFT of M_z in both space and time.

Low values of the magnetization precession amplitude are shown in Fig. 2 in dark, while high values of the precession amplitude, are shown in bright. When no voltage is applied to the structure,
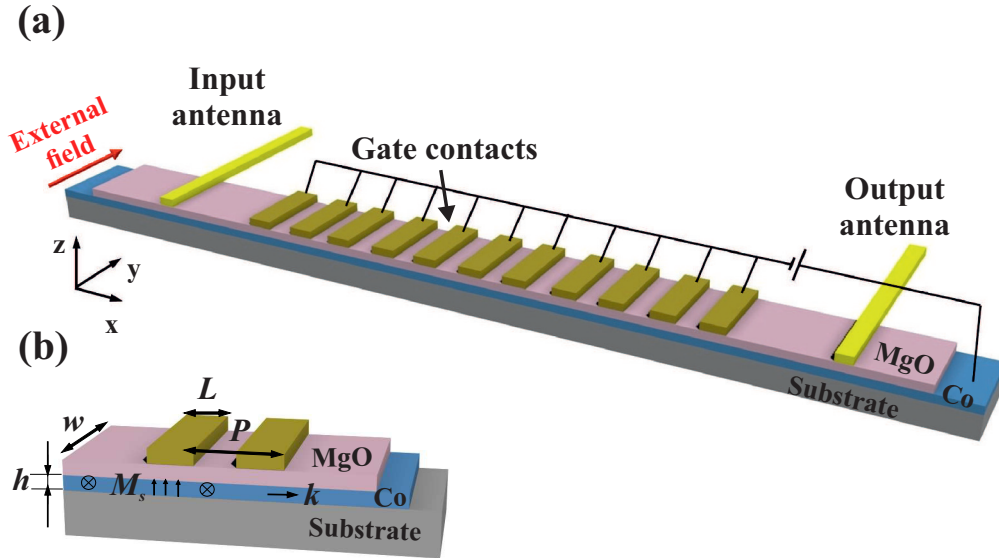
(a)

(b)

Fig. 1: (a) Schematic view of the voltage-controlled reconfigurable magnonic crystal. (b) Close-up view of the waveguide. An ultrathin Co film of $h = 1.5\,$nm thickness is placed on the substrate and is covered by an insulating MgO film. The gate metallic stripes are periodically placed on the MgO surface. The width and period of the gate metals are 10 nm and 30 nm, respectively. An electric field is applied between the gate strips and the Co layer in order to induce PMA.

there are no band gaps observed in the allowed spin-wave band above 6.8 GHz - see Fig. 2a-c. Figure 2b shows that the maximum spin-wave intensity corresponds to an FMR frequency of around 6.8 GHz. The intensity decays with an increase in the frequency due to an increase in the damping for high-frequency SWs and a decrease in the excitation efficiency. The SW intensity fluctuations for waves of different frequencies, observed in Fig. 2b, are due to the interference between the fundamental and third order width modes as well as between the forward SWs and the SWs reflected from the edge of the structure.

The characteristics of propagating SWs are modified when a voltage is applied to the periodic gate strips. Figure 2d clearly reveals the formation of the allowed and the forbidden bands in the SW transmission. Two distinct band gaps appear near 23 GHz and 70 GHz with widths of 4.1 GHz and 2.6 GHz, respectively. By comparing the SW transmission characteristic with the SW dispersion curve, one can see that the center frequencies of the band gaps are correlated to the first and the second Brillouin zone boundaries of the MC, i.e., $k_x = \pi/P = 0.105\,$rad/nm and $2\pi/P = 0.21\,$rad/nm, respectively. The occurrence of the band gaps at the Brillouin zone boundaries is due to Bragg reflection of the propagating SWs from the voltage-induced, periodically-varied magnetization. Figure 2 demonstrates one of the key points of this report: voltage-controlled PMA can induce SW band gaps in a uniform nanostripe waveguide and the switching time is less than 10 ns, which opens the path to fast, low loss, low power, and voltage controlled band gaps.

Furthermore, the application of the voltage to only selected gate strips opens an additional degree of freedom for the control of spin-wave properties. A simple example of such an application is shown in Fig. 3. The top panel Fig. 3c shows the top view of the waveguide, where the periodic rectangles represent the metal gate strips on the waveguide. The width and periodicity of the gate stripes are 10 nm and 20 nm, respectively. All the metal gates are periodically encoded by the numbers "1", "2", and "3" as shown in Fig. 3c. The voltage is either applied to all gate strips (gates 1, 2, 3), to only strips number 1 and 2, or only to number 1 strips. The spatial distributions
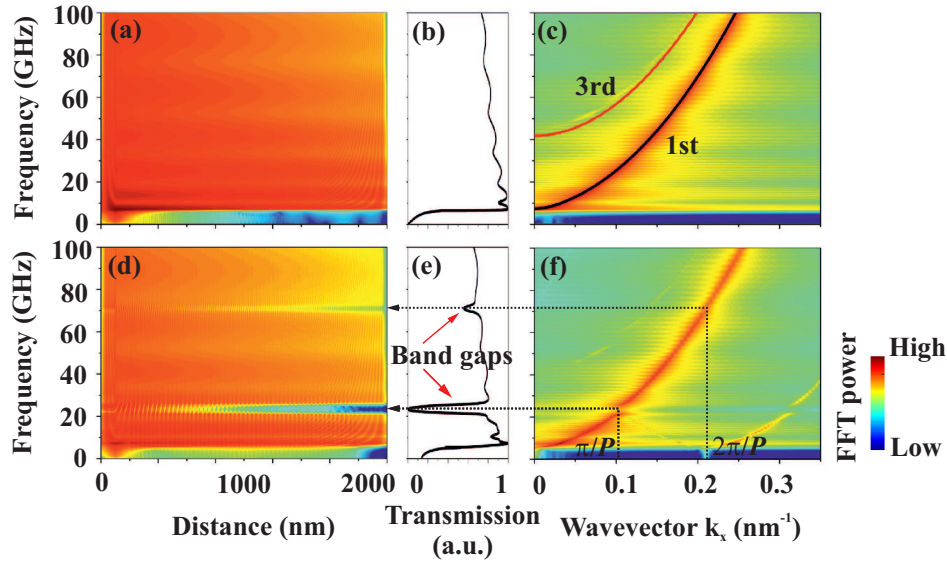
Fig. 2: The top panels (a)-(c) show spin-wave propagation through the uniform spin-wave waveguide without a voltage applied to the gate stripes. The bottom panels (d)-(f) show spin-wave transmission through the magnonic crystal when a voltage corresponding to $E = 2\,\mathrm{V/nm}$ value is applied to the gate stripes. (a), (d) Frequency spectra obtained from a FFT of the temporal evolution of M_z. (b), (e) SW transmission characteristics obtained by integrating the SW intensity over the waveguide area from 1800 nm to 1900 nm along the x-axis. (average of all the points along the width direction) (c), (f) Dispersion curves obtained by a 2D FFT of temporal M_z in space and time. The lines in (c) are obtained by analytical calculation of the first and the third width modes, respectively. The dotted lines in (f) denote the positions of the band gaps and the corresponding wave vectors k_x.

of the z-component of magnetization for these three particular cases are shown in Fig. 3c in the bottom panels. The periodicities of the magnonic crystals are changed by applying the voltage in different manners and, as a result, the spin-wave spectra are modified in different ways. For the first case, when the voltage is applied to all the gate strips, only one band gap is observed at a frequency of about 42.2 GHz shown in Fig. 3a. In the second and third case, we observe two additional band gaps at frequencies of around 23.5 GHz and 10.6 GHz, respectively. To interpret this result, we perform a FFT of the magnetization M_z along the x direction and combine the dispersion curve obtained by simulation and theory. The FFT provides the magnetization distribution in reciprocal space as shown in Fig. 3d. Combining the dispersion curve, the existence/absence of each band gap is clearly visible. We can dynamically apply the voltage to different gates to obtain programmable transmission characteristics for the propagation of the SWs. The above-mentioned voltage-controlled reconfigurable MC is a simple example. Many other structures can be designed to realize more complex functions.

In summary, we have demonstrated a reconfigurable magnonic crystal based on the use of voltage-controlled perpendicular magnetic anisotropy. The voltage-controlled PMA induces a spatial variation of the internal field along the waveguide resulting in pronounced band gaps in the spin-wave spectra. Finally, we designed a reconfigurable magnonic crystal whose band gaps can be dynamically controlled by applying a voltage to different metallic gates. Our proposal opens the path to low loss, low power voltage-controlled reconfigurable magnonic crystals that can be used in future nano-sized magnon spintronics devices.

AG MAGNETISMUS
TU KAISERSLAUTERN
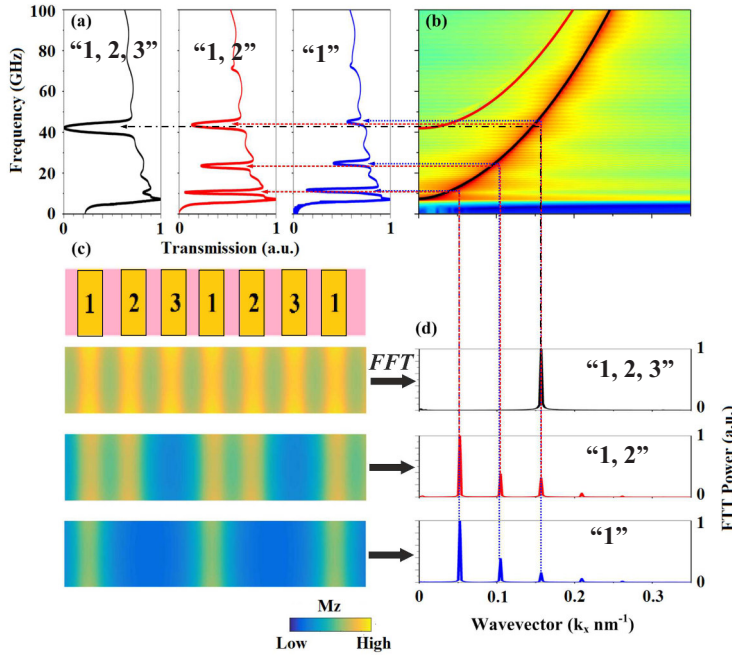
Fig. 3: Transmission characteristic of different structures. (b) Dispersion curve obtained by micromagnetic simulation (color map) and analytic theory for the first and the third width mode. (c) The first line is a top view of the waveguide while the others are the spatial magnetization distribution for different structures of the voltage gates. (d) Fourier transform of the magnetization along the x direction for different structures of voltage gates shown in panel (c).

References

[1] V.V. Kruglyak, S.O. Demokritov, D. Grundler, *Magnonics*, J. Phys. D: Appl. Phys. **43**, 264001 (2010).

[2] A.V. Chumak, V.I. Vasyuchka, A.A. Serga, B. Hillebrands, *Magnon spintronics*, Nat. Phys. **11**, 453 (2015).

[3] M. Krawczyk, D. Grundler, *Review and prospects of magnonic crystals and devices with reprogrammable band structure*, J. Phys.: Condens. Matter **26**, 123202 (2014).

[4] Y. Kajiwara, K. Harii, S. Takahashi, J. Ohe, K. Uchida, M. Mizuguchi, H. Umezawa, H. Kawai, K. Ando, K. Takanashi, S. Maekawa, E. Saitoh, *Transmission of electrical signals by spin-wave interconversion in a magnetic insulator*, Nature **464**, 262 (2010).

[5] T. Schneider, A.A. Serga, B. Leven, B. Hillebrands, R.L. Stamps, M.P. Kostylev, *Realization of spin-wave logic gates*, Appl. Phys. Lett. **92**, 022505 (2008).

[6] A.V. Chumak, V.I. Vasyuchka, A.A. Serga, M.P. Kostylev, V.S. Tiberkevich, B. Hillebrands, *Storage-recovery phenomenon in magnonic crystal*, Phys. Rev. Lett. **108**, 257207 (2012)

[7] K. Vogt, F.Y. Fradin, J.E. Pearson, T. Sebastian, S.D. Bader, B. Hillebrands, A. Hoffmann, H. Schultheiss, *Realization of a spin-wave multiplexer*, Nat. Commun. **5**, 4727 (2014).

[8] Q. Wang, H.W. Zhang, X.L. Tang, H. Fangohr, F.M. Bai, and Z.Y. Zhong, *Dynamic control of spin wave spectra using spin-polarized currents*, Appl. Phys. Lett. **105**, 112405 (2014).

[9] F.S. Ma, Y. Zhou, H.B. Braun, W.S. Lew, *Skyrmion-based dynamic magnonic crystal*, Nano. Lett. **15**, 4029 (2015).

[10] M. Vogel, A.V. Chumak, E.H. Waller, T. Langner, V.I. Vasyuchka, B. Hillebrands, G. von Freymann, *Optically reconfigurable magnetic materials*, Nat. Phys. **11**, 487 (2015).

[11] T. Nozaki, Y. Shiota, S. Miwa, S. Murakami, F. Bonell, S. Ishibashi, H. Kubota, K. Yakushiji, T. Saruya, A. Fukushima, *Electric-field-induced ferromagnetic resonance excitation in an ultrathin ferromagnetic metal layer*, Nat. Phys. **8**, 491 (2012).

4.11   A switchable spin-wave signal splitter for magnonic networks

F. Heussner, P. Pirro, A.A. Serga, and B. Hillebrands

Currently, spin wave (SW) based logic networks are widely discussed due to their potential as a CMOS complementary or even subsequent technology with extended functionality and improved performance [1, 2]. The advantages arise from the possibility to use the SW phase as an additional degree of freedom, to utilize interference effects and to reduce the size of devices. In combination with chargeless information transport and the consequent absence of ohmic losses, it allows for the realization of innovative and energy efficient information processing. Here, we explore 2D magnonic devices employing the phenomenon of spin-wave caustics [3–5]. These specific SW beams, which concentrate and direct energy of a huge number of plane spin waves with different wave vectors, can occur in in-plane magnetized magnetic films due to the anisotropic nature of the dipole-dipole interaction. Their excitation by opening of a 1D waveguide into 2D media has been shown in different magnetic materials [3, 4]. These beams feature outstanding peculiarities like sub-wavelength narrow apertures and they exhibit a strong dependency on the frequency and the direction of the external magnetic field.

After micromagnetic studies of the tractability of the SW caustic beams by current controlled inhomogeneities of the external field, we exploit the results to design a dynamically switchable SW signal splitter, a pivotal element for magnon-based networks.
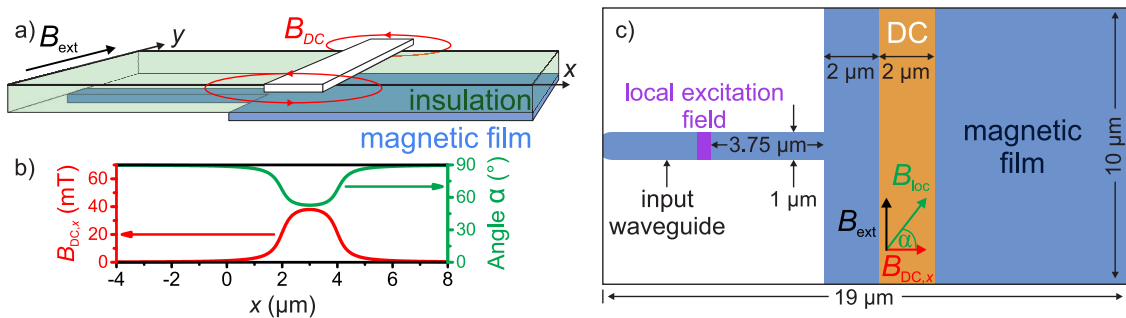
Fig. 1: Sketch of the simulated structure. a) Magnetic film with adjacent input waveguide separated from an overlaying DC-microstrip by an insulation layer. b) In-plane component $B_{DC,x}$ of the consequent magnetic field at the position of the magnetic layer in case of a DC-current of $I_{DC} = -100$ mA. This field component leads to an in-plane tilt of the local field B_{loc} by an angle of α. The upper curve shows the resulting angle in case of an external field of $B_{ext} = 50$ mT. c) Top view of the simulated magnetic structure with dimensions. The positions of the overlaying DC-microstrip and the local excitation field are depicted by the shaded areas.

The basic concept of the studied structure to create SW caustics and to control them by an inhomogeneous external field is depicted in Fig. 1. A 1 µm wide and 30 nm thick SW waveguide is connected to an unpatterned magnetic film of the same thickness. The film is tangentially magnetized by the external bias field $B_{ext} = 50$ mT applied perpendicular to the long axis of the input waveguide. A 2 µm wide and 150 nm thick current conducting microstrip is placed 300 nm above the film. The microstrip is separated from the film by an insulation layer. Passing a DC-current I_{DC} thought this microstrip leads to the creation of a localized Oersted magnetic field B_{DC}.

Figure 1b shows the in-plane component $B_{DC,x}$ in the unpatterned magnetic film, calculated according to Biot-Savart's law for $I_{DC} = -100$ mA. This field component causes an in-plane tilt of

the total local field B_{loc} by an angle of α relative to the y-axis, which is shown in the same graph. In the micromagnetic simulation, only the magnetic layer as shown in Fig. 1c is implemented together with the homogeneous external field B_{ext}, and both components $B_{\mathrm{DC,x}}$ and $B_{\mathrm{DC,z}}$ of the DC-Oersted field. The material parameters of the magnetic layer are chosen as for Permalloy ($\mathrm{Ni_{81}Fe_{19}}$: saturation magnetization $M_{\mathrm{S}} = 810$ kA/m, exchange constant $A_{\mathrm{ex}} = 13$ pJ/m, Gilbert damping constant $\alpha = 8 \cdot 10^{-3}$) since this is a widely used material, which is easy to deposit and to structure by conventional methods. The dimensions of the design and the parameters of the applied fields and currents as described above are chosen in such a way to ensure the realizability of the finally presented device. The micromagnetic simulation was carried out by utilizing the open-source GPU-accelerated simulation program MuMax3 [6]. The 19 µm long, 10 µm wide and 30 nm high magnetic structure was discretized into 1900 x 1000 x 1 cells with a size of 10 nm x 10 nm x 30 nm. This cell size ensures that in-plane wavevectors of the spin waves up to approximately $0.1\pi\,\mathrm{rad/nm}$ can be resolved. To ensure that no reflections of SW energy along the x-axis can occur, the SW damping at the vertical boundaries in Fig. 1c is increased incrementally in 25 steps over a distance of 0.5 µm to a value of $\alpha = 0.5$. No special boundary conditions are applied to the horizontal magnetic boundaries.

After calculating the ground state of the magnetization distribution, a microwave magnetic field localized on the distance of 0.5 µm in the middle of the input waveguide (see Fig. 1c) is used to excite spin waves. This field represents an input of a magnonic network. The amplitude of this field, which is acting only in x-direction, has been set to 10 mT. The field oscillates at 7 GHz, leading to the maximal SW excitation at the same frequency. To evaluate the simulation, the magnetization distribution is saved every 25 ps for a duration of 10 ns after applying the excitation field. This data is Fourier transformed in time to access the frequency dependent distribution of the SW intensity. In the following paragraphs the SW intensity distributions are shown integrated over the frequency interval from 6.75 GHz to 7.25 GHz.

Figure 2a shows the result of the simulation without any DC-current applied to the microstrip. It can clearly be seen that the SW energy splits in two caustic beams at the opening of the 1D input waveguide into the 2D magnetic film area. This simulation reproduces the experimental observations demonstrated in [3, 4]. The caustic creation is explained by the broad angular spectrum of SW wavevectors originating from the waveguide opening in combination with the anisotropic SW dispersion relation. Due to this dipolar induced anisotropy, the SW group velocity features two specific caustic angles θ_{C} with respect to the local magnetization direction. Since the local field and, accordingly, the magnetization distribution inside the film are homogeneous, the caustic angles do not change and the beams propagate in straight lines under an angle of $\theta_{\mathrm{C1}} = 75°$, respectively $\theta_{\mathrm{C2}} = 105°$, with respect to the y-axis.

The situation completely changes if a DC-current is applied that forces the local field and consequently the magnetization to tilt locally, as exemplarily shown in Fig. 2b for $I_{\mathrm{DC}} = -100$ mA. The inhomogeneous magnetization leads to a curvilinear propagation of the caustic beams since the anisotropy axes of the SW dispersion are rotated together with the local magnetization. This simulation clearly demonstrates the steering effect of SW caustics by an externally controlled inhomogeneity of the bias magnetic field.

The curvilinear caustic propagation results in an offset of the SW beams from its initial path. The offset Δy, which is defined as the distance of the intensity maxima with and without a DC-current, is studied at the position $x = 5$ µm in dependence on an applied, negative current I_{DC}. As can be seen in Figure 2c, the increased offset caused by the rising DC-current I_{DC} is accompanied with a change in the caustic intensities. These changes can be related to the contraction of the propagation
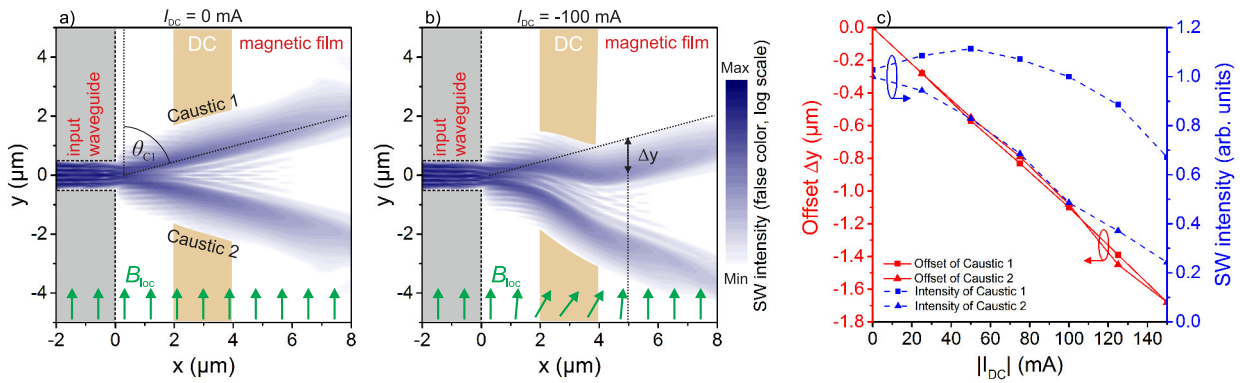
Fig. 2: Results of the micromagnetic simulations. a) SW caustics are created by opening the 1D input wave-guide into the 2D magnetic film. Without a DC-current applied to the microstrip, the external field is homogeneous and a straight propagation of the SW beams with an angle of $\theta_{C1} = 75°$, respectively $\theta_{C2} = 105°$, with respect to the y-axis can be observed. b) Curvilinear beam propagation of the SW caustics due to an inhomogeneous magnetization distribution generated by the applied DC-current of $I_{DC} = -100$ mA due to the resulting non-homogeneous local field. This leads to an offset Δy. c) Offset Δy and maximal intensity of the SW caustics at the position $x = 5$ µm as function of an applied, negative DC-current I_{DC}.

distance of the upper caustic between 20 mA and 80 mA and to the extension of the propagation distance of both caustic beams until the evaluation point is reached.

In the next step, the intrinsic splitting of SW energy in the process of caustic creation and the studied tractability of the beam directions are used to design a switchable SW splitter. This device combines two important functionalities needed to realize a magnonic network, namely the splitting of a SW signal enabling parallel data processing and its guidance through the network by controlled toggling between different waveguides. For this, in addition to the input waveguide and the adjacent unpatterned film, output waveguides are added to the structure at the position $x = 4$ µm (see Fig. 3). The transition zones between the magnetic film and these output waveguides are specially tailored to realize an efficient channeling of SW energy to the output waveguides at a DC-current of $I_{DC} = \pm 100$ mA. This value of the DC-current is chosen in accordance with the previous investigations to reach a sufficient offset of the caustic beams without serious loss in the SW intensities. All other parameters of the simulation are equivalent to those mentioned above.

Figure 3 shows the resulting distribution of the SW intensity for three different values of the DC-current I_{DC}, namely -100 mA, $+100$ mA and 0 mA. In Fig. 3a, a negative current leads to the bending of the caustic beams towards the negative y-direction, what results in a channeling of the SW intensity into the middle and bottom output waveguides. If the direction of the DC-current is changed, the SW beams bend into the opposite direction and a channeling of SW energy into the middle and the upper output waveguide occurs, as can be seen in Fig. 3b. After the splitting and switching processes, the SWs are channeled inside the specified output waveguides and subsequent magnonic devices could be selected and delivered with spin waves. For instance, Mach-Zehnder-type interferometers with different functionalities [2] could follow and perform data processing operations by interference of spin waves propagating through the middle and one of the outer waveguides. By applying the appropriate DC-current to the presented switchable splitter, the interferometer with the desired functionality can be selected.

In addition to the channeling of the SW into selected output waveguides, a further functionality arises if no DC-current is applied. This case is shown in Fig. 3c and reveals a blocking of the incoming SW energy for $I_{DC} = 0$ mA. Hence, the presented device also includes a gate function.
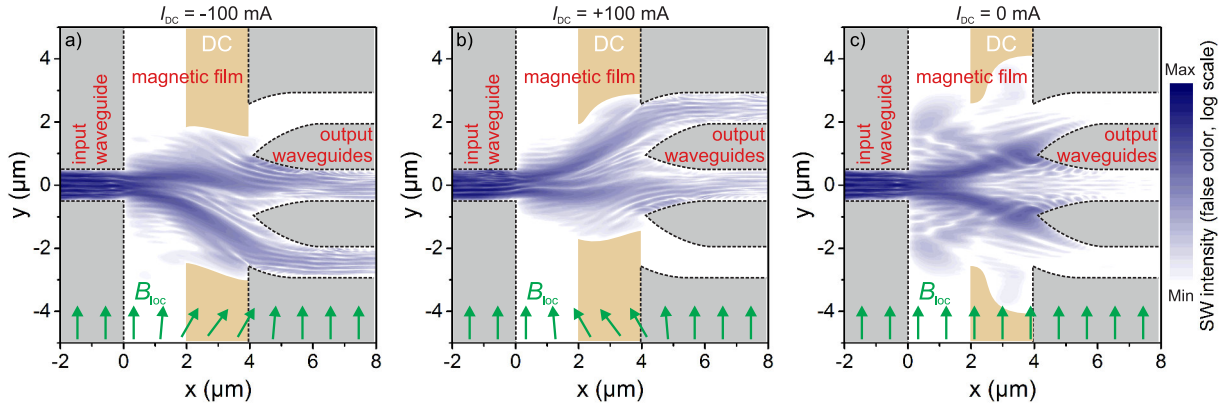
Fig. 3: Design of a switchable SW signal splitter based on SW caustics and its curvilinear propagation in inhomogeneous magnetized films. a) and b) Channeling of SW energy into different output waveguides depending on the applied DC-current. c) Suppression of the output signal, if no DC-current is applied.

In summary, we reveal by micromagnetic simulations a particular role which non-diffractive SW caustic beams propagating in unstructured magnetic films can play in the emerging field of magnonics. We have demonstrated the ability of the local manipulation of the SW caustic direction by an inhomogeneous magnetization distribution and its dynamic controllability by locally applied magnetic fields. Based on these results, such essential element for magnonic networks as a switchable SW signal splitter was developed. The presented design of the device makes it possible to channel SW into different output waveguides or to block them depending on the applied DC-current.

References

[1] A.V. Chumak, V.I. Vasyuchka, A.A. Serga, and B. Hillebrands, *Magnon spintronics*, Nat. Phys. **11**, 453 (2015).

[2] A. Khitun, M. Bao, and K.L. Wang, *Magnonic logic circuits*, J. Phys. D: Appl. Phys. **43**, 264005 (2010).

[3] T. Schneider, A.A. Serga, A.V. Chumak, C.W. Sandweg, S. Trudel, S. Wolff, M.P. Kostylev, V.S. Tiberkevich, A.N. Slavin, and B. Hillebrands, *Nondiffractive subwavelength wave beams in a medium with externally controlled anisotropy*, Phys. Rev. Lett. **104**, 197203 (2010).

[4] V.E. Demidov, S.O. Demokritov, D. Birt, B. O'Gorman, M. Tsoi, and X. Li, *Radiation of spin waves from the open end of a microscopic magnetic-film waveguide*, Phys. Rev. B **80**, 014429 (2009).

[5] T. Sebastian, T. Brächer, P. Pirro, A.A. Serga, B. Hillebrands, T. Kubota, H. Naganuma, M. Oogane, and Y. Ando, *Nonlinear emission of spin-wave caustics from an edge mode of a microstructured $Co_2Mn_{0.6}Fe_{0.4}Si$ waveguide*, Phys. Rev. Lett. **110**, 067201 (2013).

[6] A. Vansteenkiste, J. Leliaert, M. Dvornik, M. Helsen, F. Garcia-Sanchez, and B. Van Waeyenberge, *The design and verification of MuMax3*, AIP Advances **4**, 107133 (2014).

D.   Spin Caloric Transport

Spin Caloric Transport is a field of spintronics, which investigates the interplay between spin- and heat-based transport phenomena. The observation of the spin Seebeck effect (SSE) in a magnetic insulator demonstrates the crucial role of collective magnetization excitations, i.e. spin waves and their quanta, magnons, in spin caloric transport processes, and illustrates the conceptual distinction between this phenomenon and conventional thermoelectric generation. Most interesting and important is the conversion of a heat gradient into a magnon current and, vice versa, in a magnetic insulator. On a long time scale this may lead to the utilization of heat currents to support the transfer and processing of spin information.

In Report 4.12 we demonstrate the frequency dependence of the spin Seebeck effect in YIG/Pt bilayers and we present the identified characteristic response time which depends on the thickness of the YIG layer. Specifically, we find that the characteristic response time scales approximately as the inverse thickness of the magnetic films. This is consistent with recent experimental and theoretical studies and supports the notion that high-frequency magnons dominate the spin Seebeck effect in thin films but are less important for its absolute magnitude and frequency dependence in thicker ones.

Report 4.13 addresses the experimental observation of magnetization auto-oscillations in the YIG layer of a microstructured YIG/Pt nanowire driven by dc pulses applied to the Pt layer. Time-resolved Brillouin light scattering microscopy was used to display the temporal evolution and spatial distribution of the excited magnetization dynamics in the microstructure. The spin Seebeck effect has been identified as the driving force behind the auto-oscillations. The presented results are of interest, since they suggest the generation of a coherent precession state from incoherent SSE-injected magnons.

D.   Spin-kalorischer Transport

Der spin-kalorische Transport ist ein Forschungsfeld innerhalb der Spintronik, welches das Zusammenspiel zwischen spin- und wärmebasierten Transportphänomenen untersucht. Die Untersuchungen des Spin-Seebeck-Effekts (SSE) in magnetischen Isolatoren zeigen dabei die wichtige Rolle auf, welche die kollektiven Anregungen des magnetischen Systems - also Spinwellen und deren Quanten, die Magnonen - in spin-kalorischen Transportprozessen spielen. Weiterhin verdeutlichen diese Beobachtungen die konzeptuelle Unterscheidung zwischen diesen Phänomenen auf der einen sowie den konventionellen thermoelektrischen Effekten auf der anderen Seite. Von größtem Interesse und von größter Wichtigkeit in diesem Forschungsgebiet ist die Untersuchung der Umwandlung von Temperaturgradienten in reine Spinströme in Isolatoren. Perspektivisch kann das Verständnis dieser Prozesse zur Nutzung von Wärmeströmen für den Transport sowie die Verarbeitung von Spin-Information beitragen.

Im Bericht 4.12 demonstrieren wir die Frequenzabhängigkeit des Spin-Seebeck-Effekts in YIG/Pt-Zweischichtsystemen und präsentieren die ermittelten charakteristischen Reaktionszeiten welche abhängig von der YIG-Schichtdicke sind. Insbesondere zeigen wir, dass die charakteristische Reaktionszeit, näherungsweise mit der inversen Dicke des magnetischen Films skaliert. Dies ist konsistent mit kürzlich durchgeführten experimentellen und theoretischen Untersuchungen und bekräftigt die Auffassung, dass hochfrequente Magnonen den Spin-Seebeck-Effekt in dünnen Fil-

men dominieren aber weniger wichtig für seine absolute Größenordnung und die Frequenzabhängigkeit in dickeren Filmen sind.

Bericht 4.13 befasst sich mit den experimentellen Beobachtungen von Magnetisierungsoszillationen in der YIG-Schicht eines mikrostrukturierten YIG/Pt-Nanodrahtes, welcher von einem Gleichspannungspuls getrieben wird, der auf die Pt-Schicht gegeben wird. Es wurde die zeitaufgelöste Brillouin-Lichtstreuungs-Mikroskopie eingesetzt um die zeitliche Entwicklung und die räumliche Verteilung der angeregten Magnetisierungsdynamik in der Mikrostruktur sichtbar zu machen. Der Spin-Seebeck-Effekt wurde hierbei als die treibende Kraft hinter den Auto-Oszillationen identifiziert. Die präsentierten Resultate sind von großem Interesse, da sie auf die Erzeugung eines kohärenten Präzessionszustandes aus inkohärenten SSE-injizierten Magnonen hinweist.

4.12 Frequency-resolved investigation of the longitudinal spin Seebeck effect

T. Noack, T. Langner, A.A. Serga, B. Hillebrands, and V.I. Vasyuchka

In collaboration with M. Schreier[†], F. Kramer[†*], H. Huebl[*], S. Geprägs[*], R. Gross[†*], and S.T.B. Goennenwein[*]*
[†]*Physik-Department, Technische Universität München, Garching, Germany*
[*]*Walther-Meißner-Institut, Bayerische Akademie der Wissenschaften, Garching, Germany*

Angular momentum currents have been proposed as an alternative to charge currents for the implementation of logic devices and effective magnetization control at the nanometer scale. One possibility to generate these so-called pure spin currents is by stimulating magnetization dynamics in a ferromagnet, for example by creation of a thermal nonequilibrium at the interface between the ferromagnet and the spin sink (spin Seebeck effect [1]). At the present time the detailed microscopic mechanism responsible for the spin Seebeck effect is still vividly discussed. Experiments showed that the effect is nontrivially connected to the saturation and sublattice magnetization of the magnetically ordered material. The effective temperature of the magnons, which are deemed responsible for the effect, is very close to that of the phonons. Two independent studies recently attempted to quantify the time scale for the magnon-phonon coupling relevant for the spin Seebeck effect. Unfortunately the results of these experiments on yttrium iron garnet (YIG)/Pt samples were not conclusive. On the one hand, Agrawal et al. [2] observed a rolloff of the spin Seebeck voltage at frequencies below $1\,\mathrm{MHz}$ in a several-micrometer-thick film and attributed it to a finite "effective thermal magnon diffusion length". On the other hand, the experiments by Roschewsky et al. [3] in much thinner YIG films suggest that the spin Seebeck effect should be robust even beyond several tens of megahertz. We here resolve this apparent disagreement by performing systematic time-resolved spin Seebeck effect experiments on a series of samples with YIG thicknesses $50\,\mathrm{nm} \leq d_{\mathrm{YIG}} \leq 53\,\mu\mathrm{m}$. Two different experimental approaches were employed to investigate the spin Seebeck effect dynamics. At TU Kaiserslautern (UNI KL) a modulated microwave signal was used to heat the Pt layer which leads to the generation of a time varying thermal gradient across the YIG/Pt interface (Fig. 1a). At the Walther-Meißner-Institut (WMI) a continuous-wave solid-state laser is modulated to generate a sinusoidal intensity modulation of the laser beam for the heating. The time-varying spin Seebeck voltage is detected and averaged by a spectrum analyzer in both experimental approaches. More detailed information about the used setups can be found in Ref. [4].

The transfer functions $|V_{\mathrm{SSE}}|(f)$ for samples YIG(50 nm), YIG(270 nm), YIG(2.8 μm), YIG(6.7 μm) and YIG(30 μm) are exemplarily shown in Fig. 1b. The data have been normalized to the respective dc value for each sample for clarity. Evidently, the spin Seebeck voltage on the 50 nm film remains at its dc level up to much higher frequencies as compared to the other samples. Moreover, the voltage response for frequencies above the 3 dB point is markedly different for the different samples. For the 50 nm and 270 nm films the transfer function resembles a classical first order low-pass, decaying as $1/f$ for $f \gg f_{3\,\mathrm{dB}}$. In contrast, $|V_{\mathrm{SSE}}|(f)$ measured for the 2.8, 6.7, and 30 μm film decays at a much lower rate. Since the transfer functions of the investigated samples clearly cannot all be modeled with the same approach, we determine the cutoff (3 dB) frequencies

This work has been recently published in Physical Review B [4].
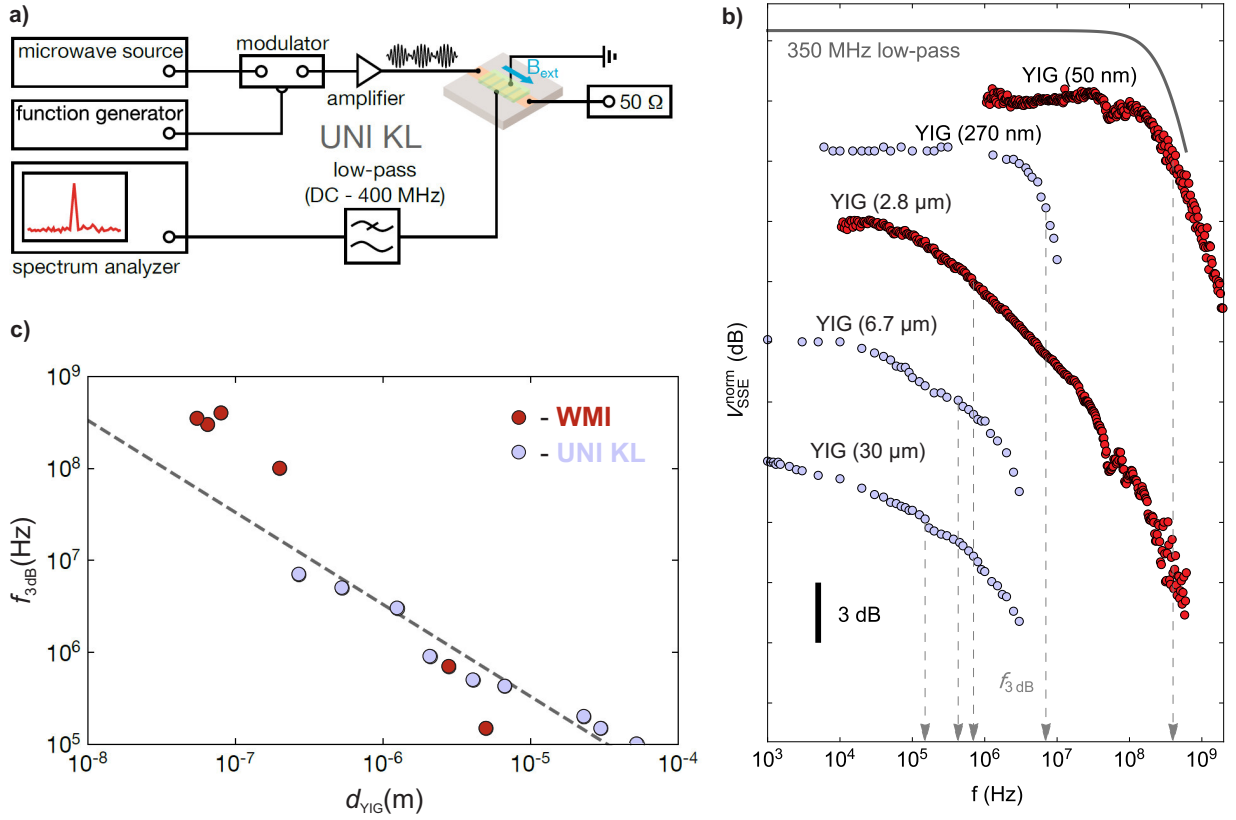
Fig. 1: a) Experimental setup used at UNI KL. b) Obtained transfer functions for different YIG-thicknesses. Light curves were measured at UNI KL, dark curves at the WMI. c) Selected cutoff frequencies $f_{3\,\mathrm{dB}}$ for all investigated samples.

$f_{3\,\mathrm{dB}}$ for all samples solely by the frequency at which $V_{\mathrm{SSE}}(f_{3\,\mathrm{dB}}) = V_{\mathrm{SSE}}(f \to 0)/\sqrt{2}$. The result is plotted in Fig. 1c and indicates a power-law like behavior of the cutoff frequency $f_{3\,\mathrm{dB}} \propto d^{\beta}$ as a function of the YIG film thickness d with an exponent $\beta \simeq -1$. The larger $f_{3\,\mathrm{dB}}$ values for the thinnest films can be attributed to the more pronounced magnetization damping in samples grown by pulsed laser deposition compared to films fabricated via liquid phase epitaxy.

Within the spin mixing interface conductance formalism an energy imbalance between the two sides of a ferromagnet/normal metal interface leads to the flow of angular momentum across the interface. For the spin Seebeck effect this energy difference may be formulated in terms of a temperature difference between electrons in the normal metal and magnons in the ferromagnet. While data at elevated temperatures are sparse, low-temperature measurements and the relatively long lifetime of the small-wave number k magnons even at room temperature suggest that the thermalization process between magnons and phonons is the limiting factor for high frequency spin Seebeck excitations. The interaction with the other thermal reservoir, the electrons in the normal metal, can be assumed instantaneous in the experimentally accessed frequency range as spin current emission has been demonstrated for much higher frequencies, e.g., in spin pumping or spin Hall magnetoresistance experiments.

To understand the observed frequency dependence of the spin Seebeck voltage we start from a steady-state model. The energy supplied to the Pt layer by the heating raises the temperature of the Pt layer (electrons and phonons are approximately in thermal equilibrium due to the fast electron-phonon scattering). Energy and angular momentum are then transferred by the spin transfer torque

from the electrons in the Pt to the magnons in the YIG, raising the magnon temperature T_m. Due to magnon-phonon scattering the energy is finally transferred to the phonon system and the heat sink. In the stationary situation a steady-state spin current is generated across the YIG/Pt interface which is proportional to the temperature difference $\Delta T = T_e - T_m$ of the electrons in Pt and the magnons in YIG. It is obvious that a finite ΔT and, hence, a finite spin Seebeck voltage is obtained only if the magnons couple to the phonons. This means a finite ΔT is obtained only on time scales longer than the characteristic magnon-phonon interaction time τ_{mp} in YIG. On shorter time scales, the energy cannot be transferred from the magnon to the phonon systems, resulting in $\Delta T \rightarrow 0$. In a simple relaxation time approach, the time evolution of the temperature difference ΔT_{mp} between the magnons and phonons in YIG can be expressed as:

$$\frac{d}{dt}\Delta T_{mp} = -\frac{\Delta T_{mp}}{\tau_{mp}} \quad . \tag{1}$$

This is trivially solved by $\Delta T_{mp}(t) \propto e^{-\frac{t}{\tau_{mp}}}$, which transforms to

$$|\Delta T_{mp}(\omega)| \propto \frac{1}{\sqrt{1+(\omega\tau_{mp})^2}} \quad , \tag{2}$$

in the frequency domain [5]. The transfer function derived from this model describes the data of the 50 and 270 nm films reasonably well. Following this reasoning the cutoff frequency in the 50 nm film thus corresponds to a characteristic interaction time between magnons and phonons of $\tau_{mp} = 1/(2f_{3\,dB}) \approx 450\,ps$. This is consistent with estimates in the literature which put τ_{mp} at a few hundred picoseconds for high-energy magnons [6]. In the simple relaxation time approach with a single, frequency independent relaxation time the extracted τ_{mp} likely is a weighted average over the entire magnon spectrum contributing to the emission of the measured spin current. Keeping in mind that τ_{mp} rather is frequency dependent further explains why the transfer function for the thicker films deviates significantly from Eq. (2). In thermal equilibrium and in the absence of any spatial variation of the temperature, the magnon population is distributed according to Bose-Einstein statistics and can be described with a single magnon temperature T_m. A thermal gradient is accompanied by a flow of magnons along the same direction, with the diffusion length of individual magnons decreasing with their energy. The different diffusion lengths become important at the edges (interfaces) of the magnetic layer at which only magnons closer than their respective diffusion length can accumulate. Increasing the magnetic layer thickness then favors lower energetic magnons with their longer diffusion lengths in the interface accumulation. This also implies that increasing the thickness of the ferromagnet leads to a growing deviation from Bose-Einstein statistics right at the interface, and the concept of a single temperature is no longer well defined. According to numerical simulations this effect is small for our thinnest films but should be more significant in thicker ones. At any rate, the magnon spectrum is expected to show an exponential relaxation, similarly to Eq. (1). The lowest energetic magnons feature interaction times with phonons exceeding a microsecond, and one would indeed expect the effective cutoff frequency to shift to lower values in thicker YIG films. More specifically, Etesami et al. [7] derived the functional dependence of the 3 dB roll-off frequency $f_{3\,dB}$ for a given magnon mode $n \in N_0$ on d_{YIG} as

$$f_{3dB}^n = \alpha\frac{\gamma}{2\pi}\left[B_0 + \frac{2A}{M_S}\left(\frac{n\pi}{d_{YIG}}\right)^2\right] \quad , \tag{3}$$

where α is the magnetization damping, γ is the gyromagnetic ratio, B_0 is the external magnetic field, A is the exchange constant, and M_{s} is the saturation magnetization. The full transfer function is a linear combination of the low-pass behavior of the individual magnon modes. As d_{YIG} increases, the mode number n for magnons, still effective at a given energy, increases and more lower energetic modes become available. Since these lower energetic modes feature smaller $f_{3\,\text{dB}}$ values the total $f_{3\,\text{dB}}$ shifts downwards, at a rate determined by the mode occupation number, i.e. the composition of the magnon spectrum. The d_{YIG}^{-1} behavior observed in Fig. 1c is qualitatively consistent with an increased weight of the lower energetic end of the magnon spectrum in thicker films. In any case, the $f_{3\,\text{dB}}$ values plotted in Fig. 1c may be understood as approximate values of the dominant magnon mode. Finally $f_{3\,\text{dB}}$ is related to the characteristic magnon energy stimulating the spin current emission via

$$ E = \hbar\omega = \frac{2\pi\hbar}{\alpha} f_{3\,\text{dB}} \quad . \tag{4} $$

The extracted values appear to be consistent with the literature and are further supported by the $f_{3\,\text{dB}}(500\,\text{nm})$ value of some $10\,\text{MHz}$ inferred from numerical simulations in Ref. [7].

In summary, we investigated the frequency dependence of the spin Seebeck effect and identified characteristic response times which depend on the thickness of the YIG layer. Specifically we find that the characteristic response time scales approximately as the inverse thickness of the films. This is consistent with recent experimental and theoretical studies and supports the notion that high-frequency magnons dominate the effect in thin films but are less important for its absolute magnitude and frequency dependence in thicker ones. Going beyond the scope of the experiments presented here, further insights might be gained by systematically studying the effect of large magnetic fields and low temperatures on the dynamics. Large magnetic fields have already been demonstrated to affect the dc properties, an effect which should also translate to the transient response. The approach presented here could also provide further insight into the spectral composition of the thermally induced spin currents in compensated garnets with nontrivial contributions from different magnetic sublattices.

References

[1] K. Uchida, S. Takahashi, K. Harii, J. Ieda, W. Koshibae, K. Ando, S. Maekawa, E. Saitoh, *Observation of the spin Seebeck effect*, Nature **455**, 778-781 (2008).

[2] M. Agrawal, V.I. Vasyuchka, A.A. Serga, A.D. Karenowska, G.A. Melkov, B. Hillebrands, *Direct measurement of magnon temperature: New insight into magnon-phonon coupling in magnetic insulators*, Phys. Rev. Lett. **111**, 107204 (2013).

[3] N. Roschewsky, M. Schreier, A. Kamra, F. Schade, K. Ganzhorn, S. Meyer, H. Huebl, S. Geprägs, R. Gross, S.T.B. Goennenwein, *Time resolved spin Seebeck effect experiments*, Appl. Phys. Lett. **104**, 202410 (2014).

[4] M. Schreier, F. Kramer, H. Huebl, S. Geprägs, R. Gross, S.T.B. Goennenwein, T. Noack, T. Langner, A.A. Serga, B. Hillebrands, V.I. Vasyuchka, *Spin Seebeck effect at microwave frequencies*, Phys. Rev. B **93**, 224430 (2016).

[5] D.J. Sanders, D. Walton, *Effect of magnon-phonon thermal relaxation on heat transport by magnons*, Phys. Rev. B **15**, 1489 (1977).

[6] M. Schreier, A. Kamra, M. Weiler, J. Xiao, G.E.W. Bauer, R. Gross, S.T.B. Goennenwein, *Magnon, phonon, and electron temperature profiles and the spin Seebeck effect in magnetic insulator/normal metal hybrid structures*, Phys. Rev. B **88**, 094410 (2013).

[7] S.R. Etesami, L. Chotorlishvili, J. Berakdar, *Spectral characteristics of time resolved magnonic spin Seebeck effect* Appl. Phys. Lett. **107**, 132402 (2015).

4.13   Auto-oscillations in YIG/Pt nanostructures due to a thermal gradient

V. Lauer, M. Schneider, T. Meyer, P. Pirro, F. Heussner, B. Lägel, V. Vasyuchka, A.A. Serga, B. Hillebrands, and A.V. Chumak

In collaboration with C. Dubs and O. Surzhenko, INNOVENT e.V., Technologie-entwicklung, Prüssingstraße 27B, 07745 Jena, Germany.

Spin-transfer torque (STT) [1] caused by the injection of spin-polarized electron currents into magnetic structures has attracted attention due to the potential realization of efficient microwave sources [2] and magnonic components without spin-wave losses [3]. The generation of spin-polarized currents based on the spin Hall effect (SHE) [4] is of particular importance since it does not require a charge current to pass through the magnetic material, therefore, providing access to the application of STT to insulators such as yttrium iron garnet (YIG) [3, 5]. Partial compensation of the spin-wave damping [6, 7] and excitation of magnetization auto-oscillations [8, 9] in YIG/Pt bilayers by applying a dc current to the adjacent Pt layer were demonstrated recently. The spin Seebeck effect (SSE) [10] is another method of spin-current generation which utilizes a thermal gradient rather than a charge current. This phenomenon might be of particular practical benefit since it potentially does not require a separate energy source, but could use parasitic heat sources that already exist in the system. There have been experimental studies showing that the spin current due to heat gradients can apply a STT to a magnetic film resulting in the partial compensation of damping in YIG (as e.g. in Ref. [11]). Furthermore, first experimental evidences of SSE-excited magnetization precession in YIG/Pt nanowires at low temperatures investigated by means of electrical measurements have been recently reported [12].
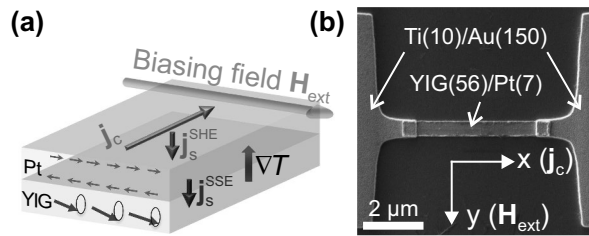
Fig. 1: a) Illustration of the spin current generated by the SHE and by the SSE (due to a temperature gradient) in a YIG/Pt bilayer, if a charge current is passed through the Pt layer. b) Image of a YIG/Pt nanowire connected to Ti/Au leads (length scale in the lower left-hand corner). The biasing field is along the y-direction, the charge current is along the x-direction.

In this Report, we show the experimental observation of magnetization auto-oscillations in the YIG layer of a YIG/Pt nanowire driven by dc pulses applied to the Pt layer. Time-resolved Brillouin light scattering (BLS) spectroscopy is used to investigate the temporal evolution and the spatial distribution of the excited magnetization dynamics in the nanostructure. The experimental results show that the spin Seebeck effect is the main driving force behind the auto-oscillations in the particular nanostructure shown in Fig. 1b. Joule heating by the current pulses leads to an increase in the Pt temperature, and, consequently, to the formation of a thermal gradient across the YIG/Pt interface. The thermal gradient gives rise to a SSE-induced spin current injected into the YIG layer which exerts an anti-damping torque on the magnetization and, eventually, excites magnetization precession. The influence of the SHE-induced spin current is detected as well, but plays only a minor role in our experiments. Figure 1a schematically shows the investigated YIG/Pt bilayer, indicating the directions of the externally applied biasing field $\mathbf{H}_{ext}$, the applied charge current density $\mathbf{j}_c$, the generated spin current density $\mathbf{j}_s^{SHE}$ due to the SHE, and the SSE-induced spin

current density $\mathbf{j}_s^{SSE}$ due to the thermal gradient ∇T.

Figure 1b shows the image of one of the investigated YIG/Pt nanowires and the Ti/Au structures (left and right) which are used as leads to apply dc pulses. The nanowire is 475 nm wide and the distance between the leads is 4 μm. The structures were fabricated by growing a YIG film of 66 nm thickness by means of liquid phase epitaxy on a gadolinium gallium garnet substrate [13]. Standard microwave-based ferromagnetic resonance (FMR) measurements yield a Gilbert damping parameter of $\alpha_{YIG} = 1.8 \times 10^{-4}$ for the bare YIG film. Next, plasma-assisted cleaning was used to remove potential contaminations before the sample was transferred into a molecular beam epitaxy (MBE) facility for the deposition of a 7 nm thick Pt layer on top of the YIG film. The deposited Pt layer was found to increase the Gilbert damping to $\alpha_{YIG/Pt} = 1.2 \times 10^{-3}$. The subsequent structuring of the YIG/Pt nanowires was achieved by electron-beam lithography and argon-ion milling. The leads (10 nm Ti and 150 nm Au) were patterned by using electron-beam lithography and vapor deposition.

For the BLS measurements, a laser beam with a wavelength of 491 nm and a power of 2 mW is focused onto the nanostructure. The laser-spot size is approximately 400 nm in diameter. An in-plane biasing field of $\mu_0 H_{ext} = 90$ mT is used to magnetize the nanowire perpendicular to its length (along the y-direction), and 50 ns long dc pulses with a repetition time of 500 ns are passed trough the nanowire (along the x-direction). Such a configuration allows for the injection of a pure spin current into the YIG layer due to two effects, the SSE and the SHE. The origin of the SSE is Joule heating of the Pt layer which creates a thermal gradient from the colder YIG to the hotter Pt. As a result, a pure spin current is injected into the YIG, and exerts an anti-damping spin torque. This SSE-induced spin torque, in particular, depends only on the thermal gradient regardless of the alignment between the magnetization orientation and the charge current direction. The situation is different for the SHE-generated spin current which reverses if the field polarity or the current direction is reversed. Thus, the SHE-driven STT can act as a damping or anti-damping torque, depending on the orientation of the magnetic field with respect to the charge current direction.
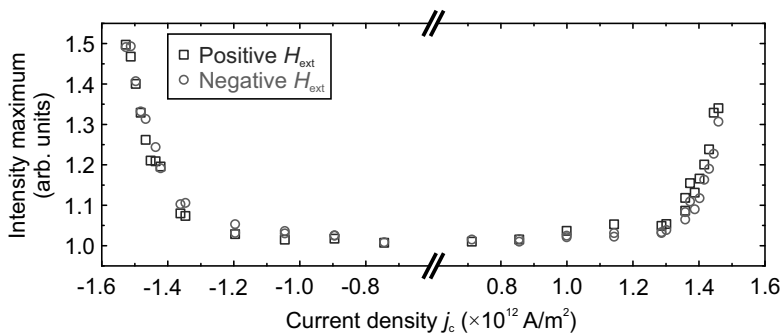
Fig. 2: BLS intensity maximum detected in the nanowire center during the applied dc pulse. The threshold-like onset of auto-oscillations is observed for both magnetic field polarities and both current directions.

Figure 2 shows the maximum BLS intensity measured in the center of the nanowire during the dc pulse as a function of the applied current for both field polarities and both current directions. It clearly reveals that the threshold-like onset of magnetization auto-oscillations for current densities higher than $|j_c| > 1.3 \times 10^{12}$ A/m^2 is independent of the field polarity. As already mentioned, this behavior can be understood by an anti-damping torque driven by the SSE, but cannot originate from the SHE. However, the data points in Fig. 2 demonstrate a weak influence of the SHE-STT on the spin dynamics in accordance with theoretical expectations: The measured maximum BLS intensity is higher in the case of the additional anti-damping SHE-STT (squares (circles) for $j_c > 0$ ($j_c < 0$) in Fig.2). From the experimental data, it can be estimated that the SHE shifts the critical current density for the SSE-generated auto-oscillations in the nanowire under investigation by only

1 %. The reason for the weak influence of the SHE in the nanowires, in contrast to Report 4.4, could be the relatively small spin-Hall angle due to the high quality Pt grown by means of MBE. It was recently reported that moderately dirty Pt layers grown by a sputtering technique yield up to 6 times larger spin-Hall angles compared to very clean growth processes [14].

Fig. 3: a) Gray-scaled BLS intensity as a function of the measured BLS frequency and time. The dashed lines illustrate the duration of the 50 ns long dc pulse. b) Temporal evolution of the BLS frequency of the intensity maximum. c) Temporal evolution of the BLS intensity integrated over all measured BLS frequencies.
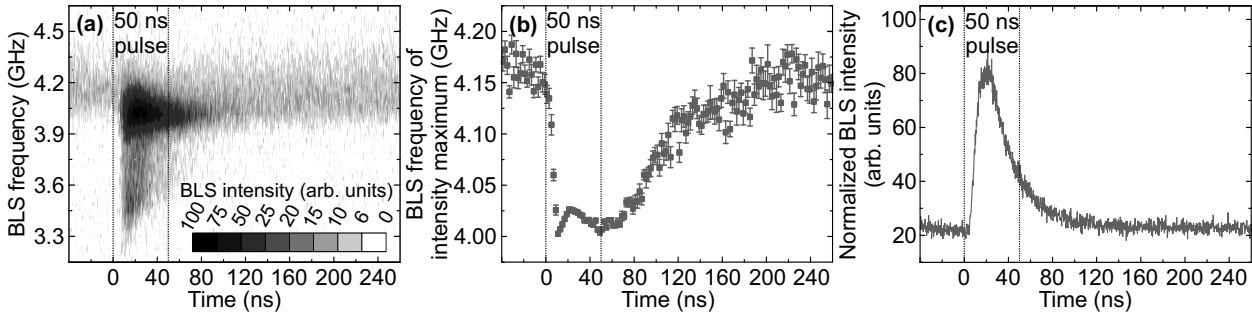
A main feature of the time-resolved BLS technique is the ability to investigate the temporal evolution of the SSE-generated auto-oscillations. In Fig. 2a the gray-scaled BLS-intensity is depicted as a function of the BLS frequency and time. Spin dynamics are excited during the applied dc pulse within the time frame of $0 < t < 50$ ns. Figure 3b shows the temporal behavior of the BLS frequency of the intensity maximum. Before the start of the dc pulse at $t < 0$ ns, the system is in equilibrium and thermal spin-waves are observed at a frequency of 4.15 GHz. The BLS frequency then drops to approximately 4 GHz when the dc pulse is applied. Comparable frequency drops have been reported for auto-oscillations excited by the SHE-STT [9]. After the pulse at $t > 50$ ns, the system slowly relaxes back to its original state. A remarkable feature of SSE-generated auto-oscillations becomes apparent by plotting the BLS intensity versus time, as shown in Fig. 3c. Here, the intensity is integrated over all detected BLS frequencies from 3.0 GHz to 5.2 GHz. The BLS intensity clearly reaches a maximum within the first 20 ns and starts to decay before the end of the pulse. We contribute this behavior to the temporal evolution of the thermal gradient in combination with the overall heating of the nanostructure under investigation. According to numerical simulations (not shown here) using COMSOL Multiphysics®, the thermal gradient in the YIG layer rapidly increases and saturates within a few nanoseconds and, therefore, the SSE saturates as well. The overall temperature of the system, in contrast, steadily increases during the whole duration of the pulse. The temperature increase is assumed to decrease the spin-mixing conductance of the YIG/Pt interface [15], and, therefore, the injected spin current drops and is accompanied by the reduction of the anti-damping torque. Such a drop of the BLS signal within the pulse duration (as shown in Fig. 3c) is observed for all tested current densities above the critical current density.

In order to display the spatial distribution of the auto-oscillations, a line scan along the nanowire (in *x*-direction) is performed. We detect the highest intensity in the center of the nanowire and observe an intensity drop close to the leads (measurement data not shown here). This finding can be understood by the assumption that the metallic leads are significant better heat sinks then the YIG layer. Therefore, the temperature increase of the Pt layer is smaller closer to the leads, and thus, also the thermal gradient at the YIG/Pt interface and the corresponding anti-damping torque is smaller close to the leads. We believe that this is the reason why SSE-driven auto-oscillations

were not observed in YIG/Pt microstructures widely covered by heat absorbing leads, as it is e.g. the case in Report 4.4 and in the experiments of Refs. [8, 9].

In conclusion, we demonstrate the generation of magnetization auto-oscillations in a YIG/Pt nanowire due to a thermal gradient. The SSE was identified as the origin for the anti-damping torque in the presented measurements. We observed a frequency drop of several hundred MHz during the excitation of spin dynamics. The temporal behavior of the BLS intensity, in particular the observation of a maximum followed by a decay within the dc pulse duration, could be attributed to the temporal behavior of the thermal gradient and the overall temperature increase in the system. This assumption is supported by the results of numerical simulations. These findings are of great interest since they suggest the generation of a coherent precession state from incoherent SSE-injected magnons and reveal an application potential for the realization of microwave sources at room temperature.

References

[1] J.C. Slonczewski, *Current-driven excitation of magnetic multilayers*, J. Magn. Magn. Mater. **159**, L1-L7 (1996).

[2] A.N. Slavin, V.S. Tiberkevich, *Nonlinear auto-oscillator theory of microwave generation by spin-polarized current*, IEEE Trans. Magn. **45**, 1875-1918 (2009).

[3] A.V. Chumak, V.I. Vasyuchka, A.A. Serga, B. Hillebrands, *Magnon spintronics*, Nature Phys. **11**, 453 (2015).

[4] J.E. Hirsch, *Spin Hall effect*, Phys. Rev. Lett. **83**, 1834 (1999).

[5] Y. Kajiwara, K. Harii, S. Takahashi, J. Ohe, K. Uchida, M. Mizuguchi, H. Umezawa, H. Kawai, K. Ando, K. Takanashi, S. Maekawa, E. Saitoh, *Transmission of electrical signals by spin-wave interconversion in a magnetic insulator*, Nature **464**, 262-266 (2010).

[6] A. Hamadeh, O. d'Allivy Kelly, C. Hahn, H. Meley, R. Bernard, A.H. Molpeceres, V.V. Naletov, M. Viret, A. Anane, V. Cros, S.O. Demokritov, J.L. Prieto, M. Muñoz, G. de Loubens, O. Klein, *Full control of the spin-wave damping in a magnetic insulator using spin-orbit torque*, Phys. Rev. Lett. **113**, 197203 (2014).

[7] V. Lauer, D.A. Bozhko, T. Brächer, P. Pirro, V.I. Vasyuchka, A.A. Serga, M.B. Jungfleisch, M. Agrawal, Yu.V. Kobljanskyj, G.A. Melkov, C. Dubs, B. Hillebrands, A.V. Chumak, *Spin-transfer torque based damping control of parametrically excited spin waves in a magnetic insulator*, Appl. Phys. Lett. **108**, 012402 (2016).

[8] M. Collet, X. de Milly, O. d'Allivy Kelly, V.V. Naletov, R. Bernard, P. Bortolotti, J. Ben Youssef, V.E. Demidov, S.O. Demokritov, J.L. Prieto, M. Muñoz, V. Cros, A. Anane, G. de Loubens, O. Klein, *Generation of coherent spin-wave modes in yttrium iron garnet microdiscs by spin-orbit torque*, Nat. Commun. **7**, 10377 (2016).

[9] V.E. Demidov, M. Evelt, V. Bessonov, S.O. Demokritov, J.L. Prieto, M. Muñoz, J. Ben Youssef, V.V. Naletov, G. de Loubens, O. Klein, M. Collet, P. Bortolotti, V. Cros, A. Anane, *Direct observation of dynamic modes excited in a magnetic insulator by pure spin current*, Sci. Rep. **6**, 32781 (2016).

[10] K. Uchida, H. Adachi, T. Ota, H. Nakayama, S. Maekawa, E. Saitoh, *Observation of longitudinal spin-Seebeck effect in magnetic insulators*, Appl. Phys. Lett. **97**, 172505 (2010).

[11] M.B. Jungfleisch, T. An, K. Ando, Y. Kajiwara, K. Uchida, V.I. Vasyuchka, A.V. Chumak, A.A. Serga, E. Saitoh, B. Hillebrands, *Heat-induced damping modification in yttrium iron garnet/platinum hetero-structures*, Appl. Phys. Lett. **102**, 062417 (2013).

[12] C. Safranski, I. Barsukov, H.K. Lee, T. Schneider, A.A. Jara, A. Smith, H. Chang, K. Lenz, J. Lindner, Y. Tserkovnyak, M. Wu, I.N. Krivorotov, *Spin caloritronic nano-oscillator*, arXiv:1611.00887 (2016).

[13] C. Dubs, O. Surzhenko, R. Linke, A. Danilewsky, U. Brückner, J. Dellith, *Sub-micrometer yttrium iron garnet LPE films with low ferromagnetic resonance losses*, arXiv:1608.08043 (2016).

[14] E. Sagasta, Y. Omori, M. Isasa, M. Gradhand, L.E. Hueso, Y. Niimi, Y. Otani, F. Casanova, *Tuning the spin Hall effect of Pt from the moderately dirty to the superclean regime*, Phys. Rev. B **94**, 060412(R) (2016).

[15] K. Uchida, T. Kikkawa, A. Miura, J. Shiomi, E. Saitoh, *Quantitative temperature dependence of longitudinal spin Seebeck effect at high temperatures*, Phys. Rev. X **4**, 041023 (2014).

E.   New Materials and Heusler Compounds

Developing new materials as well as modifying already well-known materials in order to generate properties of interest is an important aspect in our research. In our group we focus on the application of these materials in magnon-spintronic devices. The samples are mostly made vias national and international collaboration, involving a strong student exchange. The material class of Heusler compounds contains several promising candidates regarding their utilization in the field of *spintronics* and in particular of *magnon spintronics*. The major reasons for the interest in Heusler compounds are their high Curie temperature, their high spin polarization, and their low magnetic Gilbert damping. Heusler compounds have the general composition X_2YZ or XYZ, where X and Y are transition metals, and Z is an element of the main groups III-V. One of the most promising classes of Heusler materials is given by the cobalt-based compounds with the composition Co_2YZ. This class shows high spin polarization as well as the low Gilbert damping. The reason for both is the half-metallic character of Heusler compounds. Half metallicity describes the different features in the band structure of minority and majority electrons close to the Fermi energy. For the minority electrons, a band gap can be found at the Fermi energy. In contrast to this, the majority spin channel exhibits a finite density of states at the Fermi level and, thus, metallic character. Among the wide family of the Heusler compounds, the interest has been lately focused in candidates that exhibit a robust perpendicular magnetic anisotropy (PMA) together with the compatibility with standard tunneling barrier materials such as MgO or $MgAl_2O_4$.

In Report 4.14 we investigate a promising Heusler candidate, the compound material Co_2FeAl (CFA) with respect to the thickness ($7-80nm$) of the epitaxial films. This work is a part of the joint HEUMEM research project. The research initiative have addressed the development, the characterization, and the optimization of Heusler materials for the utilization in spintronics and magnon spintronics. In the report we present the dependence of the in-plane anisotropies and the Gilbert damping parameter on the thickness and the determination of the interface perpendicular anisotropy constant for the CFA/MgO interface. Negative value for the perpendicular anisotropy constant, minimum values for damping that reach the value of 3×10^{-3} and damping that increases with decreasing thickness were the main findings concerning this new type of the Heusler compound.

In Report 4.15 Heusler compounds have been also used as suitable materials for studies on spin-transfer torque induced spin-wave heating. A microstructured Heusler-Pt waveguide was used in the form $Co_2Mn_{0.6}Fe_{0.4}Si$ (CMFS) with a thickness of 5 nm. On top of the CMFS, a Pt layer of 2 nm thickness was deposited. We show that the effective spin wave damping in Heusler-Pt waveguides can be controlled in a wide range and can even be completely compensated in the case of short applied DC pulses. We find that the frequency shift is independent on the applied current, proving that Joule heating can be neglected. These results show that in any device using the spin transfer torque effect to generate or amplify spin waves, this source of heating needs to be taken into account.

In Report 4.16 we present another field where the request of new types of materials is necessary: the field of magneto-plasmonics. We propose that the use of magnetic materials in plasmonic structures can strongly modify the plasmonic and the magnetooptical properties of the samples. We show that periodically patterned ferromagnetic metal films can be seen as magneto-plasmonic meta-structures, whose magneto-optic response can be controlled by using the appropriate polarization and wavelength of the incident light. We reveal a strategy (correlation of near- and far-field effects) to design the magneto-optic response of a magnetoplasmonic material by acting on its op-

tical properties. Tuning the Kerr enhancement with the optical properties of plasmonic excitations introduces the concept of a magneto-plasmonic metastructure and opens new routes for tailoring the functionality of patterned magneto-plasmonic systems.

E.   Neue Materialien und Heusler-Legierungen

Sowohl die Entwicklung neuer als auch die Verbesserung bereits bekannter Materialien zur Untersuchung interessanter Materialeigenschaften ist ein wichtiger Aspekt unserer Forschung. In unserer Gruppe legen wir ein spezielles Augenmerk auf die Anwendung der Materialien in magneto-spintronische Devices. Die Proben werden dazu häufig über nationale und internationale Zusammenarbeit hergestellt. Hierzu gibt es einen intensiven Doktorandenaustausch. Die Gruppe der Heusler-Verbindungen enthält zahlreiche erfolgversprechende Kandidaten hinsichtlich der Nutzung im Bereich der Spintronik und insbesondere der Magnon-Spintronik. Die Hauptgründe für das Interesse an Heusler-Verbindungen sind ihre hohe Curie-Temperatur, ihre große Spinpolarisation sowie ihre geringe magnetische Gilbert-Dämpfung. Heusler-Verbindungen besitzen die allgemeine Zusammensetzung X_2YZ oder XYZ. Hierbei sind X und Y Übergangsmetalle, während Z ein Element der Hauptgruppen III-V ist. Eine der vielversprechendsten Untergruppen der Heusler-Materialien sind die Kobalt-basierten Verbindungen mit der Zusammensetzung Co_2YZ. Der Grund sowohl für die groSSe Spinpolarisation als auch für die geringe Gilbert-Dämpfung liegt im halbmetallischen Charakter der Heusler-Verbindungen. Dieser halbmetallische Charakter beschreibt die verschiedenen Eigenheiten der Bandstruktur von Minoritäts- und Majoritätselektronen nahe der Fermi-Kante. Für die Minoritätselektronen lässt sich eine Bandlücke an der Fermi-Kante beobachten, wohingegen die Bandstruktur der Majoritätselektronen dort eine endliche Zustandsdichte und somit metallischen Charakter aufweist. Innerhalb der groSSen Gruppe der Heusler-Verbindungen wurde das Hauptaugenmerk zuletzt auf solche Verbindungen gelegt, die eine starke senkrechte magnetische Anisotropie (PMA, perpendicular magnetic anisotropy) aufweisen und ebenfalls kompatibel sind mit üblichen Materialien für Tunnelbarrieren wie MgO oder $MgAl_2O_4$.

In Bericht 4.14 wird eine vielversprechende Heusler-Verbindung mit der Zusammensetzung Co_2FeAl (CFA) hinsichtlich der Dicke ($7-80nm$) der epitaktisch gewachsenen Schichten untersucht. Die vorliegende Arbeit ist Teil des gemeinsamen HEUMEM Forschungsprojekts. Dieses Projekt legt Wert auf die Entwicklung, die Charakterisierung und die Optimierung von Heusler-Verbindungen mit dem Ziel der Verwendung im Bereich der Spintronik und Magnon-Spintronik. In diesem Bericht wird erstens die Abhängigkeit der Anisotropie in der Ebene und des Gilbert-Dämpfungsparameters von der Dicke beschrieben und zweitens die Anisotropiekonstante senkrecht zur Grenzfläche CFA/MgO ermittelt. Die auffälligsten Befunde bezüglich dieser neuen Heusler-Verbindung waren negative Werte für die senkrechte Anisotropiekonstante, extrem kleine Werte für die Dämpfung (bis zu 3×10^{-3}) sowie ein Anstieg der Dämpfung bei Verringerung der Schichtdicke.

In Bericht 4.15 dienten Heusler-Verbindungen ebenfalls als Studienobjekte für Spin-Transfer-Torque-induzierte Erhitzung durch Spinwellen. Es wurde ein mikrostrukturierter Heusler-Platin-Wellenleiter der Zusammensetzung $Co_2Mn_{0.6}Fe_{0.4}Si$ (CMFS) mit einer Dicke von 5 nm verwendet. Auf das CMFS wurde eine Platinschicht von 2 nm Dicke abgeschieden. Es konnte gezeigt werden, dass die effektive Dämpfung der Spinwellen in Heusler-Platin-Wellenleitern in erheblichem MaSSe beeinflusst werden kann und dass im Fall des Einsatzes kurzer Gleichstromimpulse die Spinwellen sogar komplett aufgehoben werden können. Es wurde festgestellt, dass die Frequenzverschiebung unabhängig vom angelegten Strom ist, wodurch belegt wird, dass die Joulesche

Erwärmung vernachlässigbar ist. Diese Ergebnisse zeigen, dass bei einem Gerät, welches den Spin-Transfer-Torque ausnutzt, um Spinwellen zu erzeugen oder zu verstärken, diese Wärmequelle unbedingt berücksichtigt werden muss.

In Bericht 4.16 wird ein weiterer Bereich vorgestellt, in dem dringende Nachfrage nach neuartigen Materialen herrscht: Der Bereich der Magnetoplasmonik. Unsere Annahme ist, dass die Verwendung magnetischer Materialien in plasmonischen Strukturen die magnetooptischen Eigenschaften einer Probe stark beeinflussen kann. Es wird aufgezeigt, dass periodisch strukturierte ferromagnetische Metallschichten als magnetoplasmonische Metastrukturen aufgefasst werden können, deren magnetooptische Resonanz durch geeignete Polarisation und Wellenlänge des einfallenden Lichts gesteuert werden kann. Wir stellen eine Strategie vor (die Korrelation von Nahfeld- und Fernfeldeffekten), um die magnetooptische Resonanz eines magnetoplasmonischen Materials nach unseren Wünschen zu gestalten, indem wir seine optischen Eigenschaften verändern. Das Einstellen der Kerr-Verstärkung mit Hilfe der optischen Eigenschaften der plasmonischen Anregungen eröffnet die Möglichkeit einer magnetoplasmonischen Metastruktur und bietet viele Perspektiven, um die Funktionsvielfalt strukturierter magnetoplasmonischer Systeme den zukünftigen Anwendungen anzupassen.

4.14   Thickness dependent properties of the Heusler alloy Co$_2$FeAl

A. Conca, and B. Hillebrands

In collaboration with A. Niesen, G. Reiss, Center for Spinelectronic Materials and Devices, Physics Department, Bielefeld University, Germany.

For their use for efficient spin torque switching, materials with a certain set of properties are required. These properties are a combination of low damping and low magnetization, together with the presence of a robust perpendicular magnetic anisotropy (PMA). Additionally, these materials should show a high spin polarisation and compatibility with standard tunneling barrier materials such as MgO or MgAl$_2$O$_4$. A high Curie temperature is also desirable to guarantee temperature stability. In the wide family of the Heusler compounds, some candidates can be found which may fulfill this requirements.

In this Report we present a characterization of thin films of a promising candidate, the compound Co$_2$FeAl (CFA). A thickness series (7$-$80 nm) of epitaxial films was prepared by the University of Bielefeld and a microstrip-based VNA-FMR setup was used to study their magnetic properties. The dependence of the in-plane anisotropies and the Gilbert damping parameter on the thickness and the determination of the interface perpendicular anisotropy constant K$_S^\perp$ for the CFA/MgO interface is presented.

The stack composition is MgO(100)(subs)/MgO(5)/CFA(d)/MgO(7)/Ru(2) with $d = 7,9,11,15,$ 20,40 and 80 nm. Rf$-$sputtering was used for MgO and dc$-$sputtering for the rest. No annealing steps were performed. The XRD characterization shows crystalline (100)$-$growth for all samples. The layer stack is symmetric around CFA so that a similar interface is expected for both sides.

The in-plane anisotropies were studied by measuring the dependence of the resonant field H_{FMR} on the azimuthal angle ϕ. Fig. 1 shows this dependence for two of the samples, with 20 and 40 nm CFA thickness, in the range 0-180$^{\text{o}}$ at 18 GHz. An overall four-fold anisotropy, as expected from the cubic lattice of CFA and the (100) growth direction is observed. The easy axes correspond to 0$^{\text{o}}$ and 90$^{\text{o}}$. Overimposed to this, an additional weaker two-fold uniaxial anisotropy is also observed. It can be recognized by the different value for H_{FMR} in the 20 nm film at 0$^{\text{o}}$ and 90$^{\text{o}}$ and in the 40 nm film at 45$^{\text{o}}$ and 135$^{\text{o}}$. Most probably, this uniaxial anisotropy is induced by stress in the film.
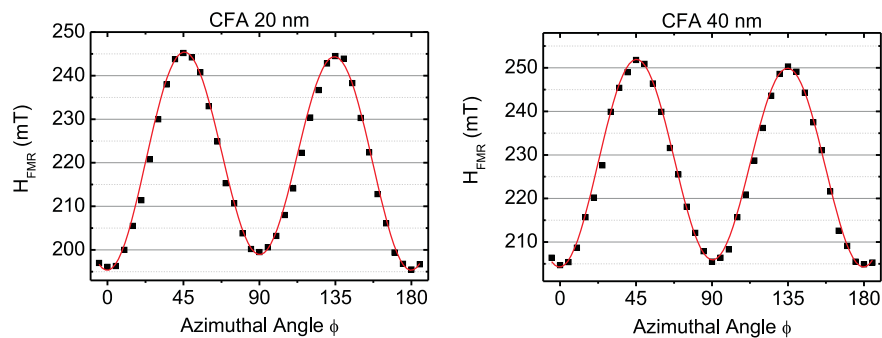

Fig. 1: Dependence of the resonance field H_{FMR} on the azimuthal angle ϕ for CFA films with $d = 20, 40$ nm. The lines are a fit to Eq. 1. The data was measured for $f_{\text{FMR}} = 18$ GHz.
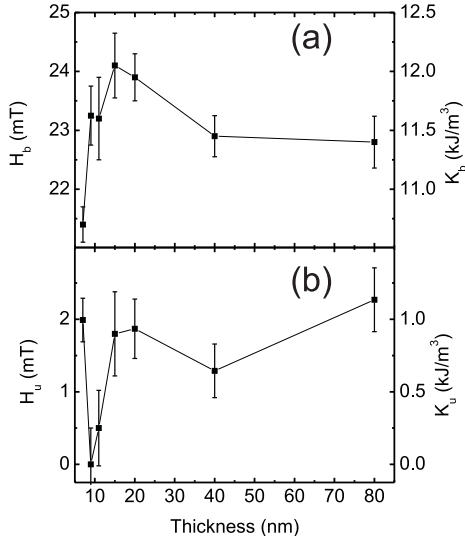
Fig. 2: In-plane anisotropy fields and corresponding anisotropy constants calculated with literature value $M_s = 1000\,\mathrm{kA/m}$ (a) Dependence of the biaxial (four-fold) anisotropy field and (b) dependence of the uniaxial (two-fold) anisotropy field on the CFA thickness.

In order to extract the anisotropy fields the following formula was used:

$$\mu_0 H_{\mathrm{FMR}} = \mu_0 \bar{H}_{\mathrm{FMR}} + H_{\mathrm{b}}\cos(4\phi) + H_{\mathrm{u}}\cos(2\phi + \varphi_m) \quad . \tag{1}$$

Here H_{b} and H_{u} are the biaxial and uniaxial anisotropy fields, ϕ is the in-plane azimuthal angle and $\bar{H}_{\mathrm{FMR}}$ is the averaged value. The angle φ_m allows for a misalignment of the uniaxial and biaxial contributions, i.e. the easy axis of both contributions may be at different angles. The lines in Fig. 1 are a fit to this formula. These field values are related to the anisotropy constants $H_{\mathrm{b,u}} = \frac{2K_{\mathrm{b,u}}}{M_s}$.

The results of the fits are plotted in Fig. 2 as a function of the CFA film thickness. The panel a shows the dependence of the biaxial anisotropy field H_{b}. On the right axis the corresponding values of the anisotropy constant K_{b} have been calculated. For this the literature value on $M_s = 1000\,\mathrm{kA/m}$ has been used [1]. The anisotropy field increases slowly with decreasing thickness from 80 nm up to a maximum value at $d = 15\text{-}20\,\mathrm{nm}$ and then decreases strongly for thinner films. The absolute values are in concordance with literature data. For instance in Ref. [2] the anisotropy field for CFA films grown also on MgO(100) substrates is 22.4 mT for $d = 45\,\mathrm{nm}$. The uniaxial field H_{u} is an order of magnitude smaller as shown in Fig. 2b and shows some similarities with Fig. 2a. There is also a local maximum around $d = 15\text{-}20\,\mathrm{nm}$ but in addition the value shows a large increase for the thinnest of the measured samples. This is probably due to the lattice mismatch between CFA and MgO.

From the dependence of H_{FMR} on the resonance frequency f_{FMR} the effective magnetization M_{eff} can be extracted using a fit to Kittel's formula [3]. For a more detailed description of the FMR measurement and analysis procedure refer please to [4]. M_{eff} is now related to the saturation magnetization of CFA by

$$M_{\mathrm{eff}} = M_{\mathrm{s}} - H_K^{\perp} = M_{\mathrm{s}} - \frac{2K_{\mathrm{S}}^{\perp}}{\mu_0 M_{\mathrm{s}} d} \quad , \tag{2}$$

where $K_{\mathrm{S}}^{\perp}$ is the perpendicular surface (or interfacial) anisotropy constant.

Fig. 3 shows now the results for the CFA series and it can be immediately recognized that the slope has a positive sign and the increase of M_{eff} saturates at same point. As a result, the value of the constant is negative, $K_{\mathrm{S}}^{\perp} = -2.4 \pm 0.5\,\mathrm{mJ/m^2}$ (hollow values not considered for the fit).
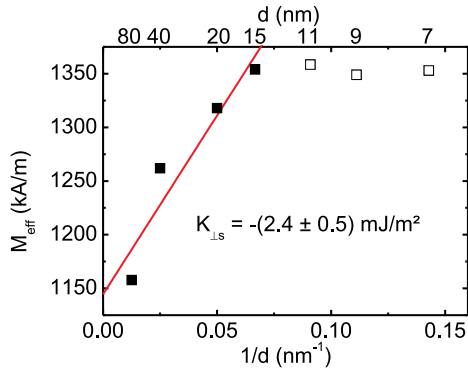
AG MAGNETISMUS
TU KAISERSLAUTERN

Fig. 3: Dependence of M_{eff} extracted from the FMR measurements on the inverse thickness $1/d$. The line is a fit to Eq. 2, the hollow data points were not considered.

Similar results were presented by Belmeguenai et al. in [1]. The value of $K_S^{\perp}$ is smaller than in our case and also negative ($-1.86\,\mathrm{mJ/m^2}$). In this case the films are (110)-ordered and textured so that they may be not totally comparable. However, the same group measured also a negative value $K_S^{\perp} = -1.8\,\mathrm{mJ/m^2}$ for epitaxial (100) oriented films grown on MgO(100) substrates [2]. In both cases the films were capped with MgO/Cr,Ta so that, as in our case, a CFA/MgO interface is present at both sides (for the case with Si substrates also a MgO buffer layer is used). An open question is if the saturation behavior observed in this Report is also present in their case. Unfortunately they reported a smaller range of thicknesses (up to $1/d = 0.10\,\mathrm{nm^{-1}}$).

The interpretation of the negative value of $K_S^{\perp}$ is that the interface anisotropy favors an in-plane orientation of the magnetization. This would mean that this combination is not a good choice when trying to realize PMA systems. However it has to be commented that PMA with Ta/CFA/MgO (or Cr or Ru) systems have been indeed achieved [6, 7] with values of $K_S^{\perp} = +0.6\,\mathrm{mJ/m^2}$ for the Ta case, $+1.0\,\mathrm{mJ/m^2}$ for Cr and $+2.0\,\mathrm{mJ/m^2}$ for Ru. However the question is if the Ta,Cr,Ru/CFA interface induces PMA while the CFA/MgO one is inducing an in-plane orientation. If this is the case, the measured value would just be the sum of both. The alternative explanation is that the better or worse lattice mismatch with these metals modifies the CFA growth properties including lattice constant (which is not relaxed in thin films) and this modifies the CFA/MgO interface. In the same publication almost vanishing $K_S^{\perp}$ was measured for Cr,Ru/CFA/Cr,Ru pointing out to the second possibility. The case for Ta is open.

An important fact has to be reminded here, the studied sample series is in the as-deposited state whereas for its application in TMR devices the stacks must be annealed in order to achieve large magnetoresistance values [11]. The annealing modifies also the interface CFA/MgO and therefore also possibly the value of $K_S^{\perp}$. For this reason, further studies with annealed series are planned.

By setting $d = \infty$ in Eq. 2 it is possible to extract a value for M_s of $1140 \pm 30\,\mathrm{kA/m}$ from the linear fit. This value is larger than the ones reported in [1, 5] (1000-1030 kA/m) but similar to a FMR study [8] on very thick (140 nm) CFA polycrystalline films providing a value of $M_{\mathrm{eff}} = 1200\,\mathrm{kA/m}$.

Figure 4 shows the dependence of the Gilbert damping parameter α on the thickness d. A logarithmic scale is chosen for d for better visibility. If we do not consider the large value for $d = 80$ nm we observe an increase of α with decreasing thickness up to a saturation value around $9\text{-}10 \cdot 10^{-3}$. The smallest value obtained for this series is $\alpha = 3.0 \pm 0.1 \cdot 10^{-3}$. When comparing to the literature it has to be taken into account that the value of α is very sensitive to the growth conditions and to the annealing temperature. Therefore the scatter of values is large. The smallest reported value [9] is around $1 \cdot 10^{-3}$ but for films annealed at 600°C. The damping increases when the annealing temperature is lower up to values similar to the ones reported here at $\sim$450°C.

Concerning the large damping value for the 80 nm sample, it is a common behavior in soft magnetic
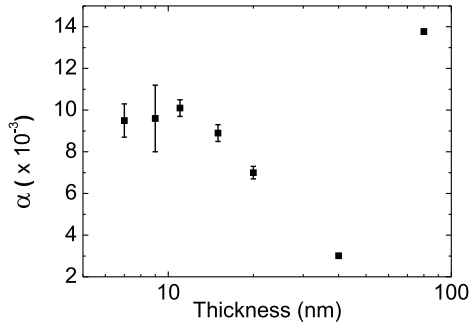
Fig. 4: Dependence of the Gilbert damping parameter α on the thickness d.

thin films that the damping increases strongly with thickness starting at a certain value. An example of this can be seen for NiFe in the literature [10]. In this case the damping of the films strongly increases starting at $d = 90\,\mathrm{nm}$. The reason for that is a non-homogeneous magnetization state for thicker films which opens new loss channels in addition to two-magnon scattering responsible for Gilbert-like behavior in in-plane magnetized films.

In summary, we studied the thickness dependent magnetic properties of CFA and we estimate a negative value for $K_S^{\perp}$. We obtained a minimum value for α of $3 \cdot 10^{-3}$ but the damping increases with decreasing thickness. A comparison with annealed samples is planned in order to determine the influence of a thermal treatment and to analyze the results of films fully compatible with TMR devices.

References

[1]   M. Belmeguenai, H. Tuzcuoglu, M. Gabor, T. Petrisor, C. Tiusan, D. Berling, F. Zighem, S. M. Chérif, *Magnetic and structural properties of Co$_2$FeAl thin films grown on Si*, J. of Magn. and Magn. Mat. **373**, 140 (2015).

[2]   M. Belmeguenai, H. Tuzcuoglu, M. S. Gabor, T. Petrisor, Jr., C. Tiusan, D. Berling, F. Zighem, T. Chauveau, S. M. Chérif, P. Moch, *Co$_2$FeAl thin films grown on MgO substrates: Correlation between static, dynamic, and structural properties*, Phys. Rev. B **87**, 184431 (2013).

[3]   C. Kittel, *On the theory of ferromagnetic resonance absorption*, Phys. Rev. **73**, 155 (1948).

[4]   A. Conca, S. Keller, L. Mihalceanu, T. Kehagias, G. P. Dimitrakopulos, B. Hillebrands, E. Th. Papaioannou, *Study of fully epitaxial Fe/Pt bilayers for spin pumping by ferromagnetic resonance spectroscopy*, Phys. Rev. B **93**, 134405 (2016).

[5]   G. Ortiz, M.S. Gabor, T. Petrisor, Jr., F. Boust, F. Issac, C. Tiusan, M. Hehn, J. F. Bobo, *Static and dynamic magnetic properties of epitaxial Co$_2$FeAl Heusler alloy thin films*, J. Appl. Phys. **109**, 07D324 (2011).

[6]   M. S. Gabor, T. Petrisor Jr., C. Tiusan, T. Petrisor, *Perpendicular magnetic anisotropy in Ta/Co$_2$FeAl/MgO multilayers*, J. Appl. Phys. **114**, 063905 (2013).

[7]   Z. Wen, H. Sukegawa1, S. Mitani and K. Inomata, *Perpendicular magnetization of Co$_2$FeAl full-Heusler alloy films induced by MgO interface*, Appl. Phys. Lett. **98**, 242507 (2011).

[8]   A. Yadav, S. Chaudhary, *Structural and dynamical magnetic response of co-sputtered Co$_2$FeAl Heusler alloy thin films grown at different substrate temperatures*, J. Appl. Phys. **115**, 133916 (2014).

[9]   S. Mizukami, D. Watanabe, M. Oogane, Y. Ando, Y. Miura, M. Shirai, T. Miyazaki, *Low damping constant for Co$_2$FeAl Heusler alloy films and its correlation with density of states*, J. Appl. Phys. **105**, 07D306 (2009).

[10] Y. Chen, D. Hung, Y. Yao, S. Lee, H. Ji, and C. Yu, *Ferromagnetic resonance study of thickness-dependent magnetization precession in Ni$_{80}$Fe$_{20}$ films*, J. Appl. Phys. **101**, 09C104 (2007).

[11] O. Schebaum, D. Ebke, A. Niemeyer, G. Reiss, J. S. Moodera, A. Thomas, *Direct measurement of the spin polarization of Co$_2$FeAl in combination with MgO tunnel barriers*, J. Appl. Phys. **107**, 09C717 (2010).

AG MAGNETISMUS
TU KAISERSLAUTERN

4.15   Spin-transfer torque induced spin-wave heating in a microstructured Heusler-Pt waveguide

T. Meyer, P. Pirro, T. Brächer*, A.A. Serga, and B. Hillebrands

In collaboration with H. Naganuma, K. Mukaiyama, M. Oogane, and Y. Ando
Department of Applied Physics, Graduate School of Engineering, Tohoku University, Sendai 980-8579, Japan

*Current affiliation: Université Grenoble Alpes, CNRS, CEA, INAC-SPINTEC, 38054 Grenoble, France

In the last years, the utilization of magnons as information carrier is a promising approach for the development of post-CMOS technologies. The realization of magnon logic devices like, e.g., the magnon transistor [1], which allows to control the flow of magnons by other magnons, are first proof-of-principle concepts for future magnonic applications. However, spin-wave (SW) based applications are limited by the Gilbert damping parameter [2] as it determines the lifetime and the propagation length of the spin waves. Thus, the development of materials like the here-used cobalt-based Heusler compounds, which offer a low magnon damping gained a large interest. Moreover, the spin-transfer-torque (STT) effect [3] in combination with the spin-Hall effect (SHE) [4], which converts charge currents into pure spin currents in a normal metal, possesses the potential to control the effective damping in magnonic circuits. Using these effects, devices which are able to amplify and even excite spin waves by a DC current [5–9] can be realized.

In this Report, we focus on the time evolution of the SW intensity and frequency change caused by the modulation of the effective magnon damping via the SHE and STT effect in a spatially extended SW waveguide. The results show that, in the investigated system, both the damping and the density of magnons can be controlled in a wide range by an applied DC current pulse. Furthermore, it is revealed that, in the case of a damping reduction by an applied current pulse, the relaxation of the increased number of magnons to the phononic bath strongly heats the magnetic medium. As a result, the SW heating turns out to be the main heat source and dominates the Joule heating which can be neglected in the presented experiments.

The magnetic layer of the SW waveguide consists of the Heusler compound $Co_2Mn_{0.6}Fe_{0.4}Si$ (CMFS) [10] with a thickness of 5 nm (see Fig. 1). It is grown on a MgO substrate and a 5 nm thick Cr layer acts as a buffer layer. This layer supports the single-crystalline growth of the CMFS layer since the magnetic properties strongly depend on its crystal order. On top of the CMFS film, a Pt layer of 2 nm thickness is deposited. The microstructuring into a 7 µm wide and 30 µm long
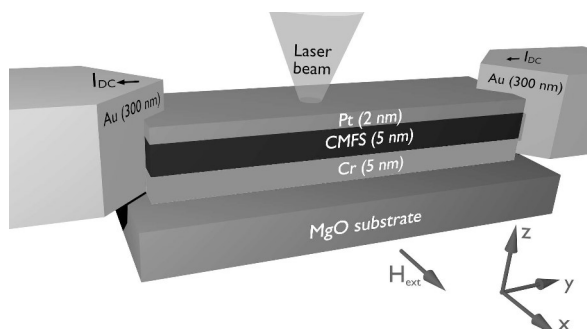

Fig. 1: Sketch of the investigated sample. The 7 µm wide and 30 µm long waveguide consists of a 5 nm thick Cr buffer layer grown on a MgO substrate, a 5 nm CMFS layer and a 2 nm Pt layer on top. Two 300 nm thick Au contacts at each end allow for the application of a DC current to the layer stack. The magnetization is aligned along the z-direction.
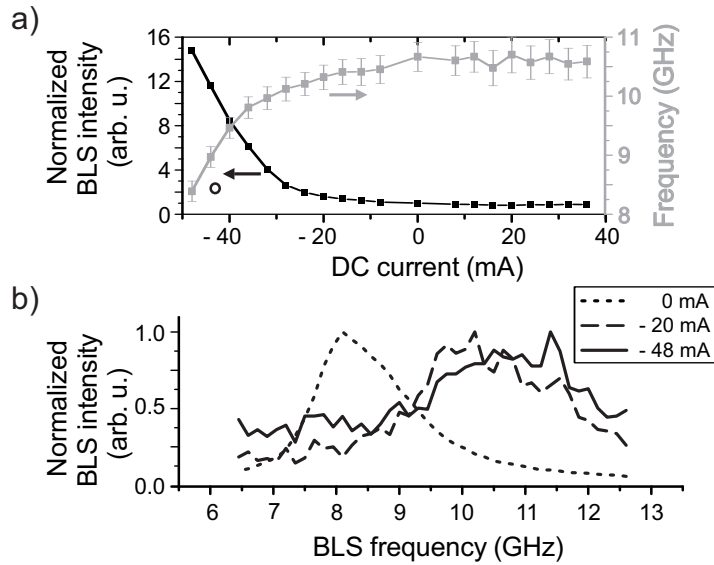
a)

b)

Fig. 2: a) The black squares show the integrated BLS intensity during the current pulse, normalized to the case of zero current. The corresponding center frequency of the spin-wave spectrum is depicted by the grey squares. b) Exemplary spin-wave frequency spectra during the current pulse for different applied currents.

microstrip-shaped waveguide is performed using electron beam lithography and ion beam etching techniques. At each end of the microstrip, 300 nm thick Au contacts are patterned in order to apply electric current pulses to the layered structure. The electric currents in the Cr and in the Pt layers are partially converted into spin currents by the SHE and, subsequently, they are injected into the CMFS film. As Cr and Pt show different signs of their spin-Hall angles [11, 12] and since the spin currents enter the CMFS layer from opposite surfaces, both spin currents add up, whereas the electric currents related Oersted fields counteract and practically cancel each other inside the CMFS film. In this study, by applying an external magnetic field of $\mu_0 H_{ext} = +70$ mT, the CMFS layer is magnetized perpendicular to the electric current direction and, thus, along the short axis of the waveguide. In this geometry, the injected spin currents act as a damping-like torque on the magnetization via the STT effect. A reduced (increased) damping results in an increase (decrease) of the thermal equilibrium magnon density. To observe the temporal evolution of this change in the magnon density, we employ time-resolved Brillouin light scattering (BLS) microscopy [13]. The probing laser spot is positioned in the center of the SW waveguide (see Fig. 1).

The black squares in Fig. 2a depict the current dependent BLS intensity integrated over the pulse duration and over the whole experimentally accessible SW spectrum normalized to the BLS signal measured at zero current. The grey squares show the corresponding center frequency of the SW spectrum obtained from the SW frequency spectra, which are exemplarily shown in Fig. 2b for different applied currents. For large negative currents, the density of the thermally excited magnons increases by more than a factor of 15. In this case, the SW frequency shows a large shift towards lower frequencies of approximately 2 GHz. In contrast, for positive applied currents, the BLS intensity is slightly suppressed and only a comparably small frequency shift is observed which is in agreement with other works [7, 14].

The observed lowering of the SW frequencies for negative applied currents can, in general, be caused by an increase of the number of the externally injected magnons or by a heating of the magnetic layer. Both processes lead to a reduced effective saturation magnetization followed by a downshift of the SW dispersion relation. As the observed frequency shift mainly relates to negative applied currents, the Joule heating effect can be excluded as the main cause of a heating of the CMFS as this effect should be independent on the current polarity.

To investigate the origin of the SW frequency shift in more detail, we performed a time-resolved
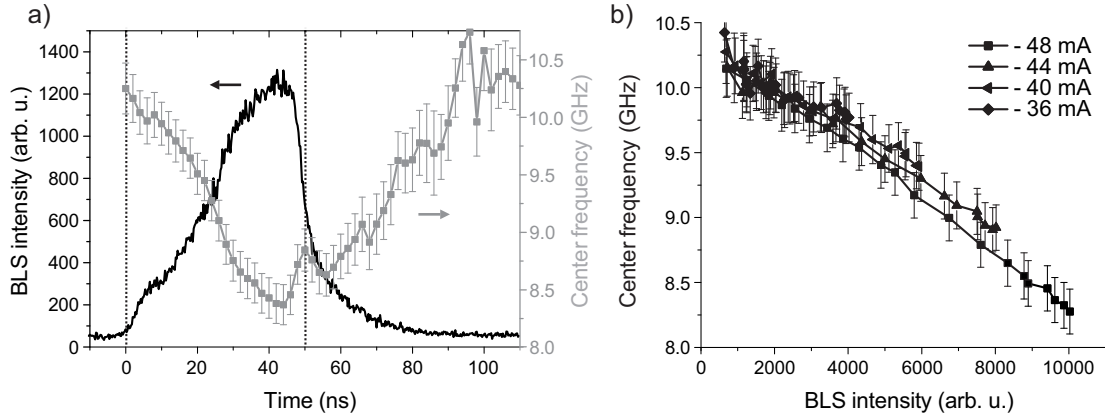
Fig. 3: a) Time evolution of the SW intensity (black line) and the corresponding center frequency of the SW spectrum (grey squares) for a 50 ns long applied current pulse of -48 mA (regimes (I) - (III)). b) Center frequency of the SW spectrum depending on the SW intensity for different applied negative currents.

analysis of the collected BLS spectra. The black curve and the grey squares in Fig. 3a exemplarily show the time-resolved BLS intensity as well as the time evolution of the center frequency of the SW spectrum for a 50 ns long applied DC current pulse of -48 mA, respectively. The temporal extent of the current pulse is given by the dashed lines. For the presented case, the threshold current of $I_{DC,Th} \approx -15$ mA which is necessary for a damping compensation is significantly overcome by the applied current pulse. This results in a negative effective SW damping and, thus, in a rapid increase of the magnon density in time. The data clearly shows that the center frequency of the spectrum drops and initially follows the temporal evolution of the magnon density. In contrast, after the current pulse is switched off at the time of $t \geq 50$ ns, the magnon density quickly decreases within a few nanoseconds. However, the spin-wave frequency relaxes much more slowly within a time of several tens of nanoseconds to the equilibrium value of approximately 10.5 GHz which is much longer than the magnon lifetimes.

The revealed deviation in the time scales of the intensity and frequency relaxation rates can be understood taking into account the lifetimes of magnons and phonons, which are the main carriers of the heat in the system. In the presented case of an applied current of -48 mA, the increase of the magnon density via the STT effect results in an overcompensated effective SW damping and in a related transfer of energy from the DC current to the SW system. But even if the effective SW damping is negative, the Gilbert damping is unchanged, leading to a continuous energy transfer from the magnonic system to the electronic and phononic systems via magnon-electron and magnon-phonon scattering processes. Thus, the energy transfer from the magnon system is proportional to the magnon density which leads to a heating of the magnetic layer as the SW intensity increases during the current pulse. Furthermore, magnons show lifetimes of only $\tau_{sw} \approx 1$ ns in the investigated system while the heat in the magnetic layer, which is mainly carried by phonons, relaxes within the phonon lifetime of several tens of nanoseconds. This longer lifetime leads to a delayed frequency shift, which is still present even if the externally injected magnons have already decayed and the intensity of the relatively long-wavelength spin waves, which are detectable by BLS spectroscopy, has dropped to its thermal equilibrium value.

As mentioned before, Joule heating can be excluded as the origin for the observed temporal behavior. Assuming the SW decay as the main heat source, the frequency shift should only correlate to the magnon density and should be independent on the applied current. To prove this, the measured time-dependent BLS intensity is correlated to the SW frequency at each point of time during the

current pulse from 0 ns to 50 ns for different applied currents. The results are shown in Fig. 3b. All lines are more or less identical and only a small change in the slope can be identified which is caused by a residual Joule heating. This data proves that the shift of the SW frequency is mainly depending on the net magnon density and, thus, is a caused by magnon heating.

In conclusion, we have shown that the effective SW damping in Heusler-Pt waveguides can be controlled in a wide range in the case of short applied current pulses. By using time-resolved BLS measurements, the time evolution of the spin-wave intensity and of the spin-wave frequency during and after the current pulse were investigated. The revealed deviation in the decay rates of the intensity and the frequency of a freely evolving magnonic system evidences that decaying magnons are the main source of heating in our experiment. Furthermore, we found that the frequency shift is practically independent on the applied current, proving that Joule heating can be neglected. These results show that in any device using the STT effect to generate or amplify magnons, the magnons themselves as a heat source need to be taken into account.

References

[1] A.V. Chumak, A.A. Serga, B. Hillebrands, *Magnon transistor for all-magnon data processing*, Nat. Comm. **5**, 1700 (2014).

[2] T.L. Gilbert, *A phenomenological theory of damping in ferromagnetic materials*, IEEE Trans. Magn. **40**, 3443 (2004).

[3] J.C. Slonczewski, *Current-driven excitation of magnetic multilayers*, J. Magn. Magn. Mater. **159** (1996).

[4] J. Hirsch, *Spin Hall effect*, Phys. Rev. Lett. **83**, 1834 (1999).

[5] K. Ando, S. Takahashi, K. Harii, K. Sasage, J. Ieda, S. Maekawa, E. Saitoh, *Electric manipulation of spin relaxation using the spin Hall effect*, Phys. Rev. Lett. **101**, 036601 (2008).

[6] V.E. Demidov, S. Urazhdin, H. Ulrichs, V. Tiberkevich, A. Slavin, D. Baither, G. Schmitz, S.O. Demokritov, *Magnetic nano-oscillator driven by pure spin current*, Nat. mater. **11** (2012).

[7] M. Evelt, V.E. Demidov, V. Bessonov, S.O. Demokritov, J.L. Prieto, M. Muñoz, J. Ben Youssef, V.V. Naletov, G. de Loubens, O. Klein, M. Collet, K. Garcia-Hernandez, P. Bortolotti, V. Cros and A. Anane, *High-efficiency control of spin-wave propagation in ultra-thin yttrium iron garnet by the spin-orbit torque*, Appl. Phys. Lett. **108**, 172406 (2016).

[8] O. Gladii, M. Collet, K. Garcia-Hernandez, C. Cheng, S. Xavier, P. Bortolotti, V. Cros, Y. Henry, J.-V. Kim, A. Anane, M. Bailleul, *Spin wave amplification using the spin Hall effect in permalloy/platinum bilayers*, Appl. Phys. Lett. **108**, 202407 (2016).

[9] K. An, D.R. Birt, C.-F. Pai, K. Olsson, D.C. Ralph, R.A. Buhrmann, X. Li, *Control of propagating spin waves via spin transfer torque in a metallic bilayer waveguide*, Phys. Rev. B **89**, 140405 (2014).

[10] T. Sebastian, Y. Ohdaira, T. Kubota, P. Pirro, T. Brächer, K. Vogt, A.A. Serga, H. Naganuma, M. Oogane, Y. Ando, B. Hillebrands, *Low-damping spin-wave propagation in a micro-structured Co2Mn0.6Fe0.4Si Heusler waveguide*, Appl. Phys. Lett. **100**, 112402 (2012).

[11] C. Du, H. Wang, F. Yang, P.C. Hammel, *Systematic variation of spin-orbit coupling with d-orbital filling: Large inverse spin Hall effect in 3 d transition metals*, Phys. Rev. B **90**, 140407 (2014).

[12] M. Schreier, G.E.W. Bauer, V. Vasyuchka, J. Flipse, K. Uchida, J. Lotze, V. Lauer, A. Chumak, A.A. Serga, S. Daimon, T. Kikkawa, E. Saitoh, B.J. van Wees, B. Hillebrands, R. Gross, S.T.B. Goennenwein, *Sign of inverse spin Hall voltages generated by ferromagnetic resonance and temperature gradients in yttrium iron garnet platinum bilayers*, J. Phys. D **48**, 025001 (2014).

[13] T. Sebastian, K. Schultheiss, B. Obry, B. Hillebrands, H. Schultheiss, *Micro-focused Brillouin light scattering: imaging spin waves at the nanoscale*, Front. Phys. **3**, 35 (2015).

[14] V.E. Demidov, S. Urazhdin, E.R.J. Edwards, M.D. Stiles, R.D. McMichael, S.O. Demokritov, *Control of magnetic fluctuations by spin current*, Phys. Rev. Lett. **107**, 107204 (2011).

AG MAGNETISMUS
TU KAISERSLAUTERN

4.16 Magneto-plasmonic metamaterials

E.Th. Papaioannou

in collaboration with Markus Rollinger, Philip Thielen, Mirko Cinchetti, Martin Aeschlimann, Fachbereich Physik and Forschungszentrum OPTIMAS, Technische Universität Kaiserslautern, 67663 Kaiserslautern, Germany, and

in collaboration with Emil Melander, Erik Östman, Vassilios Kapaklis, Department of Physics and Astronomy, Uppsala University, Box 516, SE-75120, Uppsala, Sweden.

The field of magneto-plasmonics is growing rapidly nowadays with the main aim to explore the combination of magnetic and plasmonic functionalities in patterned nano-structures [2]. The presence of surface plasmon polaritons (SPPs) in magnetic materials can strongly modify the magneto-optical response. In spite of these numerous studies on the plasmonic behavior of magneto-plasmonic lattices and the enhanced magneto-optical signal, the mechanism of coupling between plasmonic and magneto-optical properties is not fully clarified yet. Here, we tackle this open issue by combining photoemission electron microscopy (PEEM) with magneto-optical spectroscopy. We link the near-field with the far-field effects and thereby we introduce the concept of a magneto-plasmonic meta-structure whose magneto-optic response can be actively controlled through its optical properties.

In our study, we investigate a Ni anti-dot film of 100 nm thickness with holes of $d = 275$ nm diameter and a center to center distance of $a = 470$ nm, as shown in Fig. 1. The schematic representation of the hexagonal antidot pattern of Fig. 1 defines all directions and angles used in this work. Due to $\phi = 0°$ and a very small value of θ, s-polarization is equivalent to the alignment of the polarization vector along the Γ-M direction, and the p-polarization is equivalent to alignment along the Γ-K direction.

To provide direct evidence for the excitation of SPPs on magneto-plasmonic structures we use Photoemission Electron Microscopy (PEEM). In Fig. 2 we present PEEM images recorded at different excitation energies. The excitation of SPPs due to the coupling of the incident light with the periodic lattice will cause an enhancement of the electric near-field that can be directly measured with PEEM. The three rows of Fig. 2 show images of the detected electron intensity for different polarization directions, i.e. aligned along the Γ-K direction (0°) and along the Γ-M
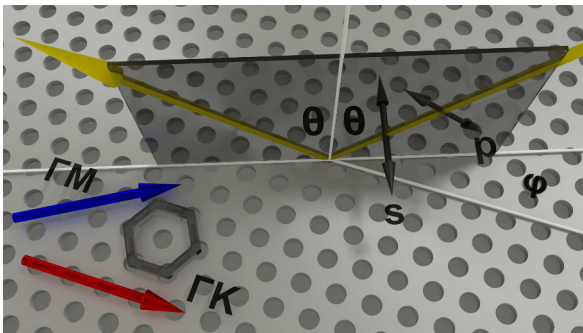
Fig. 1: Schematic view of the used geometry and the definition of the angles. θ is the angle of incidence from the surface normal, φ the angle between the polarization plane and the nearest neighbor hole direction (Γ-K), Γ-K is the nearest and Γ-M next-nearest neighbor direction noted in the real space. All of our measurements were performed by keeping $\varphi = 0$.

This work has been recently published in Nano Letters [1].

E ⟷ 0°, Γ-K   ↗ 30°, Γ-M

3.1 eV

3.4 eV

2.4 eV
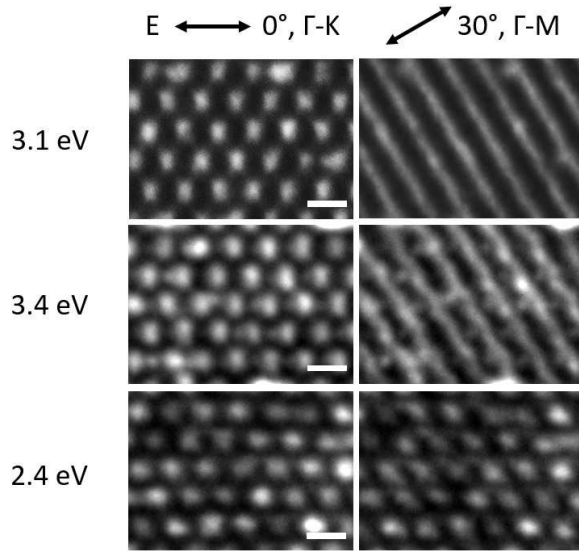
Fig. 2: PEEM images recorded at different photon energies of the Ni based anti-dot film. The scale bar for all images is 500 nm. (First row) Photoemission patterns excited at $\hbar\omega = 3.1$ eV. Spot-like emission is observed from the region in between the holes for incident light aligned along the Γ-K direction. Incident light polarized along the Γ-M direction causes emission patterns that form lines perpendicular to the E-field vector direction. (Second row) Photoemission pattern excited at $\hbar\omega = 3.4$ eV are similar to the patterns observed for $\hbar\omega = 3.1$ eV. (Third row) Photoemission pattern excited at $\hbar\omega = 2.4$ eV. Weak spot-like emission as well as mainly homogeneous emission is observed that does not follow the symmetry of the patterned while rotating the polarization.

direction (30°). They are recorded at photon energies of $\hbar\omega = 3.1$ eV and 3.4 eV, i.e. close to the onset of SPP resonances and at a photon energy of $\hbar\omega = 2.4$ eV.

At $\hbar\omega = 3.1$ eV PEEM images show very specific emission patterns for different polarizations: either spot-like or continuous lines. In particular, when the incident E-field is aligned along the direction of the nearest neighbors, PEEM images (for the Γ-K direction) reveal dot-like emission from the sample surface. The spots are formed between the holes and they are also arranged in a hexagonal pattern. This behavior is repeated for every 60° of rotation of the polarization state of light, thus every time the polarization is oriented along the Γ-K direction of the hexagonal hole lattice. When the E-field is rotated by 30° or 90°, i.e., oriented along the Γ-M direction, strong changes in the PEEM images are observed. Now bright continuous lines are formed perpendicular to the polarization direction of light. Again the lines appear on the Ni and not in the holes. The pattern is also repeated for every 60° of rotation of the polarization of the light, mirroring the symmetry of the structure for the Γ-M direction. At $\hbar\omega = 3.4$ eV photon energy the PEEM images exhibit a similar behavior: hexagonal bright spot formation for incident light polarized along the Γ-K direction and continuous lines for incident light polarization along the Γ-M direction. The results for a photon energy of $\hbar\omega = 2.4$ eV are obtained away from a SPP resonance. Spot-like emission is observed from different areas of the surface for 0° and 30° rotation of the polarization of the incident light while a more homogeneous emission is seen for 60° and 90° rotation [1]. The small changes in the photoemission patterns are not as distinct as before and evenmore do not mirror the rotational symmetry of the lattice of 60°. A distinct line formation in the photoemission pattern is not discernible here for any angle of polarization.

The dramatic changes in the near-field distribution recorded by PEEM can be correlated to the magneto-optic Kerr response of the structure. Figure 3 (top-graph) shows the polar Kerr rotation spectra for different polarization states of the incident light. The reference film exhibits two broad features around $\hbar\omega = 1.5$ eV and around $\hbar\omega = 3$ eV for both polarization states. This behavior has been associated in Ni with the d-p transitions of electrons at the top majority spin band and at the bottom of the minority spin band [3]. These characteristics are changed in the case of the patterned film as Fig. 3 (top, filled symbols) reveals. A large enhancement of the polar Kerr rotation θ_K is observed with respect to the continuous film for incident light polarized along both directions, Γ-K and Γ-M, at photon energies above $\hbar\omega = 2.4$ eV. Interestingly at $\hbar\omega = 2.4$ eV, the values of the Kerr rotation coincide for both polarization directions and for the reference continuous sample.
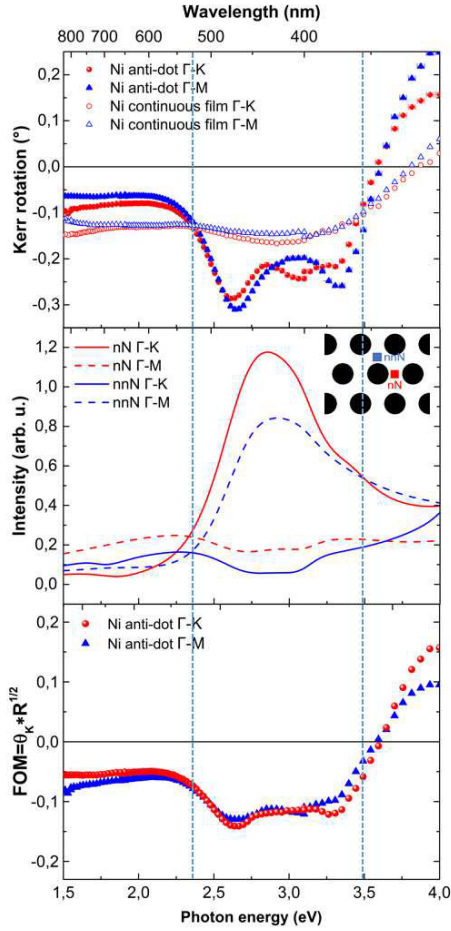
Fig. 3: (Top-graph) Polar Kerr rotation spectra of the Ni anti-dot (filled symbols) and a Ni continuous film (open symbols) used as a reference. Measurements are performed for 0°- and 90°-polarized light aligned along the Γ-K and Γ-M direction, respectively, for both samples at magnetic saturation at $B = 1T$. (Middle-graph) Enhancement of the electric near-field intensities normalized to the incident field value and calculated for 0°- and 90°-polarized light from the simulated patterns. The graphical inset shows the points on the surface of the hexagonal lattice where the intensity is calculated. nN denotes the nearest neighbor position where spot-like emission has been observed for 0° polarization (Γ-K) while nnN marks the next-nearest neighbor position where line-formation has been observed for 90° polarization (Γ-M). (Bottom-graph) Magneto-optic figure of merit (FOM) calculated for both polarization states reveals the enhancement of the pure magneto-optical conversion. The latter is correlated to the magnitude of the electric field shown in the middle graph.

At this energy, the theoretical calculations predict no surface plasmon resonance, and the PEEM images show no polarization-dependent features. Above this photon energy the values of the Kerr rotation are enhanced and remain higher compared to the continuous film up to a photon energy of $\hbar\omega = 3.5$ eV. At even higher photon energies the Kerr rotation changes sign but still remains higher in absolute values than that of the continuous film for both polarizations. PEEM images recorded at $\hbar\omega = 3.1$ eV and $\hbar\omega = 3.4$ eV have revealed the distribution of the near-field either as stripe-lines or as bright spots depending on the polarization state. This spatial distribution of the electric near-field recorded by PEEM influences the magneto-optic enhancement.

We have determined the intensity of the enhanced electric field patterns with the help of the PEEM experiment and simulations for the full spectral range [1]. The corresponding curves are plotted in Fig. 3 (middle-graph) for a polarization orientation along Γ-K and Γ-M, each calculated in a position where an enhanced photoelectron yield has been observed for one of those orientations: between two neighboring holes (denoted as nN, see the inset graphic), where spot-like emission has been observed, and between next-nearest neighbors (denoted as nnN), where the stripe-formation has been observed. We see that the electric fields are strongly intensified for light polarized either along the Γ-K or Γ-M direction (the first shows higher intensity) at a spectral region between 2.5 and 3.5 eV. Inside this spectral region we also observed a strong magneto-optic enhancement. This is a clear indication that the intensification of the electric field generated by the spatial distribution of the surface plasmons leads to an increase of the pure magneto-optic contribution. In particular, the magneto-optic Fresnel coefficient r_{sp} can be written as [2]:

$$|r_{\mathrm{ps}}| \propto \langle E_{\mathrm{p}} E_{\mathrm{s}} \rangle d |\varepsilon_{\mathrm{mo}}| \quad , \tag{1}$$

where d is the thickness of the film, $\varepsilon_{\mathrm{mo}}$ its magneto-optical constant and $\langle E_{\mathrm{p}} E_{\mathrm{s}} \rangle$ is the mean value of the product of both components of the field inside the MO layer. The enhancement of both components of the electric field shown in Fig. 3 (middle-graph) increases the pure magneto-optic contribution of the Kerr rotation. The enhancement of the electric field is also present for energies above $\hbar\omega = 3.5$ eV leading to higher positive values of the Kerr rotation.

From the top and the middle graph of Fig. 3 the correlation of Kerr rotation and enhancement of the electric field for both polarizations of the incident light is clearly shown. Still, the complex Kerr rotation is a relative quantity, it depends on the ratio of polarization conversion (r_{ps}) to the extrinsic reflectivity (r_{ss}). Accordingly, the experimentally measured real part (θ_{K}) of the complex Kerr rotation is partially representing the polarization conversion but it also depends on the reflectivity. To reveal this dependence we have normalized the measured Kerr rotation values to the reflectivity. In particular, we introduce the parameter of figure of merit (FOM), that is defined here as the product of Kerr rotation θ_{K} and the square root of reflectivity $\sqrt{\mathrm{R}}$. FOM is used to normalize the measured magneto-optical activity with respect to the excitation intensity or, in other words, to the optical contributions (reflectivity), with the aim to extract the pure magneto-optical contribution, (r_{ps}). In Fig. 3 (bottom-graph) we present the result of such a normalization process with the help of the FOM. The presented FOM values for both polarization states in Fig. 3 (bottom-graph) to a good approximation contain all the essential information about the polarization conversion. The FOM diagram affirms that the polarization conversion is enhanced and is associated to the magnitude of the intensification of the electric field revealed in the middle-graph of Fig. 3.

In conclusion, our study demonstrates that periodically patterned ferromagnetic metal films can be seen as magneto-plasmonic meta-structures, whose magneto-optic response can be controlled by using the appropriate polarization and wavelength of the incident light. We have shown a strategy (correlation of near- and far-fields effects) to design the magneto-optic response of a magneto-plasmonic material by acting on its optical properties. Tuning the Kerr enhancement with the optical properties of plasmonic excitations introduces the concept of a magneto-plasmonic meta-structure and opens new routes for tailoring the functionality of patterned magneto-plasmonic systems.

References

[1] M. Rollinger, P. Thielen, E. Melander, E. Östman, V. Kapaklis, B. Obry, M. Cinchetti, A. García-Martín, M. Aeschlimann, and E. Th. Papaioannou, *Light localization and magneto-optic enhancement in Ni antidot arrays*, Nano Letters **16**, 2432–2438 (2016).

[2] G. Armelles A. Cebollada, A. García-Martín, M. U.Gonzalez, *Magnetoplasmonics: combining magnetic and plasmonic functionalities*, Advanced Optical Materials **1**, 10–35 (2013).

[3] Buschow, K.; Engen, P.; R.Jongebreur, *Magneto-optical properties of metallic ferromagnetic materials*, Journal of Magnetism and Magnetic Materials **38**, 1–22 (1983).

AG MAGNETISMUS
TU KAISERSLAUTERN

Chapter 5: Publications

Most publications can be downloaded from http://www.physik.uni-kl.de/hillebrands.

5.1   submitted

1. *Damping of parametrically excited magnons in the presence of the longitudinal spin Seebeck effect*
   T. Langner, A. Kirihara, A.A. Serga, B. Hillebrands, V.I. Vasyuchka
   submitted, arXiv:1607.07274

2. *Voltage-controlled nano-scale reconfigurable magnonic crystal*
   Q. Wang, A.V. Chumak, L. Jin, H. Zhang, B. Hillebrands, Z. Zhong
   submitted, arXiv:1607.07975

5.2   published

1. *Spin-transfer torque based damping control of parametrically excited spin waves in a magnetic insulator*
   V. Lauer, A.A. Bozhko, T. Brächer, P. Pirro, V.I. Vasyuchka, A.A. Serga, M.B. Jungfleisch, M. Agrawal, Yu.V. Kobljanskyj, G.A. Melkov, C. Dubs, B. Hillebrands, A.V. Chumak
   Appl. Phys. Lett. **108**, 012402 (2016)

2. *Light localization and magneto-optic enhancement in Ni antidote arrays*
   M. Rollinger, P. Thielen, E. Melander, E. Östmann, V. Kapaklis, B. Obry, M. Cinchetti, A. García-Martín, M. Aeschlimann, E.Th. Papaioannou
   Nano Lett. **16**, 2432-2438 (2016)

3. *Study of fully epitaxial Fe/Pt bilayers for spin pumping by ferromagnetic resonance spectroscopy*
   A. Conca, S. Keller, L. Mihalceanu, T. Kehagias, G.P. Dimitrakopulos, B. Hillebrands, E.Th. Papaioannou
   Phys. Rev. B **93**, 134405 (2016)

4. *Influence of the MgO barrier thickness on the lifetime characteristics of magnetic tunnelling junctions for sensors*
   A. Conca, F. Casper, J. Paul, R. Lehndorff, G. Jakob, M. Kläui, B. Hillebrands, E.Th. Papaioannou
   J. Phys. D :Appl.Phys. **49**, 225001 (2016)

5. *Spin Seebeck effect at microwave frequencies*
   M. Schreier, F. Kramer, H. Huebl, S. Geprägs, R. Gross, S.T.B. Goennenwein, T. Noack, T. Langner, A.A. Serga, B. Hillebrands, V.I. Vasyuchka
   Phys. Rev. B **93**, 225001 (2016)

6. *Supercurrent in a room-temperature Bose-Einstein magnon condensate*
   D.A. Bozhko, A.A. Serga, P. Clausen, V.I. Vasyuchka, F. Heussner, A.A. Melkov, A. Pomyalov,
   V.S. L'vov, B. Hillebrands
   Nature Physics, **12**, 1057 (2016)

7. *Splitting of standing spin-wave modes in circular submicron ferromagnetic dot under axial
   symmetry violation*
   S.A. Bunyaev, V.O. Golub, O.Yu. Salyuk, E.V. Tartakovskaya, N.M. Santos, A.A. Timo-
   pheev, N.A. Sobolev, A.A. Serga, A.V. Chumak, B. Hillebrands, G.N. Kakazei
   Scientific Reports, **5**, 18480 (2015)

5.3   Habilitation thesis

1. *Magnonic crystals for magnon-based data processing*
   Dr. Andrii Chumak, TU Kaiserslautern, June 2016

5.4   Ph.D. thesis

1. *Giant reversible lattice deformation by ionic liquid gating in oxides*
   Donata Passarello, TU Kaiserslautern, performed at IBM Almaden Research Center San
   Jose, CA, USA, local supervisor: Prof. Dr. Dr. h.c. mult. S.S.P. Parkin, November 2015

5.5   Diploma thesis

1. *Untersuchung der Dynamik des longitudinalen Spin Seebeck Effekts in Abhängigkeit von der
   YIG-Schichtdicke in YIG/Pt-Systemen*
   Timo Noack, TU Kaiserslautern, June 2016

Chapter 6: Conferences, Workshops, Schools, Seminars

(shown in chronological order)

6.1   Conference Organization

A.V. Chumak:

Conference Co-Chair
WE-Heraeus-Seminar on "Magnonics - Spin waves connecting charges, spins and photons",
Bad Honnef, Germany, January 2016

B. Hillebrands, E.Th. Papaioannou:

Conference Chair
3rd Core-to-Core International Workshop, Tohoku-York-Kaiserslautern, Kaiserslautern, Germany, June 22-24 2016

6.2   Invited talks

6.2.1   International conferences and workshops

B. Hillebrands:

Novel transport phenomena using magnonic Bose-Einstein condensates
13th RIEC International Workshop on Spintronics, Sendai, Japan, November 2015

A.A. Serga:

Magnon transistor for all-magnon data processing
Magnetics and Optics Research International Symposium (MORIS2015), Penang, Malaysia, November 2015

B. Hillebrands:

Magnonic macroscopic quantum states and supercurrents
Frühjahrstagung des Arbeitskreises Festkörperphysik bei der DPG, Regensburg, March 2016

B. Hillebrands:

Advanced magnonics for information technologies
International Conference on Collaboration in Nanotechnology, IMEC, Leuven, Belgium, May 2016

A.V. Chumak:

Towards magnonic integrated circuits
Insulatronics 2016, Longyearbyen, Svalbard, Norwey, May 2016

A.A. Serga:

Magnon supercurrents in a room-temperature Bose-Einstein condensate
Insulatronics 2016, Longyearbyen, Svalbard, Norwey, May 2016

A. Conca:

Study of FM/Pt,Ta bilayers for spin pumping by ferromagnetic resonance spectroscopy
EMN Meeting Croatia, Dubrovnik, Croatia, May 2016

B. Hillebrands:

Magnon supercurrents
100 Years IMR, Sendai, Japan, May 2016

A.V. Chumak:

Towards integrated magnonic circuits
3rd Core-to-Core International Workshop, Tohoku-York-Kaiserslautern, Kaiserslautern, Germany, June 2016

P. Pirro:

Spin-wave majority gates for magnonic data processing
IEEE ICMM 2016, Tuscaloosa, USA, June 2016

V.I. Vasyuchka:

Spectral properties of the longitudinal spin Seebeck effect
Sol-SkyMag 2016, San Sebastian, Spain, June 2016

E.Th. Papaioannou:

Evolution of magneto-plasmonic interactions in Ni nanostructures: from islands to holes
Sol-SkyMag 2016, San Sebastian, Spain, June 2016

A.V. Chumak:

Spin-wave logic devices: From mm to nm scale
MOSAIC, Varberg, Sweden, June 2016

B. Hillebrands:

Magnon caloritronics
Spin Caloritronics 7, Utrecht, Netherlands, July 2016

V.I. Vasyuchka:

Influence of a thermal gradient on parametric excitation of magnons
Spin Caloritronics 7, Utrecht, Netherlands, July 2016

B. Hillebrands:

Room temperature supercurrents in a magnonic system
Plenary Talk, JEMS 2016 Conference, Glasgow, UK, August 2016

V.I. Vasyuchka:

Spectral properties of the longitudinal spin Seebeck effect
Baltic Spin 2016, Jurmala, Latvia, August 2016

A.V. Chumak:

Towards integrated magnonic circuits
Baltic Spin 2016, Jurmala, Latvia, August 2016

AG MAGNETISMUS
TU KAISERSLAUTERN

A.A. Serga:

Supercurrent in a room-temperature Bose-Einstein magnon condensate
International Conference on Quantum Fluids and Solids (QFS 2016), Prague, Czech Republic,
August 2016

B. Hillebrands:
Magnon spintronics
International Workshop on Spin Transfer, Nancy, France, September 2016

B. Hillebrands:

Magnon supercurrents in a room temperature magnon condensate
Tutorial lecture, SPICE workshop "Quantum Spintronics: Spin Transport through Quantum
Magnetic MAterials", Universität Mainz, Germany, September 2016

A.V. Chumak:

Spin-wave logic devices: Towards integrated circuits
CMD 26 - Condensed Matter Division of the European Physical Society, Groningen, Nether-
lands, September 2016

A.A. Serga:

Bottleneck accumulation of hybrid bosons in a ferrimagnet
Quantum Spintronics: Spin Transport Through Quantum Magnetic Materials, Mainz, Germany,
September 2016

A.A. Serga:

Spin Transport using magnon gases
International School & Conference on Nanoscience and Quantum Transport, Kyiv, Ukraine,
November 2016

6.2.2   Invited seminar talks and colloquia

A.V. Chumak:
Spin-wave logic devices
Fakultät für Elektrotechnik, Informationstechnik, Physik, Technische Universität Braun-
schweig, Braunschweig, Germany, December 2015

A.V. Chumak:
Spin-wave logic devices
INNOVENT e.V. Technologieentwicklung, Jena, Germany, December 2015

A.V. Chumak:
Spin-wave logic devices
Fakultät Physik, Technische Universität Dortmund, Dortmund, Germany, December 2015

B. Leven:
Unidirectional spin-wave edge modes in perpendicularly magnetized $Ni_{81}Fe_{19}$ structures
603. Wilhelm und Else Heraeus-Seminar, Bad Honnef, Germany, January 2016

B. Hillebrands:

Magnon Supercurrents
Zernicke Institute, Groningen, Netherlands, March 2016

P. Pirro:

Spin-wave devices for magnonic data processing: from macroscopic prototypes towards microstructured implementations
Seminar at IPCMS, Strasbourg, France, May 2016

B. Hillebrands:

Advanced Magnonics
Physikalisches Kolloquium IFW Dresden, Germany, June 2016

B. Hillebrands:

Spinwellen und Magnonen - neue Konzepte für Informationstechnologien
Festkolloquium Prof. U. Heinzmann, Bielefeld, Germany, June 2016

A.V. Chumak:

Spin-wave logic devices
Seminar at Physikalisches Institut, Karlsruher Institut für Technologie, Karlsruhe, Germany, August 2016

D.A. Bozhko:

Bottleneck accumulation of hybrid bosons in a ferrimagnet
Seminar: Hard Condensed Matter Theory, Mainz, Germany, August 2016

A.A. Serga:

Supercurrent in a room-temperature Bose-Einstein magnon condensate
Lecture at Department of Physics of University of Porto, Porto, Portugal, September 2016

6.2.3   Lectures at summer schools

A.A. Serga:

Advances in magnonics
International Spintronics School 2016, Tohoku University, Sendai, Japan, August 2016

6.3   Contributed talks and posters

6.3.1   Conferences and workshops

T. Meyer, T. Brächer, P. Pirro, T. Fischer, A.A. Serga, H. Naganuma, K. Mukaiyama, M. Oogane, Y. Ando, B. Hillebrands:

Control of the effective spin-wave damping in microstructured Heusler-Pt waveguides via the spin-transfer torque effect
York-Tohoku-Kaiserslautern core-to-core symposium, Sendai, Japan, November 2015

E.Th. Papaioannou, S. Keller, L. Michalceanu, A. Conca, V. Lauer, J. Lösch, A. Brodyanski, B. Hillebrands:

Reveal the role of interface on the spin pumping effect in Fe/Pt and Fe/MgO/Pt layered systems
York-Tohoku-Kaiserslautern core-to-core symposium, Sendai, Japan, November 2015

T. Meyer, T. Brächer, P. Pirro, T. Fischer, A.A. Serga, H. Naganuma, K. Mukaiyama, M. Oogane, Y. Ando, B. Hillebrands:

Control of the effective spin-wave damping in Heusler-Pt waveguides via the spin-transfer torque effect
13th RIEC workshop on spintronics, Sendai, Japan, November 2015

F. Heussner, T. Brächer, P. Pirro, T. Meyer, T. Fischer, M. Geilen, B. Heinz, A.A. Serga, B. Hillebrands:

Phase-to-amplitude conversion by parallel parametric amplification of coherently excited spin waves in microstructured Ni$_{81}$Fe$_{19}$ waveguides
13th RIEC workshop on spintronics, Sendai, Japan, November 2015

L. Mihalceanu, S. Keller, A. Conca, B. Hillebrands, E.Th. Papaioannou:

Spin pumping in epitaxially grown Fe/Pt and Fe/MgO/Pt systems
13th RIEC workshop on spintronics, Sendai, Japan, November 2015

D.A. Bozhko, A.A. Serga, P. Clausen, V.I. Vasyuchka, A.V. Chumak, G.A. Melkov, B. Hillebrands:

Mixed magnon-phonon condensation at the bottom of the magnon spectrum
603. Wilhelm und Else Heraeus-Seminar, Bad Honnef, Germany, January 2016

A.A. Serga, D.A. Bozhko, P. Clausen, V.I. Vasyuchka, G.A. Melkov, B. Hillebrands:

Magnon supercurrent in a magnon Bose-Einstein condensate subject to a thermal gradient
603. Wilhelm und Else Heraeus-Seminar, Bad Honnef, Germany, January 2016

V.I. Vasyuchka, T. Noack, T. Langner, F. Heussner, V. Lauer, A.A. Serga, B. Hillebrands:

Temporal evolution of the longitudinal spin Seebeck effect in YIG\Pt bilayers
603. Wilhelm und Else Heraeus-Seminar, Bad Honnef, Germany, January 2016

T. Meyer, T. Brächer, P. Pirro, T. Fischer, A.A. Serga, H. Naganuma, K. Mukaiyama, M. Oogane, Y. Ando, B. Hillebrands:

Control of the effective spin-wave damping in HeuslerPt waveguides via the spin-transfer torque effect
603. Wilhelm und Else Heraeus-Seminar, Bad Honnef, Germany, January 2016

V. Lauer, D.A. Bozhko, T. Brächer, P. Pirro, V.I. Vasyuchka, A.A. Serga, M.B. Jungfleisch, M. Agrawal, Yu.V. Kobljanskyj, G.A. Melkov, C. Dubs, B. Hillebrands, A.V. Chumak:

Spin-transfer torque based damping control of parametrically excited spin waves in a magnetic insulator
603. Wilhelm und Else Heraeus-Seminar, Bad Honnef, Germany, January 2016

E.Th. Papaioannou, S. Keller, L. Mihalceanu, A. Conca, V. Lauer, J. Lösch, A. Brodyanski, B. Hillebrands:

Reveal the role of interface on spin pumping effect in Fe/Pt, Fe/MgO/Pt layered systems
603. Wilhelm und Else Heraeus-Seminar, Bad Honnef, Germany, January 2016

D.A. Bozhko, P. Clausen, G.A. Melkov, B. Hillebrands A.A. Serga:

Spectral black hole in a pumped magnon gas
13th Joint MMM/Intermag Conference, San Diego, USA, January 2016

D.A. Bozhko, P. Clausen, A.V. Chumak, B. Hillebrands, A.A. Serga:

Formation of Bose-Einstein magnon condensate via dipolar and exchange thermalization channels
13th Joint MMM/Intermag Conference, San Diego, USA, January 2016

A.A. Serga, D.A. Bozhko, M. Agrawal, V.I. Vasyuchka, B. Hillebrands, M. Kostylev:

Spin-wave excitation, propagation and amplification in YIG-Pt bilayers
13th Joint MMM/Intermag Conference, San Diego, USA, January 2016

T. Langner, A.A. Serga, A. Kirihara, B. Hillebrands, V.I. Vasyuchka:

Influence of a thermal gradient on parametrically excited magnons in YIG-Pt bilayers
13th Joint MMM/Intermag Conference, San Diego, USA, January 2016

M. Vogel, A.V. Chumak, E.H. Waller, T. Langner, V.I. Vasyuchka, B. Hillebrands, G. von Freymann:

An optically reconfigurable magnetic material for the control of spin waves
13th Joint MMM/Intermag Conference, San Diego, USA, January 2016

T. Langner, A.A. Serga, A. Kirihara, B. Hillebrands, V.I. Vasyuchka:

Influence of a thermal gradient on parametrically excited magnons in YIG\Pt bilayers
SPP1538 "Spin Caloric Transport" Kolloquium, Bad Honnef, Germany, March 2016

T. Noack, T. Langner, V. Lauer, F. Heussner, A.A. Serga, B. Hillebrands, V.I. Vasyuchka:

Spectral properties of the longitudinal Spin Seebeck effect
SPP1538 "Spin Caloric Transport" Kolloquium, Bad Honnef, Germany, March 2016

L. Mihalceanu, D. Bozhko, A.A. Serga, B. Hillebrands:

Collective effects and instabilities of a magnon gas
SFB/TR 49 International School on Thermal, Quantum, and Topological Phase Transitions, Bad Endorf, Germany, March 2016

T. Langner, A.A. Serga, B. Hillebrands, V.I. Vasyuchka:

Influence of a thermal gradient on parametrically excited magnons in YIG-Pt bilayers
Young Researchers Symposium 2016 (YRS), Kaiserslautern, Germany, April 2016

P. Pirro, A. Hamadeh, M. Lavanant, J.-P. Adam, B. Tao, Y. Lu, S. Mangin, S. Petit-Watelot:

Domain walls in synthetic antiferromagnets based on perpendicularly magnetized CoFeB
Colloque Louis Néel 2016, Saint Dié des Vosges, France, April 2016

A. Conca, S. Keller, L. Mihalceanu, T. Kehagias, G.P. Dimitrakopulos, B. Hillebrands, E.Th. Papaioannou:

Characterization of FM/Pt,Ta bilayers (FM= Fe, CoFeB) for spin pumping by ferromagnetic resonance spectroscopy
3rd Workshop of the Core-to-Core Project Tohoku-York-Kaiserslautern, Kaiserslautern, Germany, June 2016

E.Th. Papaioannou:

The concept of a magneto-plasmonic meta-material
3rd Workshop of the Core-to-Core Project Tohoku-York-Kaiserslautern, Kaiserslautern, Germany, June 2016

S. Keller, L. Mihalceanu, A. Conca, M.R. Schweizer, J. Lösch, B. Hillebrands, E.Th. Papaioannou:

Spin pumping at structurally engineered interfaces
3rd Workshop of the Core-to-Core Project Tohoku-York-Kaiserslautern, Kaiserslautern, Germany, June 2016

V.I. Vasyuchka, T. Langner, A.A. Serga, A. Kirihara, B. Hillebrands:

Influence of a thermal gradient on parametrically excited magnons in YIG/Pt bilayers
3rd Workshop of the Core-to-Core Project Tohoku-York-Kaiserslautern, Kaiserslautern, Germany, June 2016

T. Meyer, T. Brächer, P. Pirro, T. Fischer, A.A. Serga, H. Naganuma, K. Mukaiyama, M. Oogane, Y. Ando, B. Hillebrands:

Control of the effective spin-wave damping in Heusler-Pt waveguides via the spin-transfer torque effect in the short pulse regime
The 9th International Symposium on Magnetic Multilayers (MML), Uppsala, Sweden, June 2016

T. Noack, T. Langner, V. Lauer, F. Heussner, A.A. Serga, B. Hillebrands, V.I. Vasyuchka:

Spectral properties of the longitudinal spin Seebeck effect
IEEE ICMM 2016, Tuscaloosa , USA, June 2016

A.A. Serga, A.V. Chumak, B. Hillebrands:

Magnonic-crystal-based magnon transistor
Proceedings of 7th International Conference on Metamaterials, Photonic Crystals and Plasmonics (META'16), Torremolinos, Spain, July 2016

V. Lauer, D.A. Bozhko, T. Brächer, P. Pirro, V.I. Vasyuchka, A.A. Serga, M.B. Jungfleisch, M. Agrawal, Yu.V. Kobljanskyj, G.A. Melkov, C. Dubs, B. Hillebrands, A.V. Chumak:

Spin-transfer torque based damping control of parametrically excited spin waves in a magnetic insulator
8th Joint European Magnetic Symposia (JEMS), Glasgow, UK, August 2016

T. Meyer, T. Brächer, P. Pirro, T. Fischer, A.A. Serga, H. Naganuma, K. Mukaiyama, M. Oogane, Y. Ando, B. Hillebrands:

Control of the effective spin-wave damping in Heusler-Pt waveguides via the spin-transfer torque effect in the short pulse regime
8th Joint European Magnetic Symposia (JEMS), Glasgow, UK, August 2016

E.Th. Papaioannou, M. Rollinger, P. Thielen, E. Melander, E. Östman, V. Kapaklis, M. Cinchetti, A. Garcia-Martin, M. Aeschlimann:

Light localization and magneto-optic enhancement in magneto-plasmonic meta-structures
8th Joint European Magnetic Symposia (JEMS), Glasgow, UK, August 2016

L. Mihalceanu, S. Keller, A. Conca, N. Pliatsikas, D. Karfaridis, G. Vourlias, B. Hillebrands, E.Th. Papaioannou:

Investigation of the spin-pumping effect in epitaxially grown Fe/MgO/Pt systems
8th Joint European Magnetic Symposia (JEMS), Glasgow, UK, August 2016

T. Meyer, P. Pirro, T. Brächer, A.A. Serga, H. Naganuma, K. Mukaiyama, M. Oogane, Y. Ando, B. Hillebrands:

Temporal behaviour of the effective damping manipulation in Heusler-Pt waveguides via the spin-transfer torque effect
International Workshop and School on Spin Transfer (IWST), Nancy, France, September 2016

V. Lauer, M. Schneider, D.A. Bozhko, T. Meyer, T. Brächer, P. Pirro, B. Heinz, B. Lägel, C. Dubs, M.C. Onbasli, C.A. Ross, B. Hillebrands, A.V. Chumak:

Spin-transfer torque based damping control of spin waves in yttrium iron garnet
International Workshop and School on Spin Transfer (IWST), Nancy, France, September 2016

M. Schneider, V. Lauer, T. Meyer, T. Brächer, P. Pirro, B. Heinz, B. Lägel, M.C. Onbasli, C.A. Ross, B. Hillebrands, A.V. Chumak:

Generation of auto-oscillations in YIG/Pt microstructures on the nano-second time scale
International Workshop and School on Spin Transfer (IWST), Nancy, France, September 2016

A.V. Chumak, A.A. Serga, P. Pirro, B. Hillebrands:

Magnon transistor and majority gate for wave-based computing
10th International Congress on Advanced Electromagnetic Materials in Microwaves and Optics (Metamaterials 2016), Chania, Crete, Greece, September 2016

L. Mihalceanu, P. Frey, D. Bozhko, A.A. Serga, B. Hillebrands:

Magnon-condensation scenarios as temperature-dependent phenomena in the low-temperature regime
Quantum Spintronics: Spin Transport Through Quantum Magnetic Materials, Mainz, Germany, September 2016

6.3.2   Contributions to the DPG Frühjahrstagung

10 contributions: DPG Frühjahrstagung, Regensburg, Germany, March 2016

6.3.3 Schools

F. Heussner, T. Brächer, P. Pirro, T. Meyer, T. Fischer, M. Geilen, B. Heinz, B. Lägel, A.A. Serga, B. Hillebrands:
Enhancement of the spin-wave propagation distance in microstructures by localized parallel parametric amplification
IEEE Magnetics Society Summer School 2016, Sendai, Japan, July 2016

S. Keller, L. Mihalceanu, A. Conca, M.R. Schweizer, J. Lösch, B. Hillebrands, E.Th. Papaioannou:
Spin pumping at structurally engineered interfaces
IEEE Magnetics Society Summer School 2016, Sendai, Japan, July 2016

T. Fischer, T. Meyer , T. Brächer , P. Pirro , B. Heinz , M. Geilen, A. Conca, B. Hillebrands:
Investigation of $Co_{40}Fe_{40}B_{20}$ spin-wave waveguides
IEEE Magnetics Society Summer School 2016, Sendai, Japan, July 2016

6.4 Annual group retreat

In 2016 our group organized a three-day retreat at the Kurhaus am Trifels, Annweiler. We have had two days of intense scientific discussion and 24 presentations by our group members and guests. Prof. Dr. Dominik Durner from the Weincampus Neustadt gave a fascinating evening talk on the innovative methods in the field of oenology. On the first day, the group members participated in a soft skill seminar on project and time management in the framework of the "Diemersteiner Selbstlerntage" held by Dr. Martin Sauerland and Maria Peter in assistance.

6.5 Other meetings and trade fairs

M. Kewenig, T. Fischer, D.A. Bozhko, I.I. Syvorotka, B. Hillebrands, A. Chumak:
Scientific progress report: Kaiserslautern Realization of a spin-wave majority gate
InSpin Meeting, Brussels, Belgium, April 2016

A. Conca:
HEUMEM Progress Report Kaiserslautern: CFA Thickness variation
HeuMem Meeting, Frankfurt am Main, Germany, April 2016

A. Conca, V. Lauer, P. Pirro, L. Mihalceanu:
Applied Spintronics and STeP Project
Hannover Messe (at Rhineland-Palatinate stand), Hannover, Germany, April 2016

F. Heussner, P. Pirro, A.A. Serga, B. Hillebrands:
Project B01: Spin-wave caustics - Overview
Spin+X Supply Chain Meeting, Kaiserslautern, Germany, April 2016

F. Heussner, P. Pirro, A.A. Serga, B. Hillebrands:

Dynamically Switchable Signal Splitting in 2D Magnonic Microchips by Locally Controlled Spin-wave Caustics
Spin+X Supply Chain Meeting, Kaiserslautern, Germany, October 2016

6.6   Awards, Fellowships, and others

B. Leven:

Innovationspreis des Landes Rheinland-Pfalz "Entwicklung energieeffizienter Sensoren auf Basis des Tunnelwiderstands (TMR) insb. für Industrie 4.0 und das Internet der Dinge (IOT)", Kategorie "Kooperation, gemeinsam mit Sensitec GmbH und Johannes Gutenberg-Universität Mainz", January 2016

B. Hillebrands:

ERC Advanced Grand "Supercurrents of Magnon Condensates for Advanced Magnonics (Super Magnonics)", May 2016

T. Brächer:

Preis der ALUMNI-Stiftung TU Kaiserslautern, July 2016

Appendix: Impressions from 2015

Ph.D. defense Dr. Donata Passarello, 27.11.2015

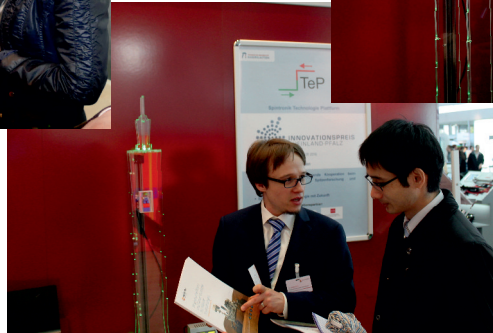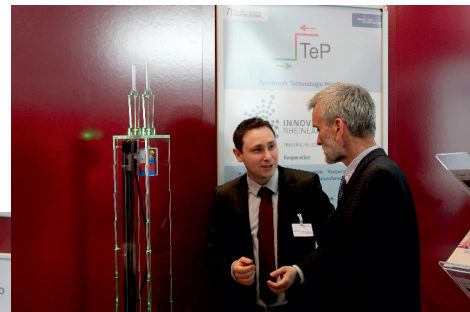Tag der Physik, 05.12.2015

XMAS, 18.12.2015

Innovationspreis, 20.01.2016

Nacht, die Wissen schafft, 22.04.2016

Hannover Messe, 24.-28.04.2016

Habilitation Andrii Chumak, 13.06.2016

AG MAGNETISMUS
TU KAISERSLAUTERN

Core-to-Core Workshop, 22.-24.06.2016

Group excursion, 22.07.2016

Schülerinnentag, 29.09.2016

Group Retreat, 04.-06.10.2016

Prof. Dr. Burkard Hillebrands

Fachbereich Physik

Landesforschungszentrum OPTIMAS

Technische Universität Kaiserslautern, Germany

P.O. Box 3049

67653 Kaiserslautern

Phone: +49 631 205-4228

Fax: +49 631 205-4095

hilleb@physik.uni-kl.de

www.physik.uni-kl.de/hillebrands/

TECHNISCHE UNIVERSITÄT
KAISERSLAUTERN